Remote vital signs monitoring using a mm-wave FMCW radar

by

Mostafa Alizadeh

A thesis
presented to the University of Waterloo
in fulfillment of the
thesis requirement for the degree of
Master of Science
in
Electrical and Computer Engineering

Waterloo, Ontario, Canada, 2019

Author's Declaration

I hereby declare that I am the sole author of this thesis. This is a true copy of the thesis, including any required final revisions, as accepted by my examiners.

I understand that my thesis may be made electronically available to the public.

Abstract

A vision on the migration from contact standard health monitoring measurement devices to non-contact measurement technologies has gained a tremendous attention in literature and in industry. A promising method for realizing the remote measurement of vital signs is using electromagnetic radars such as frequency modulated continuous wave (FMCW) radars. However, using these radars has challenges to precisely acquire the respiration and heart rates. A solution for higher accurate measurement of the vital signs can be the use of mm-wave frequencies, which gives a high-resolution sensing of displacements in an environment in the order of sub-mm changes. On the other hand, being in mm-wave bands increases both hardware and signal processing designs and implementations.

In this work, a mm-wave radar is used to monitor the breathing and the heart rates as well as their waveforms for further clinical diagnostics. To that end, we established a complete analysis of the FMCW radars principles by considering hardware impairments. The analysis considers the effect of antenna coupling, RF cross-talk, stationary clutters, phase noise, IQ imbalances, and the thermal noise. Also, the effect of the individual hardware imperfections on the phase quality is shown by simulations and experiments. The simulations are carried out with a Matlab Simulink model. For the experiments, Texas Instruments (TI) mm-wave FMCW radars have been used.

To earn insight into vital signs monitoring, different experiments are designed. In the experiments, the effect of the thermal instability of the RF parts on the phase is shown. In addition, to mimic the behaviour of the chest vibration due to respiration and the heartbeats, a two-pendulum system is designed and tested. Particularly, the pendulum system performance in terms of vibration frequency estimations of the two pendulums versus distance is then measured. In the simulations, the system performance is obtained for different signal to noise ratios (SNR) and different phase noise levels, as well as different stationary clutters.

Finally, to test the TI sensors for different directions to the subjects, Hexoskin smart garment is used as a reference sensor, which is a reliable commercial product. Our results show great system improvement in terms of accuracy of the vital signs detection in comparison to other similar research. For different sleep positions, the accuracy of HR and BR are greater than 94% and 96%, respectively. In addition to detecting the vital rates, we have shown that their waveforms can also be reconstructed by using an adaptive optimum filter.

Acknowledgements

First of all, I should thank **God** whose blessings are endless during this life or Hereafter. He gave and will give the meaning, the courage, and the power for this work and the future works as he said: "The effort of one who faithfully strives hard for the life to come, will be appreciated."

I would also like to express my sincere gratitude to my advisers professor **Safieddin (Ali) Safavi-Naeini** and professor **George Shaker** for their continuous support of my Master study and related research, patience, motivation, and immense knowledge. Their guidance has helped me in all the time of research and writing of this thesis.

Also, I want to thank all **my friends** who supported me during the completion of this degree. I am not mentioning their names because they deserve to be in my heart and my mind all the time.

A special thank to **my parents** who are constantly supporting me emotionally and subjectively. Without them, the creation of this thesis was not possible.

Dedication

This study is wholeheartedly dedicated to my beloved parents, who have been my source of inspiration and gave me strength when I thought of giving up, who continually provide their moral, spiritual, emotional, and financial support.

Table of Contents

List of Tables

List of Figures

Abbreviations

ANC adaptive noise cancellation 8, 85

AR auto regressive 35

ARM advanced RISC machine 13

AWGN additive white Gaussian noise 10, 24

BR breathing rate 1, 2, 4, 11, 17, 49, 71, 82, 84, 85

BSS blind source separation 9

CFAR constant false alarm rate 100

CW continuous wave 3, 4, 6

DACM differentiate and cross-multiply 3

DDS direct digital synthesizer 2

DSP digital signal processor 13

ECG electrocardiographic signal xii, 76, 79, 80

FOV field of view 24

FTPR frequency-time phase regression 3

HMI hip motion intensity 17

HMUSIC harmonic multiple signal classification 35

HR heart rate 1–4, 11, 17, 71, 82, 84, 85

HRV heart rate variability 3, 4, 17, 74, 85

LNA low-noise power amplifier 20

LSE least square estimator 8

MUSIC multiple signal classification 9, 84

NF noise figure 23, 65, 85

NLLS non-linear least square estimation 29

PA power amplifier 20

PAPR peak-to-average-power ratio 20

PSD power spectral density 54

PWM pulse width modulation 51

RCS radar cross section 22, 53, 70, 100

RF radio frequency 1

RTT round-trip time 20

Rx receiver 13

SNR signal to noise ratio 5, 65

STFT short-time Fourier transform 43

SVD singular value decomposition 6

THD total harmonic distortion 63

TI Texas instruments 1, 9, 13, 85

Tx transmitter 13

UART universal Asynchronous Receiver/Transmitter 13, 93

ULA uniform linear array 62

UWB ultra-wideband 6

WSS wide sense stationary 22, 26, 36

List of Notations and Symbols

T_r Chirp duration 19–21

T_c FMCW frame period 24

$f_{b,max}$ ADC sampling rate 24–26

B_s FMCW sweeping bandwidth 19, 22, 26

$\boldsymbol{x}$ Column vector xvi, 29, 35

f_{max} The frequency at the end of FMCW sweep 19

f_{min} The frequency at the start of FMCW sweep xvi, 19, 20, 22

t_f Fast time 20, 21, 24

f_c FMCW frame rate 24, 26, 27

λ_{max} The wavelength corresponding to f_{min} 21, 26, 27

c Light speed 21, 22

$\boldsymbol{x}^H$ Complex vector hermitian 36

A Matrix xvi, 29

$\| \boldsymbol{x} \|^2$ norm-2 squared of a column vector $\boldsymbol{x}$ 29

ϕ_n Phase noise 20, 21

$A^\dagger$ Pseudo-inverse of a matrix A 29

t_s Slow time 20, 21, 24, 26

$\boldsymbol{x}^T$ Vector transpose 29

Chapter 1

Introduction

1.1 A big picture

As the analog and digital circuits technologies have been developed, semiconductor manufacturers have integrated both digital and analog parts on a single chip. This integration not only reduces the size and the cost but also the power consumption, and makes it attractive for energy-harvesting and portable systems. Indeed, the modern chip designs equip sensors with built-in processors with which they can be connected to other devices and chips. In fact, they are capable of being connected to others chips to make a network of sensors.

One of the greatest companies with outstanding repute, Texas instruments (TI), has developed modular mm-wave radars with seamless integration of the radio frequency (RF) and analog circuits to digital circuits. The modularity and generality of the chips allows advanced developers to mediocre users to adopt and configure them for their applications. In this work, we will use them to detect and characterize the vital signs' rates, namely breathing rate (BR) and heart rate (HR). In general, the problem is developing a system based on a mm-wave FMCW radar as a vibrometer. In the course of design and system implementations, we have investigated all aspects by considering both analog and digital aspects.

1.2 Literature survey

Monitoring vital signs of a human like heart rate and breathing rate is very critical for saving lives. Individuals might suffer from a disease such as sleep apnea, or their lives have been threatened by a natural disaster. In the former case, there is a need for continuous surveillance of a patient in a room while in the latter case the problem is finding the victims through obstacles like walls. In addition, if a patient's skin is burned, it is not possible to attach a device to the subject body to record and analyze their health-related signals. One solution is using radars with the capability of sensing any environment dynamics. The general principle of a typical radar is sending a specific signal then listening to its echo in order to extract environmental features. This idea is not new as it has been used by bats for million years ago (see [62]) in that they use acoustic waves. The acoustic waves could not travel a long distance and they are easily interfered with any mechanical movements and they need a medium for propagation. In contrast, electromagnetic (EM) waves can propagate without a medium and can penetrate through obstacles and do not have the limitations of acoustic waves.

Among popular applications of EM radars, biomedical sensing has gained increasing attention for adopting them in remote sensing of vital signs such as HR, BR, blood oxygen density, etc. For instance, radars can find HR and BR by detecting the chest wall movement. This is greatly helpful for reducing the number of contact biomedical sensors for monitoring of a patient over a long time. For example, to monitor sleep apnea, in [30] the authors proposed a remote controlling system, which uses a 24 GHz radar.

As we are interested in using FMCW radar, it is important to note that there is no comprehensive analysis for the Doppler accuracy of FMCW radars. But in [16], authors investigated the range accuracy considering non-idealities in FMCW generation. This is the first paper using direct digital synthesizer (DDS) for artificially adding non-linearities and phase noise to evaluate their effects on the range detection. Using DDS helps to sweep the amount of nonlinearity as well as the noise power. In fact, the phase noise power and the FMCW ramp nonlinearity are represented by adding a Gaussian noise and a sinusoid term (with much less frequency than the FMCW carrier frequency) in the phase of the FMCW, respectively. Besides, they used short-time chirp-z transform for obtaining the sub-micro meter range accuracy which is far less than the fundamental range resolution of the radar. Due to importance of the phase noise on our system performance, we will discuss the developed Matlab Simulink model to clarify the effect of the phase noise on the beat signal phase as well as the end frequency estimator (see section 4.4).

In the generation of an FMCW signal, a sort of phase randomness appears, which is called phase noise. While it is manifesting itself in the phase, it has impact on the

magnitude of the generated signal. In addition, the phase noise degrades the quality of the parameter estimation in any radars particularly FMCW radars. In general, the phase noise effect in the range detection of any radar kind is discussed in [19]. When the echo signal is mixed with the transmitted signal at the receiver, the phase noise autocorrelation becomes a function of transmitted phase noise autocorrelation. This phenomenon is called the *range correlation effect*. In brief, [19] clarifies that the phase noise effect in the range detection of continuous wave (CW) or FMCW radar systems increases as the range of the subject increases. Fortunately, the phase noise due to the range correlation effect is very low for our case because the subject is very close to the radar located at a few meters distance. We will talk about this effect in section 3.2.

In [59], the authors focused on measuring the range error of an FMCW radar at 77 GHz. In fact, They used theories of previous works for analytical expression of the range error rate lower bound. They showed that the range uncertainty increases by increasing the range, which can be inferred heuristically.

The authors in [65] reconstructed the cardiac motion at different sides by claiming that the cardiac and the respiration motions are isotropic meaning that the volume change of lungs and heart can be detected from all directions. In contrast, they could not extract it at the left/right sides as clean as the front or back sides. It is shown that by applying the proposed polynomial curve fitting, most cardiac motion cycles have better performance than the frequency-domain filtering technique. They compared the polynomial fitting method with the traditional filtering technique, which has frequency-dependent phase shift, and they found out that it is more suitable for time-domain analysis to remove the influence of respiratory motion. Their method lacks enough evidence for convincing how the polynomial interpretation of the breathing wave outweighs the traditional filtering, which are seemed to be more practical. In [65], the radar sensor operated at a carrier frequency of 15 GHz with a 10-dBm power to detect the time-domain cardiac motion of the subject. In addition, using the differentiate and cross-multiply (DACM) method for phase unwrapping has been exploited.

Nosrati *et al.* in [54] used a CW radar at 2.4 GHz. Basically, for the heart signal acquisition enhancement, the second derivative of the received phase is taken, which means that the input phase signal is filtered by a filter with the frequency response of ω^2. This filter amplifies the higher frequencies pertaining to the HR. But, the final rate estimation of HR will be biased with a higher weight on the lower frequencies. However, they claimed that the accuracy is improved by almost 10% with the use of frequency-time phase regression (FTPR) method instead of FFT.

For determining autonomic nerve activities, heart rate variability (HRV) is a helpful

sign, which can be characterized by different parameters [48]. HRV has two parts of low (0.03-0.15 Hz)[1] and high frequencies (0.15-0.45 Hz)[2]. They used a 24 GHz radar (JRC: NJR4265J1K) and achieved very accurate results of 93% with comparing to an ECG recorder.

A CW radar equipped with a phased array is used to monitor two targets' vital signs in [52]. They designed the antenna array such that it has two beams at two angles. They designed a dual-beam proof-of-concept radar with a 4-element linear array (for both Tx/Rx). The two beams were at 25 and -35 degrees with respect to the antenna boresight. In this way, the phase signature of two subjects located in the field of view of two different beams can be separated. They tested the system for two subjects by detecting BR, but HR detection is neglected.

In [18], a CW radar at 79 GHz is used together with a six-port for mixing the Rx/Tx signals. Adopting a passive RF component instead of an active mixer reduces power and cost. The outputs are four with different relative phase shifts. They have shown that this radar can be used for the detection and characterization of the vibrating objects.

Similarly, in [15], the authors used the FMCW radar for the purpose of vital signs detection. To choose the start frequency, they tested the FMCW radar at different start frequencies with different bandwidths and different subject positions. At the end, they came up with a great conclusion that the radar reliably senses vital signs for many cases, however, they chose 9.6 GHz for the purpose of the demonstration and implementation by considering other factors such as the low interference on the wireless local area networks. They analyzed the magnitude and phase of the received echo signal and they showed that the vital signs detection can be carried out on either phase or magnitude. This result is against the discussion in [44] where the authors illustrated that the magnitude analysis comes with higher order harmonics which degrades the vital signs' rate detection robustness, instead they exploited the phase extraction. Furthermore, [15] did not discuss the linear phase trend that was apparent in the captured phase. This behavior seemed to be the impact of the hardware non-linearities while they neglected with no more clarification.

A similar phase acquisition using FMCW radar at 80 GHz was presented in [66]. The authors assumed that the distance of the target is known, therefore they did not concentrate on designing an algorithm for finding the target ranges. In addition, the radar was tested in front, back, left, and right sides of the subject when the target was sitting on a chair.

[1]Low HRV frequency is related to both sympathetic and parasympathetic activities. The former regulates the body's unconscious actions and the later is responsible for stimulation of "rest-and-digest" that occur when the body is at rest.

[2]High HRV frequency contains parasympathetic activities

This experiment setup cannot be used for a practical clinical purpose when a patient is supposed to be laying down on the bed with lots of background clutters. In addition, they did not use phase unwrapping and we will show that is necessary in mm-wave frequencies.

It is also important to know the electromagnetic properties of the body to understand how the wave is reflected. In [61], the authors investigated the main reason for reflecting an EM wave from a body in microwave frequencies. In particular, there are two main reasons: 1) blood perfusion underneath of the skin surface leading to the skin impedance variation, 2) skin/body surface movement. By designing some experiments, they found out the body displacement has a higher influence on reflecting the signal than the impedance change of the skin surface. Their research was conducted in microwave frequencies at which a portion of the wave can penetrate the body. While in mm-wave frequencies, as we consider, the wave is totally reflected off the body surface.

The echo signal characteristics such as its polarization and power depend on the constituent material of the target and its orientation. Consequently, in the literature numerous studies are about echo signal characterization. There are two different purposes to investigate the EM modelling of a target: 1) exploiting the model for optimum design of the radar hardware and signal processing algorithms for a particular application, 2) extracting the properties by a radar for target classification. For instance, the EM characteristics of the human body have been studied extensively in [32], [35], [8] from 10 Hz to 100 GHz.

In contrast, the authors in [49] proposed a single layer model of the torso while the complete model is a multi-layer dielectric material. They developed the model based on the fact that the reflection and transmission coefficients of the wave remain the same for both models. In addition, for more simplification, they used only a portion of the torso for simulating the vital signs to reduce the solution region in EM simulation. The vital sign detection is also carried out in the EM simulator. This enabled them to compare their model with the experiments. They used a stepped frequency continuous wave (SFCW) radar operating at 2.5 GHz with 1 GHz of sweeping bandwidth in the experiments. Single-subject and two-target experiments were conducted to show a good agreement between the simulation based on the single-layer model and the practical measurements.

The use of other type of radars has been considered in the literature. For instance, the authors in [40] proposed a time-varying filter to reduce noise in order to extract the heart rate with an impulse radar. Initially, the algorithm finds the respiration rate. Then, it adopts a time-varying filter after which the derivative of the received signal is taken to increase the signal to noise ratio (SNR) for the estimation of the heart rate. Although this paper considers how to increase SNR for detecting the heart rate, there was no thorough description of the experiment equipment and the setup. Indeed, the accuracy of the

reference sensor has not been reported.

A ultra-wideband (UWB) radar is employed in [50] for individuals' detection in a natural disaster such as under ruined buildings after an earthquake. Because the system is wideband, it has low intrinsic SNR. Therefore, the victim's breathing rate and his range estimation is performed by taking singular value decomposition (SVD) of the so called *slow-fast time* matrix. The SVD is used for the noise reduction by taking a portion of the slow-fast time matrix containing most of the signal power. In this way, a subspace of the matrix space is removed in which the power of the noise is dominant and it contributes to decrease SNR. The singular values are scaling factors and determine the signal power corresponding to the space of that singular value. To determine the signal subspace, they set a threshold on the singular values by which the signal space was found to be the subspace spanned by the basis corresponding to the singular values greater than the threshold.

The selection between Heterdyne or Homodyne receivers along with DC and IQ imbalance compensations are investigated in [29]. In Heterodyne receivers, there is an image frequency band which falls in the desired band in baseband. The image frequency must be eliminated by an RF BPF before mixing in the Heterodyne architecture. In contrast, in Homodyne receiver the positive and negative frequencies will be overlapped on each other in the baseband which increases the noise level (see section 2.1.1). However, this problem can be solved by the use of IQ mixer. A complete comparison between Heterdyne and Homodyne receivers are discussed in [29].

In CW radars with IQ mixers, the correlated signal, beat signal, has a constant phase, which is a function of the distance to the target as well as the other constant delays between the transmit and receive paths. If there is a vibrating object in front of the radar, the beat signal will be a complex exponential with a frequency equal to the vibration frequency. But, the constant phase determines the centre point of the arc around which the trajectory of the complex points will be shaped in the real-imaginary plane[3]. If we assume that the real part of the complex is used for the vibration analysis, the small angle approximation is only valid when the constant phase is around multiple of 2π. On the other hand, if it is not, the phase of the real part will be a polynomial function of the phase, based on the Taylor series expansion of cosine. Therefore, without knowing the distance of the target, it will be hard to performe phase analysis by taking only real or imaginary parts of the beat signal [29]. The problem is referred to as optimum/null point detection in CW radars with real mixing. Furthermore, we shall address the real and IQ mixing in more details in section 2.1.1.

[3]The point cloud in the complex plain is not a complete circle in the microwave frequencies for the vital signs detection as the phase is not rotating a complete circle. This is because the phase modulation is occurred based on relative movement of the chest and the wavelength, which is very small in these bands.

Among other radars, we chose FMCW for our study. Compared to the other alternatives, mm-wave FMCW radars have a collection of advantages and features, which could not be found in a single radar. Those are:

- Being a mm-wave radar: The high attenuation in mm-wave frequencies provides a high isolation between the co-located operating radars even if they are separated in a few meters. Indeed, tiny displacements in mm are comparable to the wavelength so they can be detected. This high sensitivity is required to detect the chest wall movement, which is in mm order.

- Discriminating range or localizing: The radar can distinguish the reflections from different ranges; therefore, potentially it can be used for multi-subject vital signs detection. This feature is recognized as the main advantage of an FMCW radar in [66]. Indeed, high propagation attenuation reduces the possibility of having an echo signal, which is bounced off multiple reflectors. Most probably, the echo signal is reflected off a single object if the environment is not rich scattering. In that area, the received signal at particular range experienced a line of sight wireless channel. In contrast, CW radars suffer from multipath fading because they collect all reflections from all objects at all visible ranges in a one sinusoid signal.

- Being robust against thermal noise: FM signals are more robust against noise in comparison to AM signals. Also, in FMCW radars the vital sign information is encoded in the received phase similar to FM signals. Thus, FMCW radar is less affected by the noise in comparison to impulse radars.

There are many efforts in literature for removing random body motions for vital signs detection. In fact, the vital signs detection can be achieved when the body of the subject is perfectly stationary, otherwise any random motion creates harmonics and distortions in the signal such that detecting the vital signs becomes impossible. There are some solutions proposed such as Changzhi *et al.* , in [43], proposed a two-Doppler radar system by which they cancelled random body motions. They suggested the use of two radars placed on the back and front sides of the body in order to have two different samples of the phase modulation. By having them and considering the fat that the signs of the modulated phases due to body motion are different, they can be combined such that the output contains only the vital signs' phase modulation. To implement the signal processing, they used phase demodulation, which has advantages compared to the complex signal analysis [45]. To exploit the benefits of the phase demodulation, the DC offset and IQ imbalances of the complex signal should have been removed before moving to the phase domain. The DC

offset removal is a huge challenge ([43]) since it could not be distinguished with the DC generated by the vital signs' phase modulation (see section 3.3).

In addition to the body motion, self-motion of the radar with respect to the ground coordinates should be removed. For example, if the radar is installed at the back of a driver seat for health monitoring, the radar shakes due to bumps in the road. Fang *et al.* , in [70], proposed dual-band Doppler radar, which uses the fundamental and harmonic frequencies of the LO to have two Doppler radars. The Doppler radar operates at 2.4 and 4.8 GHz. The fundamental frequency is used for vital signs detection while the other one is used for the radar platform motion cancellation. More specifically, the harmonic Doppler radar has Tx/Rx antennas pointed to a fixed reflectors to measure the radar motion. A single low-IF receiver downconverts both fundamental and harmonic signals. By the two observed IF signals, similar to [43], the radar motion can be cancelled. It is interesting to note that the method used in [70] is not a simple subtraction or addition of the harmonic Doppler signal; instead, they employed an adaptive noise cancellation (ANC) method, [67]. Here, the reference signal is the harmonic response while the input signal is the fundamental Doppler response. The ANC adopts an adaptive updating of filter coefficients by which the desired error signal converges to zero. The zero error is equivalent to removing the radar motion from the signal containing both radar and the vital signs modulations.

As mentioned before, one challenge in phase acquisition of the CW or FMCW radars is the existence of a DC in the received signal. The reasons for such DC are mainly three sources: 1) antenna coupling or RF cross-talk, 2) stationary object in a desired range, 3) the target phase modulation. The last one should not be removed from the signal while the other two should. There is no way to distinguish the first two DC sources from the last one. Thus, we should resolve the issue either by removing the sources or accepting the phase distortion. Authors in [38] investigated the DC cancellation methods proposed in the previous works. There are different techniques for estimating the centre point of an incomplete circle such as least square estimator (LSE) [22], linear demodulation [29, 56], Yuen method [68], compressed sensing method [13]. Among them the compressed sensing method represents more accurate results and we will describe it in section 3.3.

After the phase acquisition, the phase contains two periodic signals. In fact, the phase is modulated by two vibrating objects. The aim is to find the fundamental frequency of the periodic signals. This is a basic problem, which has been investigated extensively in literature under the topic of f_0 estimations, fundamental frequency estimation, and the pitch detection, traditionally[4]. The fundamental frequency estimator for a mixture of the

[4]The terminology used in the speech analysis but we will use the term "fundamental frequency" estimation.

periodic signals has a wide range of applications such as speech and image characterization and compression, individuals identifications etc. Extracting periodic signals from a single channel noisy observation may be similar to the blind source separation (BSS) problems; however, they differ in nature for having assumptions on the behaviour of the sources, which are assumed to be periodic. When the original periodic source is mixed with a noise, the mixed signal is not a periodic signal and it is called pseudo-periodic (or quasi-periodic) signals. The problem boils down to the spectral analysis, which are divided into two general categories of parametric and non-parametric methods. For example, autocorrelation based techniques are parametric methods in which the autocorrelation of the signal is used to determine the fundamental frequency. These methods are biased and depend on the magnitude of the signal. Thus, if there are large fluctuations in the signal magnitude, the method fails to find the true fundamental frequency [12][5]. Indeed, they depend on a threshold, which has must be adaptively adjusted to maintain a low level of error [66].

Furthermore, there are many parametric high resolution methods such as linear prediction [21], subspace methods [25, 10], harmonic fitting [47], maximum liklihood [26], cepstral method [51], and Bayesian estimation [20, 36]. Among subspace methods, multiple signal classification (MUSIC) analysis exploits the signal subspace models to enhance, separate, and estimate the periodic signal properties [23]. Christensen *et al.* , in [11], did not only find the fundamental frequency, also they fully characterized the periodic signals. A complete explanation and the mathematical derivation of the fundamental frequency and the optimum filter design are given in section 3.5. We will use this method for the harmonic analysis of the received radar phase for the vital rate estimations.

Authors in [10] developed an optimization problem in which the model order in [23] and the fundamental frequency of a periodic signal will be obtained simultaneously. This relies on a higher computational burden while it can be avoided by assuming a fixed model order but loosing accuracy. We shall investigate each vital signs separately in chapter 5.

For our measurements, we used TI mm-wave radars in this work. One advantage is that they leverage the benefits of IQ demodulators. They bring SNR improvement, noise level estimation, intermodulation reduction, and simple range and phase demodulation. We will discuss these in the next chapter.

[5]This is why we will not use this method for the vital signs rate extraction.

1.3 Main contributions of the work

This work shows the feasibility and validity of using an FMCW radar to monitor vital signs remotely. Also, we will investigate the theories required for fundamental frequency estimations of two vibrating objects, in general. To achieve so, we used a mm-wave radar from **TI** to analyze, develop, design and implement the signal processing. A summary of the main contributions of the work are as follows:

1. A complete system model of a typical FMCW radar is presented including the antenna coupling or RF cross-talk, phase noise, IQ imbalance, and stationary clutter.

2. The DC offset calibration is investigated and showed how it will affect the phase quality.

3. The phase analysis is presented in which the phase wrapping is embedded and proposed to uncover the true phase modulation. Indeed, the constraint for the proper working of the algorithm is derived, which depends on the vibration frequency and the magnitude of the vibrations.

4. An optimum filter design for the characterization and enhancement of the periodic signals is included at the end of signal processing chain to find and estimate the vital signs waveforms and their fundamental frequencies.

5. We designed experiments in which we had stationary objects to identify the linear phase trend for the stationary targets.

6. We designed a two-pendulum system by which we were able to mimic the chest wall movement due cardio-respiratory activities. The experiments helped to gain intuitions for the vital sign detections.

7. We implemented the most complete FMCW radar system in Matlab using Simulink model. The model gives a realistic sense of the system performance in the presence of additive white Gaussian noise (AWGN), phase noise, IQ imbalance, stationary clutters, etc.

8. Finally, the proposed signal processing is examined for vital signs detection. The accuracy of the system compared to the other similar works using an FMCW radar.

1.4 Summary

In Chapter 2, we will introduce brief features and specifications of the used equipment for the experiments. They are **TI** mm-wave radars and Hexoskin vest. We will also discuss the benefits of the IQ mixing in a radar rather than using the real mixing.

In Chapter 3, the fundamental FMCW radar principles are discussed. This chapter will substantiate the mathematical derivations required for the vital signs detection. Important topics are DC compensation process, phase analysis of a vibrating object or a radial movement, harmonic analysis, and real to imaginary phase transformation.

Chapter 4 verifies the proposed system with different experiments. They are stationary tests, pendulum tests, and the Matlab simulation. We will discuss the results obtained by the simulations, which are very close to the practical observations.

Chapter 5 contains experiments for the vital signs detection. Generally, two sets of experiments were conducted. In the first set, a subject was sitting in front of the radar facing the radar at a right angle. In the second set of experiments, a subject was sleeping on a bed and the radar was mounted on the ceiling above the bed. The final results of BR and HR accuracies are compared to the preceding works.

The work is concluded in Chapter 6 by wrapping up the novelties of the work and the future extensions.

Chapter 2

Hardware and equipment

For this study, we use an off-the-shelf radar equipment by *Texas Instruments* for the investigation and analysis of the signals for the final goal of vital signs monitoring. In the subsequent sections, we will explain the general system parameters of each device used in the experiments.

2.1 Texas Instruments mm-wave radars

In lieu of outstanding advances in the integrated circuit technologies, new ways of system implementation and integration are offered by manufacturers. In fact, the traditional complex systems containing different units and components are designed and developed seamlessly both in hardware and software in a single chip. **TI** offers different mm-wave FMCW radar solutions not only for a particular use but for a variety of applications. Different applications range from proximity sensing, gesture recognition, advanced driving assistance system (ADAS) for low range and middle range, occupancy detection, target localization in 3D, vital signs detection to object identification and classification. There are different demos and applications available in the project repository of *TI* accelerating the design and developments. Some are discussed in Appendix A.

As mentioned in Chapter 1, mm-wave FMCW radar has benefits that cannot be found in any single radar. Firstly, they are smaller and conveniently can be integrated to any spaces such as the front bumper of a vehicle as a part of the parking assistance sensor, which is the feature leveraged from small wavelengths in mm waves. In addition, the prominent property of the FMCW radar is its capability in localization and range discrimination with

a single observation such that other types of sensors could not provide the target range detection.

In addition, TI radars have multiple transceivers for exploiting multiple input multiple output (MIMO) techniques in obtaining the angular information of the objects and facilitating the 3D mapping of the environment. For instance, a flexible binary phase modulation (BPM) and time division multiplexing (TDM) can be used to increase the accuracy of the azimuth and elevation angles' estimations.

For our experiments, we chose a Texas Instruments (TI) mm-wave radar (AWR1443 [2] or AWR1642 [4]) operating from 76-81 GHz. They have built-in digital signal processor (DSP)s and advanced RISC machine (ARM) processor for post-processing. Although the radar can run small applications stand-alone, we did not use it to run our processing on the chip. In fact, after configuring the radar, the chirp samples are transferred over the universal Asynchronous Receiver/Transmitter (UART) interface to a PC to performe signal analysis in Matlab. To work with the radar, evaluation boards of AWR1443 [3] and AWR1642 [5] were used.

AWR1443 has 3 transmitters and 4 receivers and AWR1642 has 2 transmitters and 4 receivers, but we use a single transmitter (Tx)/receiver (Rx) pair for the entire study. According to this great difference between the two radars, the former can detect both azimuth and elevation of the target, while the latter only can detect the azimuth angle. In addition to mm-wave FMCW intrinsic features incorporated in these chips, they borrow the assets of IQ demodulation, which enhance the system performance in comparison to the real demodulation and we will discuss them in the following section.

2.1.1 Benefits of using IQ demodulator

The general architecture of an IQ demodulation and its counterpart, real demodulation, are shown in figure 2.1. In the signal path, without loss of generality, the generator output is a cosine-form signal with a phase $\phi(t)$. The signal goes to the transmit power amplifier (PA) which is connected to the Tx antenna. The echo signal is collected by the Rx antenna and the LNA amplifies the signal. The major difference between the two mixing methods is that the power of the signal is divided between I and Q, while there is no power division in real mixing. The following are the benefits of this structure.

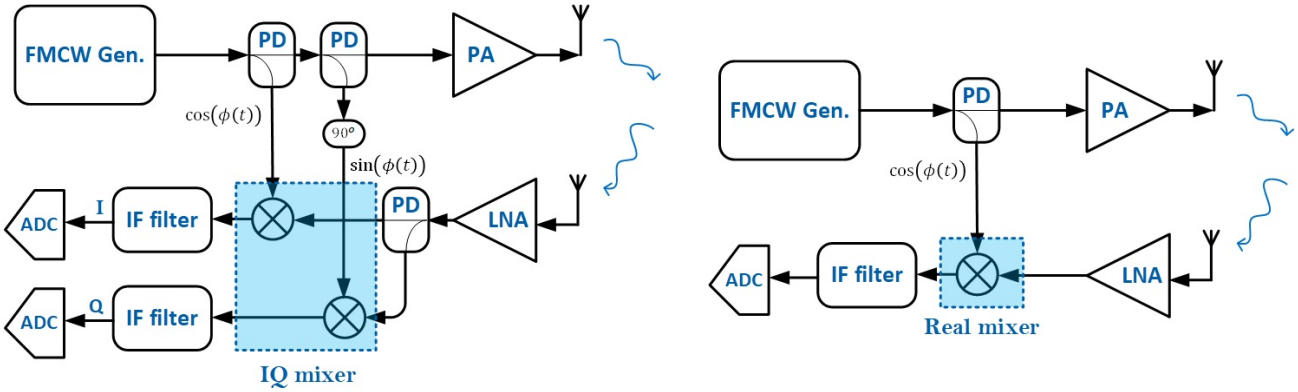

Figure 2.1: IQ demodulation vs real demodulation

SNR improvement

Although, the signal power splitting in the IQ mixing increases the contribution of the IF component noises, the baseband noise due to RF components before mixing is smaller. In fact, if the transmit power coupling between nearby Tx/Rx antennas and the RF cross-talk in the RF circuit are the dominant sources of the noise, then IQ demodulation has 3 dB better SNR. Figure 2.2 explains this claim. Suppose that the reflected wave is the superposition of the chirps with different delays associated with different objects in the environment. Each delay is translated to a frequency shift of the chirp start frequency and can be represented by the frequency components in figure 2.2. This concept is more discussed in 3.1. By real mixing, the positive frequencies are shifted down to the left hand side of DC and the negative frequencies are shifted to the positive side of the based band. During the conversion, the noise level at the baseband is doubled due to overlapping noises of the positive and negative frequencies. In contrast, in IQ mixing, only the positive (or negative) portion of the spectrum is downcoverted keeping the noise level as it is in RF –the IQ mixing shown in 2.1 downconverts the negative frequencies. Thus, there is at most $3dB$ more SNR in the IQ demodulation. Note that the relative magnitude of the peaks in the frequency domain are drawn such that the farther objects have less magnitudes due to more attenuation of the reflected wave –we assume that the radar cross sections (RCS) of all targets are the same.

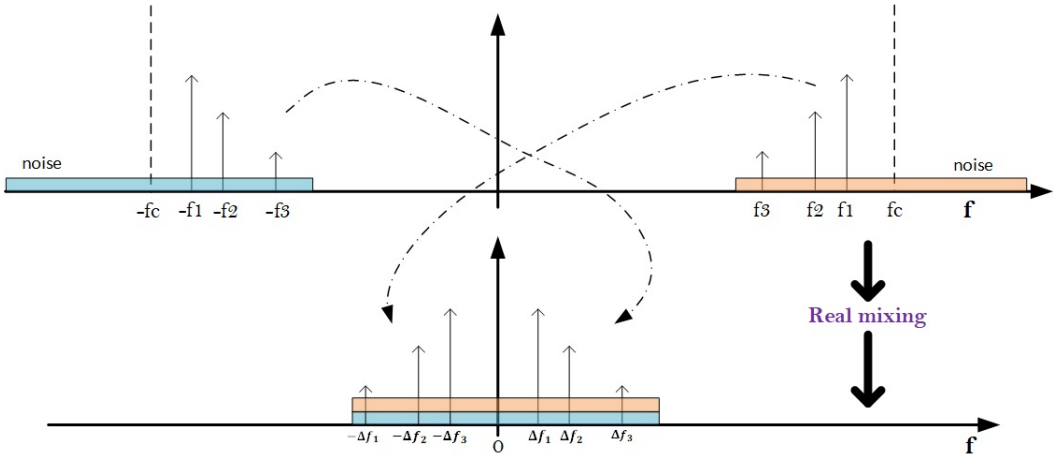

Figure 2.2: Real mixing: $\Delta f_1, \Delta f_2, \Delta f_3$ are corresponding to the downconverted frequencies of $f_1,\ f_2,\ f_3$, respectively.

Noise level estimation

As mentioned before, while the IQ mixing results in an asymmetric spectrum at the based band, this brings a benefit to having a portion of the spectrum[1] containing only noise. Therefore, it can be used for noise power estimation for the signal processing end.

intermodulation reduction

In real mixing, any image or interference out of band can be folded back to the band, which degrades the signal quality at the digital input end. In practice, a portion of the transmit power is coupled to the receiver either through RF corr-talk or antennas. Furthermore, assume that a chirp reflection is received by a target. The delay of the coupled chirp is less than the echo chirp, so the former has a closer start frequency (f_1 in figure 2.3) to the FMCW generator start frequency (f_c in figure 2.3). By considering LNA as a nonlinear component, it produces harmonics close to f_c, which are falling in the same band of the based band by means of real mixing. In figure 2.3, the lowest order in-band intermodulations, which are $\pm 2f_1 \mp f_2$ are illustrated with red peaks in the frequency. The coupled chirp delay is very small, depending on the RF group delays between the generator output and the receiver mixer, such that the intermodulation terms are so close

[1] positive or negative frequencies depends on the mixing

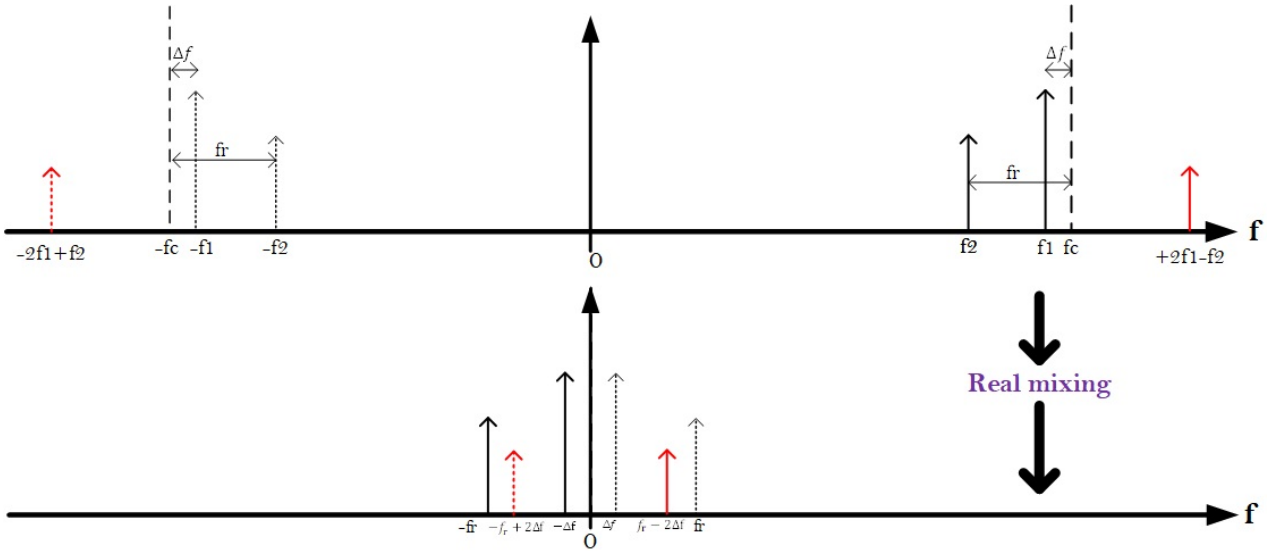

Figure 2.3: Falling intermodulations of the LNA output in the based band: the dotted and solid lines are for negative and positive frequencies, respectively.

to the desired echo chirps. In contrast, in the IQ demodulator, the intermodulation terms are out of band and can easily be filtered.

Range and phase analysis

In the next chapter, the received complex signal of each range bin can be seen as the echo signal in CW radars, but carrying the reflections only from one range. This means that the same problem of optimum/null point detection [43] exists, which can be avoided by using complex demodulation. Otherwise, in real demodulation the relationship between the phase modulation and the basedband signal might not be linear[2].

[2]For clarification, suppose that $cos(\omega_r t + f(t) + \theta_0)$ is received by real demodulation where ω_r, θ_0 are the radian frequency and a constant phase corresponding to the range of a target, and $f(t)$ is the time-dependent delay consisting of the vibration waveform of the target. Thus, after moving it to DC it becomes $cos(f(t) + \theta_0)$. θ_0 determines whether the cosine function can be linearly approximated to $f(t)$ or not. As a matter of fact, the relationship can be non-linear.

Table 2.1: AWR1443 and AWR1642 specifications

Param.	**Tx power**	**min /max Rx gain**	f_c [a]	B_s [b]	**max** K [c]	$f_{b,max}$ [d]	**max range**[e]	**range resolution**	**phase noise**[e]
Value	12 dBm	24/48 dB	71-81 GHz	Up to 4 GHz	100 $MHz/\mu s$	10 MHz	+100 m	3.75 cm	-91 dB/Hz

[a] Start frequency of the ramp
[b] Sweeping bandwidth
[c] Ramp slope
[d] Maximum sampling frequency
[e] For 77-81 GHz at 1 MHz offset

2.1.2 General parameters

Table 2.1 listed some of the important parameters of the radar, which are the same for both AWR1443 and AWR1642. The phase noise is reported at 1 MHz frequency offset, which corresponds to 2.4 m range. The maximum range can be detected theoretically by $f_{b,max} = 10\ MHz/\mu s$ is 150 m, which is fairly long such that the received power is a restriction for the range detection. In fact, the max detectable range is limited by the minimum required SNR 3.

2.2 Hexoskin vest

Figure 2.4: Hexoskin and BioRadio

The Hexoksin vest is a commercial product of *Carre Technologies inc.* [41]. They have wearable smart textiles (figure 2.4) to monitor physiological activities including BR, HR, HRV, tidal volume (v_t), minute ventilation, and hip motion intensity (HMI). The garment

can also record the position of a subject for 6 different postures: standing, sleeping on stomache, back, left, and right sides. The accuracy of the HR and BR estimations for different postures is evaluated by [63]. The authors claimed that the device measures BR and HR for different body postures with 98% accuracy in comparison to the standard laboratory measurement tools. We used this sensor as a reference for comparing our radar results.

Chapter 3

System model and radar analysis

In any radar, the electromagnetic wave is sent into the environment containing various objects. Then the echo of the wave is captured at a receiver. A simplified block diagram of such a system is shown in Figure 3.1a in which both the transmitter and the receiver are at the same location. Each chirp at the output of the FMCW generator is a sinusoid signal whose frequency is swept from f_{min} to f_{max} (figure 3.1b). Here the frequency is swept linearly with a positive slope of K and a duration of T_r implying that the sweeping bandwidth is $B_s = f_{max} - f_{min} = KT_r$. The received signal at the output port of the receiver antenna is amplified and correlated with the transmit signal, which results in a signal called beat signal. The beat signal contains information about the objects in the scene. Particularly, the delay (t_d in figure 3.1b) in the reflected signal is translated to an instantaneous frequency difference between the transmitted and the received chirps.

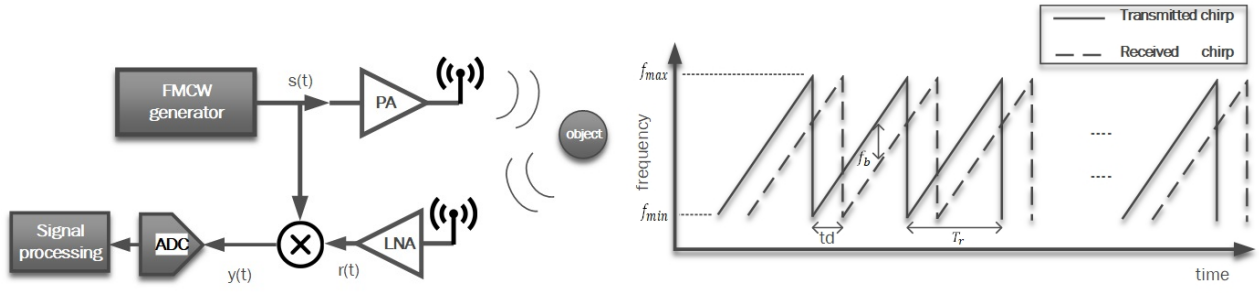

(a) Block diagram of an FMCW radar

(b) Transmitted and received chirp sequences

Figure 3.1: Signal transmission and reception of FMCW chirps

The power amplifier (PA) and the low-noise power amplifier (LNA) at the transmitter and the receiver in Figure 3.1a are non-linear components. One feature of FMCW signals is that they are constant envelope signals with the peak-to-average-power ratio (PAPR) of zero dB, which lets the amplifiers work in their linear region. This adds time-varying delays to the signal even if they are in their linear operation. The time varying delay is much greater than T_r and it manifests itself as a very small Doppler shift in the baseband. This Doppler shift is in slow-time as we will be seen later. In practice, the PA and the LNA delays will diminish after a while when they become thermally stable.

Throughout the entire text, we use the terms "objects" and "targets" interchangeably to imply that for the purpose of discussing the signal properties, it is not important whether the signal is reflected off a desired object or a clutter.

3.1 FMCW radar fundamental principles

The complex chirp signal is [28]:

$$s(t_f) = A_t \exp\left(j(2\pi f_{min} t_f + \pi K t_f^2 + \phi_n(t_f))\right), \quad 0 < t_f < T_r, \tag{3.1}$$

where A_t related to the transmit power, f_{min} is the start frequency (and λ_{max} is the corresponding wavelength), and t_f is the fast time, which can be in $[0, T_r]$. In fact, in writing equations we should distinguish between the time that is within a chirp period or the time that is within the physical displacement of the target. Also, ϕ_n is the phase noise of the generator. we assume that for a single target when the thermal noise and any other RF imperfections are ignored, the echo signal is a delayed version of the transmitted chirp in (3.1):

$$r(t_f, t_s) = A_r \exp\left[j\left(2\pi f_{min}(t_f - t_d(t_s)) + \pi K(t_f - t_d(t_s))^2 + \phi_n(t_f - t_d(t_f))\right)\right], \tag{3.2}$$

where $t_d(t_f)$ is the round-trip time (RTT) delay of the wave which is a function of the the slow time t_s meaning that the delay changes over time are greater than T_r. Thus, again we should emphasize that t_f and t_s must be distinguished.

We suppose that there is only a single small object positioned at a nominal distance of R_0 to the radar but it is moving from R_0, which results in a time-varying distance to the radar. This time-varying delay should vary the order greater than T_r, if it is not, the chirp duration should be smaller to meet the criterion. This assumption is very important will be shown later. Let us denote this time-varying distance by $R(t_s) = R_0 + x(t_s)$, where $x(t_s)$

is a function represents the distance variations. Furthermore, $t_d(t_s) = 2R(t_s)/c$, where c is the light speed throughout the whole text. As illustrated in Figure 3.1a, the beat signal is the result of the received and transmit chirp product, i.e. $y(t_f, t_s) = s(t_f)\, r^*(t_f, t_s)$. By plugging $t_d(t_s)$ into (3.2) and doing some manipulation, y can be expressed as:

$$
\begin{aligned}
y(t_f, t_s) &= A_r A_t \exp\Big[j \big(2\pi K t_d(t_s) t_f + 2\pi f_{min} t_d(t_s) - \pi K t_d^2(t_s) + \\
&\quad \phi_n(t_f) - \phi_n(t_f - t_d(t_s)) \big) \Big], \\
&= A_r A_t \exp\Big[j \Big(2\pi f_b\, t_f + \frac{4\pi K}{c}\, x(t_s)\, t_f + \Big(\frac{4\pi}{\lambda_{max}} - \frac{8\pi K}{c^2} R_0 \Big) x(t_s) \\
&\quad - \frac{4\pi K}{c^2} x^2(t_s) + \theta_0 + \theta_1 + \phi_n(t_f) - \phi_n(t_f - t_d(t_s)) \Big) \Big], \qquad (3.3) \\
f_b &:= \frac{2K R_0}{c}, \qquad \lambda_{max} := \frac{f_{min}}{c}, \qquad \theta_0 := \frac{4\pi R_0}{\lambda_{max}}, \qquad \theta_1 := -\frac{4\pi k R_0^2}{c^2} \qquad (3.4)
\end{aligned}
$$

Fourth and fifth terms in the exponential argument in (3.3) can be neglected because typically, K/c^2 is in the order of 10^{-4} (refer to the values in table 2.1). Thus, θ_1 is approximately equal to zero. The second term in (3.3) can be very small by considering t_f, t_s values. We suppose a scenario in which the target has a radial velocity of $100\, m/s$. If $T_r = 10^{-5}$, then $\Delta x = x(T_r) - x(0)$ is approximately equal to $1 cm$. Hence, during one chirp, the coefficient in the second term would be around 10^{-3} and can be ignored. Similarly, if the target is vibrating with f_v frequency and a maximum physical displacement of $1\, cm$, then the maximum Δx during one chirp would be very small depending on the choice of T_r[1]. Therefore,

$$
\begin{aligned}
y(t_f, t_s) &\approx A_r A_t \exp\Big[j \Big(2\pi f_b\, t_f + \frac{4\pi}{\lambda_{max}}\, x(t_s) + \theta_0 + \Delta\phi_n(t_f, t_s) \Big) \Big] \qquad (3.5) \\
\psi(t_f, t_s) &= 2\pi f_b\, t_f + \frac{4\pi}{\lambda_{max}}\, x(t_s) + \theta_0 + \Delta\phi_n(t_f, t_s), \qquad (3.6) \\
\Delta\phi_n(t_f, t_s) &= \phi_n(t_f) - \phi_n(t_f - t_d(t_s)),
\end{aligned}
$$

In fact, $\Delta\phi_n(t_f, t_s)$ is the result of the *range correlation* [19] by which the effective phase noise for the beat signal depends on the distance of the object. For instance, the closer

[1] Suppose that $x(t_s) = A_v cos(2\pi f_v t_s)$. If $f_f = 1/T_r$, then $t_s = n/f_f$. Though, it can be shown that the maximum $\Delta x = x(n+1) - x(n)$ is $A_v(2\pi f_v/f_f)$. Because this maximum is in the order of 10^{-5}, the second term in the phase of the exponential function in (3.3) is almost zero.

the target is ($t_d \approx 0$), the lower the phase range is. It is straightforward to obtain power spectral density (PSD) of $\Delta\phi_n(t_f, t_s)$ as a function of the PSD of $\phi_n(t_f, 0)$ by assuming that the target is stationary and is located at R_0, and ϕ_n is wide sense stationary (WSS):

$$S_{\Delta\phi}(f) = 4S_{\phi}(f)\ \ sin^2\left(\frac{2\pi R_0}{c} f\right) \tag{3.7}$$

The PSD in 3.7 increases as the range of the target increases. According to the dependency of the target range on the instantaneous frequency difference of the echo chirp and the transmitted chirp (see figure 3.1b), the farther the object is, the more the frequency shift is. In fact, it is true that the range correlation effect diminishes for longer ranges, but, fortunately, in FMCW radars the phase noise power is less for the longer ranges since the frequency offset to the start frequency (f_{min}) is greater. In other words, even though if there is no range correlation at a distant range,[2] the phase noise power is much less than the near objects. This also raises the need for minimizing the delay through the transmit and receive paths to maintain the lowest possible phase noise effect at the output of the mixing at the receiver.

3.2 Radar equation and received signal power

If the P_t is nominal transmit power and the target is at a distance of R, then the received power is related to the transmit power of a radar by the following [17]:

$$P_r = \frac{P_t G_t G_r \sigma \lambda^2}{(4\pi)^3 R^4} \tag{3.8}$$

where G_t, and G_r are the transmit and the receive antenna gains, respectively. σ is the radar cross section (RCS) of the target [3]. Also, λ is the wavelength of the travelling wave. For physiological motion, the area under which the chest moves determines the RCS. Equation (3.8) is known as the radar equation. We assume that the room temperature is 300 Kelvin (or about 25 Celsius) and the transmit chirp has a sweeping bandwidth of 4 GHz, then the noise power at the output terminal of the receiver antenna is $P_n = 10\ log_{10}(KTB_s) \approx -103\ dB$ in which K is Boltzmann's constant [4]. In addition, if the

[2] because the frequency shift with respect to f_{min} is high

[3] RCS is a hypothetical area required to intercept the power density at the target such that if the total reflected power is scattered isotropically, the power density at the Rx is achieved.

[4] $K = 4.138 \times 10^{-23}\ J/K$. Do not confuse this K with the chirp slope.

receiver noise figure (NF)[5] is NF dB and the minimum SNR required at the based band is denoted by SNR_{min}, then the minimum received signal power at the output port of Rx antenna will be $P_{r,min} = NF + P_n + SNR_{min}$ in which NF is the noise figure and all the variables are in dB. By using (3.8), which relates P_r to the target range, the maximum range versus minimum required SNR at the based band can be obtained:

$$R_{max} = \sqrt[4]{\frac{P_t G_t G_r \sigma \lambda^2}{P_{r,min}(4\pi)^3}}, \quad P_{r,min} = NF + P_n + SNR_{min} \tag{3.9}$$

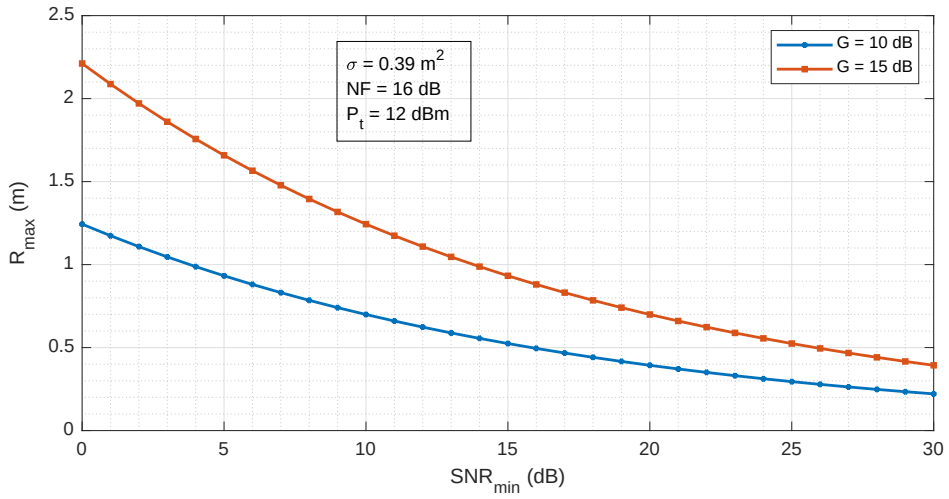

Figure 3.2: Maximum range of a target versus minimum required SNR at the based band. The gain of Tx/Rx antennas are the same as G.

In figure 3.2, R_{max} is plotted versus minimum SNR with values annotated. In fact, $\sigma = 0.39m^2$ is an approximate value for a human as mentioned in [29]. The transmit power of 12 dBm is the output power of AWR1642/AWR1443 chips (see table 2.1).

3.2.1 Complex signal analysis

Furthermore, $\psi(t_f, t_s)$ in (3.6) varies with $x(t_s)$ relative to λ_{max}. So, the phase variations in the scale of the maximum wavelength can greatly change the beat signal phase. For

[5]Noise figure is defined as the ratio between the input SNR to the output SNR of a circuit component.

example, a radar operating at 6 GHz is 10 times less sensitive in comparison to a 60 GHz radar. Thus, as a rule of thumb, the phase power for the same amount of physical displacement is 20 dB more in mm-waves.

This equation is used to detect the range of a subject, R_0. To this end, an FFT is applied over samples of a chirp to obtain the spectrum of the beat signal, which has peaks corresponding to the subjects at different ranges. This FFT reveals range information so it is called range FFT. Each range FFT bin represents a particular distance with an associated phase similar to $\psi(t)$.

The basedband signals $y(t_f, t_s), \psi(t_f, t_s)$ (in (3.5) and (3.6)) are sampled in the **fast time** by the sampling frequency of $f_{b,max}$ (see table 2.1), though $t_f = n/f_{b,max}$. In the **slow time**, if each chirp is sent every T_c, then the sampling frequency will be $f_c = 1/T_c$, though $t_s = m/f_c$. By replacing the discrete times in (3.5) and (3.6), the discrete form of the signals will be obtained i.e. $y[n, m]$, $\psi[n, m]$.

Range detection

We suppose that within each chirp period the number of samples is N, then f_b in 3.4 can be estimated by means of peak searching in the FFT domain of $y[n, m]$ over **fast time** samples (with index n and FFT size of N). From that, an estimate of the target, R_0, will be obtained. The following theorem proves that in an AWGN channel, $\hat{f}_b$ is optimum in ML sense when it is the maximum frequency component of $y[n, m]$, when there is a single target in the radar field of view (FOV). Also, note that A_r is (3.5) is not Rayleigh distributed as usual wireless channels therein the assumption of the dense scattering environment is a premise [37]. In contrast to them, here the channel is not a rich scattering environment due to having limited number of reflectors at a distance R_0. Thus, A_r is not magnitude of a zero mean complex Gaussian random variable. The following proves the optimality of the range detection by simple peak frequency detection of $y[n, m]$.

Theorem 3.2.1 (optimality of range detection) *If $y[n]$ and $Y[m]$ are a discrete signal and its FFT $\forall m, n = 0, \cdots, M-1$, $w[n]$ is an i.i.d. complex Gaussian random process with zero mean, and $x_p[n]$ is in $\{e^{j\frac{2\pi}{M}pn} \mid p = 0, \cdots, M-1\}$, such that:*

$$y[n] = x_p[n] + w[n]$$

then, the maximum estimation of p is:

$$\hat{p} = \underset{m}{\operatorname{argmax}} \left| Y[m] \right| \tag{3.10}$$

Proof: *The problem is to find a* $x_i[n]$ *such that the following will be satisfied in an interval of* M *samples:*

$$\max_i \; p_r \left(y[n] \middle| x_i[n] \right) \tag{3.11}$$

in which p_r *is the conditional probability. (3.11) is maximum likelihood (ML) criterion and it is optimum when all possible* $x_i[n]$ *can happen with equal probability and equal power. ItEven though can be shown that (3.11) is equivalent to the minimum Euclidean distance criterion between* $y[n]$ *and* $x_i[n]$*. Then (3.11) is equal to the following:*

$$\max_i \left| \sum_{n=0}^{M-1} y[n] x_i^*[n] \right| = \max_i \; R\left(y[n], x_i[n] \right) \tag{3.12}$$

and R *is the cross-correlation function between the two sequences in its argument. It is enough to show that the following is true:*

$$\underset{i}{\text{argmax}} \left| \boldsymbol{Y}^T \boldsymbol{e}_i \right| = \underset{i}{\text{argmax}} \; R\left(y[n], e^{-j\frac{2\pi i n}{M}} \right) \tag{3.13}$$

where $\boldsymbol{Y}$ *is a vector containing frequency samples of* $y[n]$ *from discrete-time Fourier transform (DFT).* $\boldsymbol{e}_i$ *is a vector having only one at the i'th position. We start to expand the inner argument of the left-hand side of the equation:*

$$\boldsymbol{Y}^T \boldsymbol{e}_i = DFT\left(y[n] \circledast e^{j\frac{2\pi n}{M} i} \right) \tag{3.14}$$

$$= DFT\left(\sum_{l=0}^{M-1} y[l] e^{j\frac{2\pi i}{M}(n-l)} \right) \tag{3.15}$$

$$= \frac{1}{M} \sum_{n=0}^{M-1} \left[\sum_{l=0}^{M-1} y[l] e^{j\frac{2\pi i}{M}(n-l)} \right] e^{-j\frac{2\pi}{M} nk} \tag{3.16}$$

$$= \sum_{l=0}^{M-1} y[l] e^{-j\frac{2\pi}{M} il} \sum_{n=0}^{M-1} \frac{1}{M} e^{-j\frac{2\pi n}{M}(i-k)} \tag{3.17}$$

$\circledast$ *is a circular convolution is used to convert frequency multiplication to time-domain convolution. In (3.16),* k *is the index of FFT and* l *is the index of convolution. After interchanging the summation orders in (3.16), (3.17) is obtained in which the second summation is* $\delta(i-k)$*. By replacing it in (3.17), the theorem is proved.*

By the *Nyquist* sampling theorem, $f_{b,max}/2$ should be greater than or equal to f_b to be able to detect f_b (or the range of the target). Therefore, the maximum unambiguous detectable

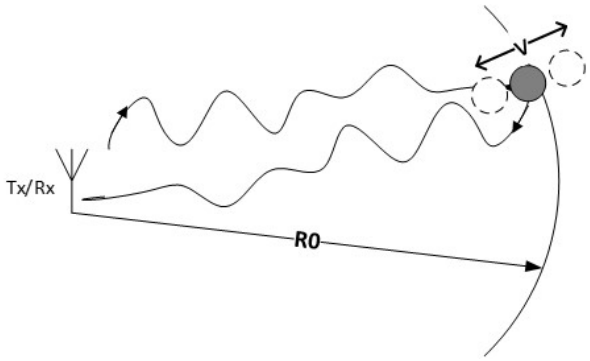

Figure 3.3: Radial velocity with respect to the radar

range will be $R_{max} = f_{b,max}/2K$, which is followed from 3.4. Also, the range resolution, which is the minimum resolvable distances, is $R_{min} = f_b c/2NK = c/2B_s$, where B_s is the sweeping bandwidth.

Radial displacement

After applying FFT on $y[n, m]$ over n indexes and removing the f_b frequency, the resulting signal is the slow time variation of y i.e. $\tilde{y}[m] = \text{FFT}_n(y[n, m])$. In addition, because $\phi_n[n]$ is WSS, so without loss of generality, we set $n = 0$. Thus,

$$\tilde{y}[m] = A_r A_t \exp\left[j\left(\frac{4\pi}{\lambda_{max}} x[m] + \theta_0 + \Delta\phi_n[m]\right)\right] \tag{3.18}$$

$$\tilde{\psi}[m] = \frac{4\pi}{\lambda_{max}} x[m] + \theta_0 + \Delta\phi_n[m] \tag{3.19}$$

where $\Delta\phi_n[m] = \Delta\phi_n[0, m]$. Two cases are of interest for $x[m]$ function. Here, we investigate when the target has a radial velocity of v with respect to the radar (Figure 3.3) and when it is modelling the vibration of the target. In Figure 3.3, the target is moving towards or away from the radar determining the sign of v in $x[m] = vt_s = mv/f_c$. Hence, $\tilde{y}[m]$ is a periodic signal with $\omega_r = 4\pi v/\lambda_{max} f_c$, which is the normalized radian frequency. So, again by taking the second FFT across the detected range bin samples, an estimate of ω_r can be obtained. In fact, f_c should be high enough such that $|\omega_r| \leq \pi$. It is interesting to note that in ω_r, the velocity is measured with respect to λ_{max} implying that the sensitivity to the minimum detectable velocity of the radar is managed by its operating frequency. For example, at 77 GHz and $v = 1mm/s$, then $\omega_r = 3.22\ Rad/s$ if $f_c = 1\ Hz$. In contrast, the maximum velocity should be $f_c/(4\lambda_{max})$ such that the Nyquist condition is satisfied.

Vibration displacement

If the target is vibrating around R_0 instead of moving away or towards the radar, then $x[m] = A_v cos(\omega_v t_s)$. By substituting it to 3.18, then:

$$\tilde{y}[m] = A_r A_t \exp\left[j\left(\frac{4\pi}{\lambda_{max}} A_v cos(\omega_v / f_c) + \theta_0 + \Delta\phi_n[m]\right)\right] \tag{3.20}$$

$$= A_r A_t e^{j(\theta_0 + \Delta\phi_n[m])} \sum_{l=-\infty}^{\infty} j^l J_l\left(4\pi \frac{A_v}{\lambda_{max}}\right) e^{jl\,\omega_v} \tag{3.21}$$

the second equality is the result of the *Fourier Series* (FS) expansion of the right hand side equation in 3.20. J_l is the l'th order Bessel function of the first kind. Though, in the frequency domain, the vibration produces many harmonics make the spectral estimation of the ω_v inaccurate where J_l is not necessarily decreasing as l increases. So, for instance, if there is a maximum peak at f_{v1} it might be for a harmonic $l > 1$ rather than the fundamental vibration frequency. The problem of estimating the fundamental vibration frequency is more discussed in 3.4.

In fact, for vital signs detection application, $x[m]$ can be a function models the chest wall displacement of a subject. As it is vibrating due to the heartbeat and exhalation or inhalation, it is a periodic function [28]. In that case, two vibrating objects at the same location modulating $\tilde{\psi}[m]$. Thus the phase of the complex signal in 3.18 contains two periodic signals. As a result, the FS expansion of each periodic signal will be multiplied producing many harmonics. So practically, estimating the two vibration frequencies becomes infeasible. In next, we will provide a brief explanation about the two vibrating cases to highlight some important points that are needed to be considered during analyzing the vital signs.

To monitor respiration and heart rates, the chest wall can be modeled as two vibrating objects with different frequencies and different magnitudes. Suppose that f_b, f_h, A_b, A_h are BR, breathing amplitude, HR, and heart amplitude, then the phase of $\tilde{y}[m]$ will be:

$$\tilde{\psi}[m] = \theta_0 + \frac{4\pi}{\lambda_{max}} A_b cos\left(2\pi \frac{f_b}{f_c} m\right) + \frac{4\pi}{\lambda_{max}} A_h cos\left(2\pi \frac{f_h}{f_c} m\right) + \Delta\phi_n[m] \tag{3.22}$$

[43] showed that $\tilde{y}[m]$ with the phase in 3.22 will produce so many harmonics as well as DC terms in real and imaginary parts. We will investigate the DC problem in phase analysis, the DC terms due to vibrations do not have a detrimental effect on extracting the phase of $\tilde{y}[m]$ because they have resulted in by the desired phase modulation of the vital signs.

3.3 DC compensation process

The received signal in the form of (3.18) does not have DC term. However, in practice, there are reasons for having DC terms in the reflections. As [29] mentioned, there are four main sources of generating the DC:

- Leakage between Tx and Rx antennas [70]
- RF cross-talk between Tx and Rx paths [70]
- Stationary clutters [29]
- Phase modulation by a vibrating object [43]

The result of the DC in the complex plane is that the signal constellation is shifted from the origin to a new point $\boldsymbol{x}$ ($\boldsymbol{x} = [dc_r \;\; dc_i]^T$). In Figure 3.4, a constellation shift is apparent in the point cloud before DC compensation. If there are any DC terms rather than the phase modulation, then they should be removed or minimized before the phase analysis otherwise in the phase domain there will be so many harmonics. In contrast, the phase modulation itself results in a DC and it must not be removed since it is a part of the phase modulation. Therefore, there is a challenge to keep the desired DC term while removing unwanted DCs. Practically, this can not be achieved while there is no mean to distinguish the two sources of the CD generators. If the unwanted DC term is $d_i + jd_q$, the phase is corrupted and it is shown by the following manipulations:

$$\tilde{\psi}_{DC}[m] = \arctan\left(\frac{Q[m] + d_q}{I[m] + d_i}\right) \tag{3.23}$$

in which $Q[m]$, and $I[m]$ are the imaginary and real parts of the DC-free signal in (3.18). (3.23) can be expressed as a Taylor series expansion around the desired point i.e.:

$$\tilde{\psi}_{DC}[m] \approx \arctan\left(\frac{Q[m]}{I[m]}\right) + \frac{1}{1 + \left(\frac{Q[m]}{I[m]}\right)^2}\Delta\psi[m] - \frac{\frac{Q[m]}{I[m]}}{\left(1 + \left(\frac{Q[m]}{I[m]}\right)^2\right)^2}\Delta\psi^2[m] + o\left(\Delta\psi^2[m]\right), \tag{3.24}$$

$$\Delta\psi[m] := \frac{Q[m] + d_q}{I[m] + d_i} - \frac{Q[m]}{I[m]}, \tag{3.25}$$

The first term in the right hand side of (3.24) is the desired phase while the other terms are the harmonics and intermodulations caused by the DC. It is straightforward to replace

$Q[m]$ and $I[m]$ by $\sin\tilde{\psi}[m]$ and $\cos\tilde{\psi}[m]$, respectively, and use the trigonometric identities to obtain an equivalent equation like below:

$$\tilde{\psi}_{DC}[m] \approx \tilde{\psi}[m] + \frac{1}{2}\left(1+\cos(2\tilde{\psi}[m])\right)\Delta\psi[m] + \left(\frac{1}{8}\sin(4\tilde{\psi}[m]) + \frac{1}{4}\sin(2\tilde{\psi}[m])\right)\Delta\psi^2[m] + o\left(\Delta\psi^2[m]\right) \tag{3.26}$$

This equation reveals the fact that the phase has similar harmonics as in (3.21).

The center and the radius of the cloud in Figure 3.4 can be estimated based on a non-linear least square estimation (NLLS). Let us denote each complex point as a column vector whose first and second elements are real and imaginary parts of the point, respectively. Furthermore, assume $\boldsymbol{a}_i$, $\boldsymbol{x}$, r are the i'th point, hypothetical centre point and the radius, respectively. For finding an estimate of the centre point and the radius we solve the following NLLS problem[6]:

$$\begin{aligned} P &= \min_{\boldsymbol{x},r} \sum_{i=1}^{N} \left(\| \boldsymbol{x} - \boldsymbol{a}_i \|^2 - r^2\right)^2 \\ &= \min_{\boldsymbol{x},r} \sum_{i=1}^{N} \left(\| \boldsymbol{x} \|^2 - 2\boldsymbol{a}_i^T x + \| \boldsymbol{a}_i \|^2 - r^2\right)^2 \end{aligned} \tag{3.27}$$

N is the number of samples. The last summation resembles the second norm of a vector. By rearranging the inner bracket terms and putting unknowns in a vector, $\boldsymbol{y}$, and known variables in a vector $\boldsymbol{b}$ the following equation can be obtained:

$$P = \min_{y} \quad \| A\boldsymbol{y} - \boldsymbol{b} \|^2 \tag{3.28}$$

$y = [R \ \boldsymbol{x}^T]^T$, $R = \| \boldsymbol{x} \|^2 - r^2$, and $A, \boldsymbol{b}$ are:

$$A = \begin{bmatrix} 1 & -2\boldsymbol{a}_1^T \\ 1 & -2\boldsymbol{a}_2^T \\ \vdots & \vdots \\ 1 & -2\boldsymbol{a}_N^T \end{bmatrix}, \boldsymbol{b} = \begin{bmatrix} -\| a_1 \|^2 \\ -\| a_2 \|^2 \\ \vdots \\ -\| a_N \|^2 \end{bmatrix} \tag{3.29}$$

A is a full column rank matrix for $N > 3$, thus has a left inverse of $A^\dagger$ and the optimum solution is:

$$\boldsymbol{y}^* = A^\dagger \boldsymbol{b} = (A^T A)^{-1} A^T \boldsymbol{b} \tag{3.30}$$

[6]This method is known as compressed sensing method for estimating and tracking the centre and the radius of an arc [13].

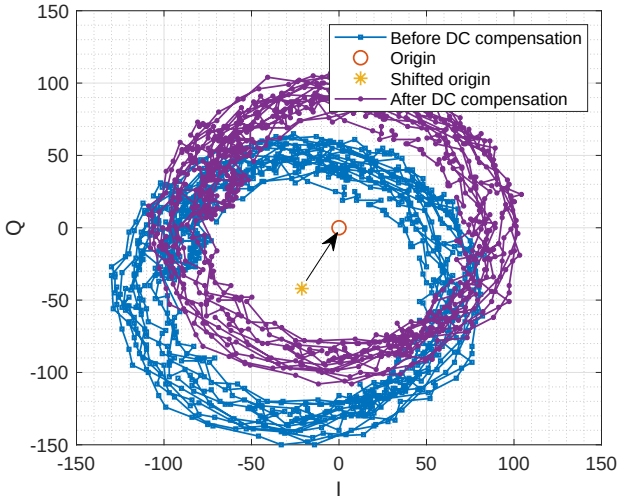

Figure 3.4: Correction of the received complex signal.

The optimum solution of P in (3.27) is equal to the optimum solution in (3.28) when $r = \| \boldsymbol{x} \|^2 - R > 0$. By contradiction, if $r < 0$ and $\boldsymbol{y}^* = [R \; \boldsymbol{x}^T]^T$ is optimum the following shows $\boldsymbol{y}^*$ is not optimum:

$$\begin{aligned} 0 \leq \| \boldsymbol{x} - \boldsymbol{a}_i \|^2 &= \| \boldsymbol{x} \|^2 - 2\boldsymbol{a}_i^T \boldsymbol{x} + \| \boldsymbol{a}_i \|^2 \\ &< R - 2\boldsymbol{a}_i^T \boldsymbol{x} + \| \boldsymbol{a}_i \|^2, \qquad \forall i \end{aligned} \tag{3.31}$$

therefore each term of the summation in (3.27) with $\boldsymbol{y}^*$ is greater than when $y = [\| \boldsymbol{x} \|^2 \quad \boldsymbol{x}^T]^T$ implying that r has to be zero. Figure 3.4 is obtained for the actual vital signs' waveforms. The *mm* sensitivity makes the complex signal trajectory in Figure 3.4 a complete circle. This is the result of the phase dependency on the relative chest movement to the wavelength causing a great phase change only for displacements in the range of *mm*.

3.4 Phase analysis

In section 3.2.1, we represented that the complex received signal modulated with two vibrating objects at the same range has too many harmonic components. Instead, for vital signs application, we recommend to use phase analysis (or traditionally known as *arctan* demodulation) in order to reduce higher order harmonics of the breathing on the heartbeat band.

Suppose that the received basedband complex signal has zero phase meaning that it is real, a. If a complex noise, $n(t) = n_c(t) + jn_s(t)$, is added to the signal, then it deviates the actual phase of the received complex sample by $\Delta\theta$:

$$y(t) = a + n_c(t) + jn_s(t) = a + n(t) = a + B_n e^{j\theta_n(t))}$$

$$\theta_y(t) = tan^{-1}\left(\frac{n_s(t)}{a + n_c(t)}\right) \approx tan^{-1}\left(\frac{n_s(t)}{a}\right) \tag{3.32}$$

$$\theta_y(t) \approx \frac{n_s(t)}{a} \tag{3.33}$$

3.32 is approximated when $n_c(t)$ is much smaller than a, though the noise shifts the phase by:

$$\theta_y(t) \approx \frac{B_n}{a} sin(\theta_n(t)) \tag{3.34}$$

B_n is the magnitude of the noise. The power of the $\theta_y(t)$ is the squared expectation of it and since it is zero mean, then:

$$E(\Delta\theta^2) \approx \frac{1}{2}\frac{\sigma_n^2}{a^2} \tag{3.35}$$

where σ_n^2 is the noise power, and σ_n^2/a^2 is the inverse of SNR. Therefore, as SNR increases, the phase deviation due to the noise decreases.

In practice, the phase is calculated by $\tan^{-1}$ function which outputs phases in $[-\pi, \pi]$. If $\psi[m]$ in equation (3.5) is sampled with an appropriate sampling time of T_c then it is possible to maintain the phase difference between two consecutive samples less than π. Equivalently, $x(t_s)$ (in (3.3)) must not change more than $\lambda_{max}/4$ within T_c period. If this assumption is satisfied, any phase change greater than π indicates that the phase should be corrected by adding or subtracting 2π. This process is called *phase unwrapping*. In other words, there should be at least three phase samples in $[-\pi, \pi]$ to be able to recover the phase, which is modulated by a physical displacement.

We should do the phase unwrapping across the phases on a range bin where the target is sat. Let us denote the phase sequence as ϕ_n for $n = 1, \cdots, M$, namely M is the size of the vibration FFT. For every pair of (ϕ_n,ϕ_{n+1}), we know that $|\phi_{n+1} - \phi_n|$ should not be greater than π. If it is then a phase correction must be applied. The phase correction is accomplished as bellow:

- $\phi_{n+1} - \phi_n > \pi$: means that $\phi_{n+1} > 0$ and $\phi_n < 0$. As illustrated in Figure (3.5, left), it seems the target followed the path shown in the red color just in T_c period. However, with our assumption it should pass the green path, which is shorter and it is less than π. To achieve so, 2π must be subtracted from ϕ_{n+1}.

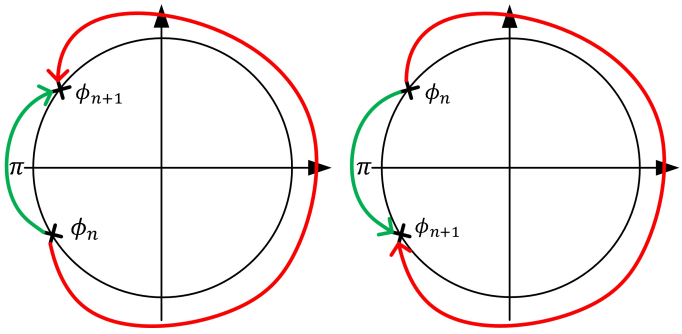

Figure 3.5: Phase jump cases: phase difference of greater than π (left), phase difference of less than $-\pi$ (right). The red lines are the unacceptable paths for phase change while the green lines are the acceptable paths.

- $\phi_{n+1} - \phi_n < -\pi$: means that $\phi_{n+1} < 0$ and $\phi_n > 0$. Similarly, in Figure (3.5, right) it is shown that the target followed the long path with the red color while the correct one is the shorter one. To correct, this time 2π must be added to ϕ_{n+1}.

The whole process must be done in a sequence starting with n=1 and ending with n=M-1. At each iteration, ϕ_{n+1} is only updated. The algorithm 1 explains the process.

Algorithm 1 Phase unwrapping procedure

r is the desired detected range index $\boldsymbol{r}_{desired} = R(:, r)$ (R is the *range-slow time* matrix and Matlab syntax is used to select the r'th column) $\boldsymbol{\phi} = tan^{-1}(\boldsymbol{r}_{desired})$ **for** *n=1:M-1* **do**

```
if φ_{n+1} − φ_n > π then
    φ_{n+1} = φ_{n+1} − 2π;
else if φ_{n+1} − φ_n < −π then
    φ_{n+1} = φ_{n+1} + 2π
else
    Do nothing
end
```

Figure 3.6a shows an example of a phase function before wrapping, after wrapping and after applying the unwrapping process in algorithm 1. In this example, the phase magnitude is growing exponentially with fixed sampling frequency. The growing magnitude increases the phase difference between consecutive samples gradually. Thus, it can be seen that the phase unwrapping process fails when there is less than 2 samples in $[-\pi, \pi]$. One

way to correct unwrapping for a sparse sampled phase, which may happen when the object moves faster than it should, is to upsample the complex signal. By upsampling, we add more samples between I and Q samples. Thus, there will be more phase samples helping to have more change to unwrap the phase properly. As an illustration, in figure 3.6b, the phase is upsampled with a factor of 4 so that it is possible to recover the phase even when the phase without upsampling could not be properly unwrapped.

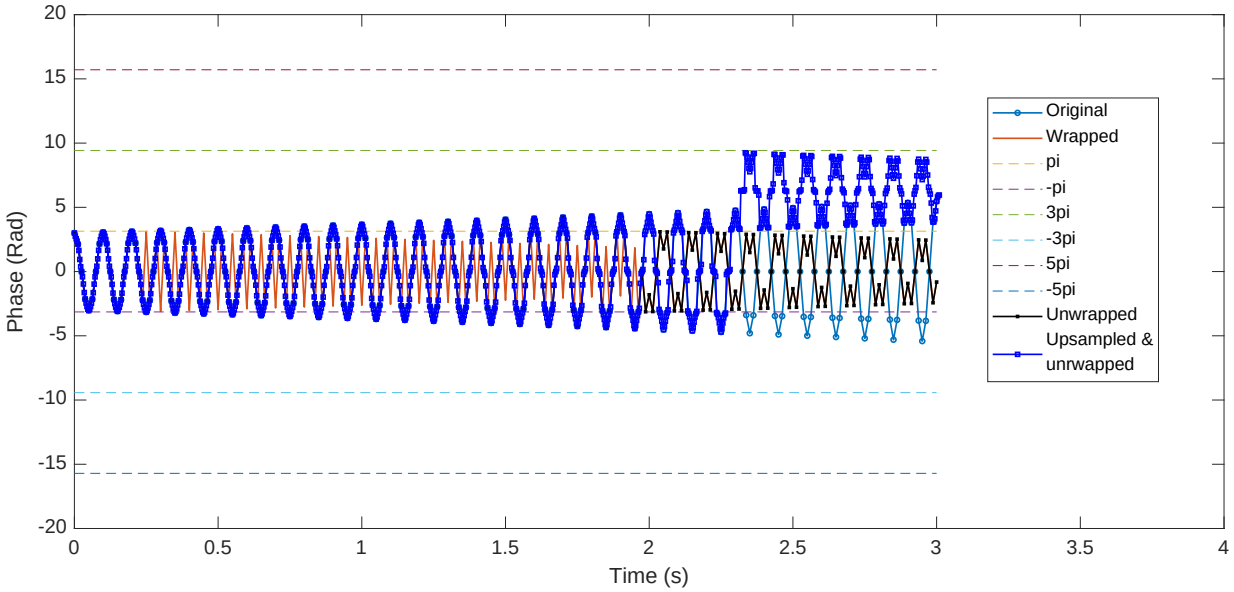

(a) Before $t = 0.25s$, there is no need for phase unwrapping. Also, the phase correctly unwrapped before $t = 2\,s$ either for the phase with the original sampling rate or for the upsampled phase. But the upsampled phase is correctly unwrapped until $t = 2.18s$.

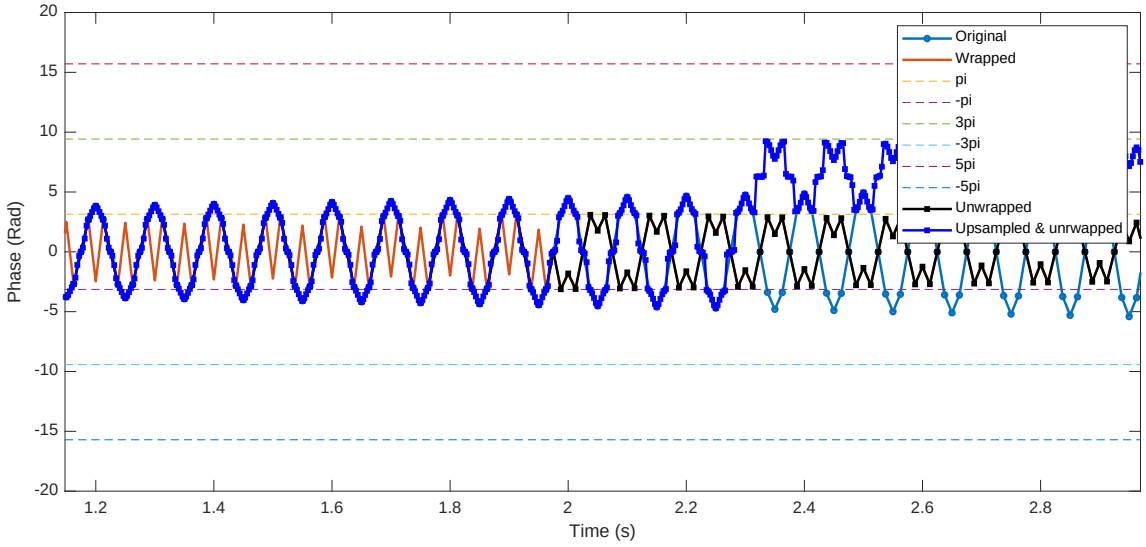

(b) Zoomed-in figure 3.6a

Figure 3.6: Phase unwrapping test

3.5 Harmonic analysis

After unwrapping $\tilde{\psi}[m]$ in (3.19), a quasi-periodic signal will be obtained. The signal could not be an exact periodic signal because of additive noise (see (3.35)), phase noise, and imperfect DC compensation. For vital signs detection, the received phase is a superposition of two periodic signals. Hence, the problem turns out to be fundamental frequency estimation from a mixture of periodic signals i.e. multi-pitch processing. Commonly the problem is addressed in many fields such as speech recognition and compression, image compression and feature extraction. In literature, there are many different approaches to estimate the fundamental frequencies of a signal [27]. Among them, we choose harmonic multiple signal classification (HMUSIC) methods presented in [24], [25] and [10]. We use their final results, so for more details refer to the papers. Here we will describe the problem in vital signs monitoring terminology as well as additional discussions on the noise.

Let us assume that we have K quasi-periodic signals in the observed signal $x(t)$ corresponding to the breathing and heart signals. Each quasi-periodic signal can be expressed as follows:

$$x_k[n] = \sum_{l=1}^{L_k} a_{k,l} e^{j\omega_k l n} + e_k[n] \tag{3.36}$$

$a_{k,l}$ is the complex coefficient of the k'th signal component and l'th harmonic order. Correspondingly, ω_k is the fundamental radian frequency of the k'th component. Each periodic signal has its own noise, $e_k(n)$, which is uncorrelated (in the case of complex Gaussian noise they are also independent). L_k is the model order of the k'th component. Also note that the complex coefficients are not varying with time and they are $a_{k,l} = A_{k,l} e^{j\phi_{k,l}}$ with $A_{k,l}$ is a positive constant and $\phi_{k,l}$ is uniformly distributed in $[-\pi, \pi]$. The received signal is a superposition of individual signal components:

$$x[n] = \sum_{k=1}^{K} x_k[n] = \sum_{k=1}^{K} \sum_{l=1}^{L_k} a_{k,l} e^{j\omega_k l n} + e[n] \tag{3.37}$$

where $e[n]$ is the aggregated noise of all components. For the vital signs signal, there are only two components of breathing and heart signals, so $K = 2$. By taking M signal samples, we define a vector $\boldsymbol{x}[n] = [x[n], x[n-1], \cdots, x[n-M+1]]^T$. An important note is that this method is a prediction method based on M previous samples. M should be at least equal to the longest period in (3.37) corresponding to the smallest fundamental frequency. It is interesting to note that M is the order model in auto regressive (AR) for (3.37) but the model here is used to estimate ω_k and $a_{k,l}$ coefficients instead of predicting the signal at future. Indeed, because we are assuming that the complex coefficients are

WSS, thus the signal should be WSS otherwise the model is not held. WSS assumption is violated when there is a sudden short-time event in the signal such as a change in the average or the presence of an interference. By rearranging and putting variables in (3.36) to matrix and vectors, $\boldsymbol{x}_k[n]$ can be expressed as:

$$\boldsymbol{x}_k[n] = A_k[n]\boldsymbol{a}_k + \boldsymbol{e}_k[n], \tag{3.38}$$

$$A_k[n] = \begin{bmatrix} e^{j\omega_k n} & e^{j2\omega_k n} & \dots & e^{j\omega_k L_k n} \\ e^{j\omega_k (n-1)} & e^{j2\omega_k (n-1)} & \dots & e^{j\omega_k L_k (n-1)} \\ \vdots & \vdots & \dots & \vdots \\ e^{j\omega_k (n-M+1)} & e^{j2\omega_k (n-M+1)} & \dots & e^{j\omega_k L_k (n-M+1)} \end{bmatrix}$$

$$= \begin{bmatrix} 1 & 1 & \dots & 1 \\ e^{-j\omega_k} & e^{-j2\omega_k} & \dots & e^{-j\omega_k L_k} \\ \vdots & \vdots & \dots & \vdots \\ e^{-j\omega_k (M-1)} & e^{-j2\omega_k (M-1)} & \dots & e^{-j\omega_k L_k (M-1)} \end{bmatrix} \begin{bmatrix} e^{j\omega_k n} & & \mathbf{0} & \\ & e^{j2\omega_k n} & & \\ & & \ddots & \\ & \mathbf{0} & & e^{j\omega_k L_k n} \end{bmatrix} \tag{3.39}$$

$$:= Z_k D^n \tag{3.40}$$

$$:= Z_k[n] \tag{3.41}$$

(3.39) is derive by looking at each column of A_k so that the ith column is multiplied to $e^{j\omega_k in}$. We split the matrix A_k into two matrixes of one independent of time (Z_k) and the other is a diagonal matrix containing time information (D^n). Consider that Z_k is a **Vondermonde** matrix which is a full column rank matrix when $M \geq L_k$ (has more rows than columns). In (3.40), matrix D^n only depends on n and by plugging it to (3.38), either the matrix Z_k can be seen as a time varying matrix ((3.41)) or the vector $\boldsymbol{a}_k$:

$$\boldsymbol{x}_k[n] = Z_k[n]\boldsymbol{a}_k + \boldsymbol{e}_k[n] = Z_k\boldsymbol{a}_k[n] + \boldsymbol{e}_k[n] \tag{3.42}$$

$\boldsymbol{x}[n]$ is the summation of $\boldsymbol{x}_k[n]$ and it has an correlation matrix of R:

$$R = E(\boldsymbol{x}[n]\boldsymbol{x}^H[n]) = \sum_{k=1}^{K} Z_k P_k Z_k^H + Q \tag{3.43}$$

in which P_k is a diagonal matrix if $\boldsymbol{a}_k$ has uncorrelated coefficients for different l with diagonal elements of $A_{k,l}^2$. Q is the accumulation of the source noise powers. An estimation of the correlation matrix of R can be found by sample averaging: $\hat{R} = 1/G \sum_{N-1}^{m=M-1} (E(x[n]x^H[n])$

and $G = N - M + 1$ and N is the total number of samples over which the average is computed[7]. $\hat{R}$ is invertible when it is full rank and it happens when $M < N/2 + 1$ because $\hat{R}$ will be the summation of at least M rank 1 matrixes.

3.5.1 Optimum filter design

In order to find an estimate of $\boldsymbol{a}_k$ and ω_k, one can design a filter such that its output is the closest signal to the noiseless component in (3.36). The idea is similar to designing a matched filter, but here the output power of the filter is maximum when the true values of $\boldsymbol{a}_k, \omega_k$ are found. Assume, $\boldsymbol{h}_k[n] = [h_k[0], h_k[1], \cdots, h_k[M-1]]^H$ are the complex filter coefficients, then we want to minimize the numerical average error between the output filter samples and the noiseless signal component i.e.:

$$P = \min_{\boldsymbol{a}_k, \omega_k, \boldsymbol{h}_k} \frac{1}{G} \sum_{m=M-1}^{N-1} \left| \boldsymbol{y}_k[n] - \hat{\boldsymbol{y}}_k[n] \right|^2 \tag{3.44}$$

$$= \min_{\boldsymbol{a}_k, \omega_k, \boldsymbol{h}_k} \frac{1}{G} \sum_{m=M-1}^{N-1} \left| \boldsymbol{h}_k^H \boldsymbol{x}[n] - \boldsymbol{a}_k^T \boldsymbol{w}_k[n] \right|^2 \tag{3.45}$$

In (3.45), $\boldsymbol{w}_k[n] := diag(D^n)$. Consider that the objective in (3.45) is minimizing the average error between the filter output and the ideal noiseless periodic signal. Also, we have assumed that L_k is known while there are methods for estimating the model order (see [10]). The problem in (3.45) is quadric in both $\boldsymbol{a}_k$ and $\boldsymbol{k}_k$. In addition, it has a bounded optimum solution when $W_k := 1/G \sum_{m=M-1}^{N-1} \boldsymbol{w}_k[n] \boldsymbol{w}_k^H[n]$ is positive semi-definite. In fact, it is straightforward to show that W_k is positive semi-definite [8].

Assume that ω_k is known. By taking derivative of (3.45) with respect to $\boldsymbol{a}_k$, the optimum harmonic coefficients will be obtained as:

$$\hat{\boldsymbol{a}_k} = W_k^{-1} G_k \boldsymbol{h}_k \tag{3.46}$$

and $G_k := 1/G \sum_{m=M-1}^{N-1} \boldsymbol{w}_k[n] \boldsymbol{x}^H[n]$. By replacing (3.46) to (3.45) it will turn to a new problem for $\boldsymbol{h}_k$, which is quadratic and has a trivial solution of zero. Thus, a new condition on $\boldsymbol{h}_k$ will be added such that the filter impulse response has 1's on the harmonic frequencies

[7] Because is is assumed that $\hat{R}$ is stationary, then N should be long enough to have a good estimation of R. Practically, it should be at least 5 periods of the periodic component having the smallest fundamental frequency.

[8] If $U \in R^{n \times n}$ and $U = \boldsymbol{v}\boldsymbol{v}^H$, then $\forall \boldsymbol{x} \in R^n$, $\boldsymbol{x}^H U \boldsymbol{x} = \| \boldsymbol{v}^H \boldsymbol{x} \|^2 \geq 0$.

Algorithm 2 Finding $\hat{\boldsymbol{h}}_k$, $\hat{\boldsymbol{a}}_k$, $\hat{\omega}_k$

Set N,M,L `// based on prior knowledge about the signal`

cc = 1 `// counter`

for $\forall \omega_k \in \Omega$ **do**

  Compute: G_k, W_k, $\hat{Q}_k$

    Compute: $H_{mat}(cc,:) = \hat{\boldsymbol{h}}_k$ `// The matrix indexing syntax is the Matlab style. The right hand side is from equation (3.47).`

  $A_{mat}(cc,:) = \hat{\boldsymbol{a}}_k$ `// from equation (3.46)`

  $\hat{\boldsymbol{p}}_k(cc) = \boldsymbol{h}_k^H \hat{R} \boldsymbol{h}_k$

  cc = cc + 1

end

Find $\hat{i} =$ index of $max(\hat{\boldsymbol{p}}_k)$

$\hat{\boldsymbol{h}}_k = H_{mat}(\hat{i},:)$

$\hat{\boldsymbol{a}}_k = A_{mat}(\hat{i},:)$

$\hat{\omega}_k =$ i'th member of Ω

of $\omega_k l$ for $l = 1, \cdots, L_k$. After solving the new problem, optimum filter coefficients can be calculated by:

$$\hat{\boldsymbol{h}}_k = \hat{Q}_k^{-1}(Z_k^H \hat{Q}_k^{-1} Z_k)^{-1}\mathbf{1} \tag{3.47}$$

$\mathbf{1}$ is a column vector of all ones, and $\hat{Q}_k$ is the residual noise correlation matrix remained after estimating $\boldsymbol{a}_k$. In other words, $\hat{Q}_k := \hat{R} - G_k^H W_k^{-1} G_k$.

For estimating ω_k, a **brute-force** method is adopted by testing all candidate ω_k's so that the filter output power is maximized i.e.:

$$\hat{\omega}_k = \underset{\omega_k \in \Omega}{\text{argmax}}\ \boldsymbol{h}_k^H \hat{R} \boldsymbol{h}_k \tag{3.48}$$

and Ω is the set of all possible ω_k's. For instance, breathing rate is in $[0.1, 0.6]\,Hz$. One can search within this frequency range by a frequency resolution of Δf to obtain a profile for the filter output power versus all frequencies. In ideal, $\hat{\omega}_k$ is corresponding to the profile peak. In summary, the complete algorithm for finding the filter, harmonic coefficients, and fundamental frequency is shown in algorithm 2.

Residual noise power in successive signal component elimination

As we will see in the vital signs chapter, the breathing signal produces large interference on the heart band leading to a poor estimation of the heart rate. One suggestion might

be using (3.47) and (3.46) to construct a noise-free breathing signal, then subtract it from the signal to **enhance** the heart signal. This must be done with the noise and distortion considerations.

Suppose that the first component in (3.37), which is for breathing signal, is perfectly estimated with zero error, thus $y[n] = \boldsymbol{h}_1^H \boldsymbol{x}[n]$. Therefore, the difference $x[n] - y[n]$ is a new observation, which can be used for heat signal characterization by applying the same procedure in algorithm 2. So,

$$d[n] = x[n] - y[n] = \sum_{l=1}^{L_1} a_{1,l} e^{j\omega_1 ln} \sum_{l=1}^{L_2} a_{1,l} e^{j\omega_2 ln} + e_[n] - \boldsymbol{h}_1^H \boldsymbol{x}[n] \tag{3.49}$$

$$= \boldsymbol{w}_1^T \boldsymbol{a}_1 + \boldsymbol{w}_2^T \boldsymbol{a}_2 - \boldsymbol{h}_1^H Z_1 D_1^n \boldsymbol{a}_1 - \boldsymbol{h}_1^H Z_2 D_2^n \boldsymbol{a}_2 + e[n] - \boldsymbol{h}_1^H \boldsymbol{e}[n] \tag{3.50}$$

the third term in (3.50) will cancel the first term and after rearranging terms, the difference signal will be:

$$d[n] = (\boldsymbol{w}_2^T - \boldsymbol{h}_1^H Z_2 D_2^n)\boldsymbol{a}_2 + \tilde{\boldsymbol{h}}_1^H \boldsymbol{e}[n] \tag{3.51}$$

where $\tilde{\boldsymbol{h}}_1^H = [1 - h[0], h[1], h[2], \cdots, h[M-1]]^H$, in which all the entries are the same as $\boldsymbol{h}_1$ except the first one. So, the new noise power is:

$$\tilde{P}_n = \sigma_n^2 \parallel \tilde{\boldsymbol{h}}_1 \parallel^2 \tag{3.52}$$

Because there is no restriction on the $\parallel \boldsymbol{h}_1 \parallel$ during optimum filter design, so the noise power could be more when a component is subtracted from the original signal. Also note that the second term in (3.51) corrupts the heart signal.

3.5.2 Harmonic processing complexity

The complexity of algorithm 2 depends on the calculation of $\boldsymbol{w}_k$, W_k, $\hat{Q}_k$, $\hat{\boldsymbol{h}}_k$, $\hat{R}$, and $\boldsymbol{a}_k$. But, the complexity order has an upper-bound denoted by $\mathcal{O}$ [14][9]. The overall calculation of the mentioned variables is $\mathcal{O}(M^3)$ and M is defined as in algorithm 2. There is an iteration on all $\omega_k \in \Omega$ and if $|\Omega|$ is the cardinality of the candidate frequencies, then the total time complexity of the algorithm is $\mathcal{O}(|\Omega|M^3)$. For instance, if breathing frequency is divided in 100 segments with $M = 200$ when the sampling frequency is 20 Hz, then $800,000,000$ operations are required to get the parameters.

[9] See chapter 3.

3.5.3 Real phase to complex phase

The phase signal in (3.19) is a real signal but the model in (3.36) is complex. In fact, every real signal can be converted to an analytical downsampled complex signal [7]. The complex signal has the same real value as the original real signal. There is another method for making a complex signal out of a real signal such that they have the same real parts. The idea comes from the fact the one can set negative frequencies of the real signal to zero without loss of information. In fact, the real data has a symmetric frequency content so that having half of the frequencies is enough for representing the signal. To set the negative frequencies of a real signal to zero and maintaining the same real parts, **Hilbert** transform of the signal is required as follows:

$$y[n] = \frac{1}{\sqrt{2}}(x[n] + j\hat{x}[n]) \tag{3.53}$$

in which y is the complex signal and $\hat{x}$ is the Hilbert transform of x. But y in 3.53 is not analytical while its counterpart for the continuous signals is [7]. To have an analytical signal, the real and imaginary parts of y should be orthogonal, which leads to the following conversion written in Matlab syntax.

Listing 3.1: Matlab code for real to complex conversion

```
N=length(x); X=fft(x,N);
y=(1/2) *ifft ( [X(1)+X(N/2+1) ;2+X(2:N/2)] , N/2 );  % By downsampling
    factor of 2, the two ends of the spectrum will be overlapped.
```

3.6 Summary

In this chapter, we started the discussion with fundamental principles of FMCW radar. The mathematical derivation for obtaining target's range, velocity, and vibration frequency was presented. Based on the parameters defined in Table 3.1, the final equations for estimating each parameter are listed in Table 3.1.

In practice, before phase analysis, the DC of the received complex beat signal should be removed. After removing DC, the phase is calculated and unwrapped based on algorithm 1. Furthermore, the real phase should be converted to an analytical complex signal prior to fundamental frequency estimation. The algorithm 2 can be used to estimate the vibration frequencies as well as harmonic coefficients.

Table 3.1: FCMW radar range and velocity estimations and their min/max detectable bounds

Parameter	**Range**	**Radial velocity**	**Vibration frequency**
Estimation	$\hat{R}_0 = \frac{f_b c}{2K}$	$\hat{v} = \frac{\lambda_{max}}{2} \text{argmax}_f(\lvert\tilde{Y}(f)\rvert)$[a]	$\hat{f}_v = \text{argmax}_k \left(\lvert\hat{p}_k\rvert\right)$[b]
Max	$\frac{c f_{b,max}}{4K}$	$\frac{\lambda_{max}}{4T_c}$	$\frac{1}{2T_c}$
Min	$\frac{c f_{b,max}}{2NK}$	$\frac{\lambda_{max}}{2MT_c}$	_ [c]

[a] $\tilde{Y}(f)$ is the FFT of $\tilde{y}[n]$ in 3.18.

[b] $\hat{p}_k$ is output power of the optimum filter for ω_k.

[c] the minimum can be anything.

In the following chapters, we will address the radar performance by designing different tests. Then, the radar results for vital signs detection will be presented.

Chapter 4

System verification with experiments and simulations

In this chapter, we will investigate the radar performance in terms of range, radial displacement, and vibration detections. To that end, we designed three different tests as follows:

- **Antenna chamber tests**: The radar accuracy in the range, radial displacement, and vibration detections are examined in a clutter-free environment i.e. an antenna chamber.
- **Stationary tests**: The phase received from a stationary target is investigated where it has a linear trend. The source of the phase slope is identified and it has been shown it does not deteriorate the vital signs detection.
- **Pendulum tests**: The performance of the system is evaluated for vibration frequency estimation by employing the algorithm 2. In these experiments, we designed a pendulum system with which we will investigate the problem of DC compensation, phase harmonics, and frequency estimator performance before discussing the vital signs application in the next chapter. The pendulum system allows us to modulate the phase synthetically similar to what is done by the cardio-respiration activities. In addition, the subtleties during radar analysis, as mentioned in the previous chapter theoretically, are investigated practically.

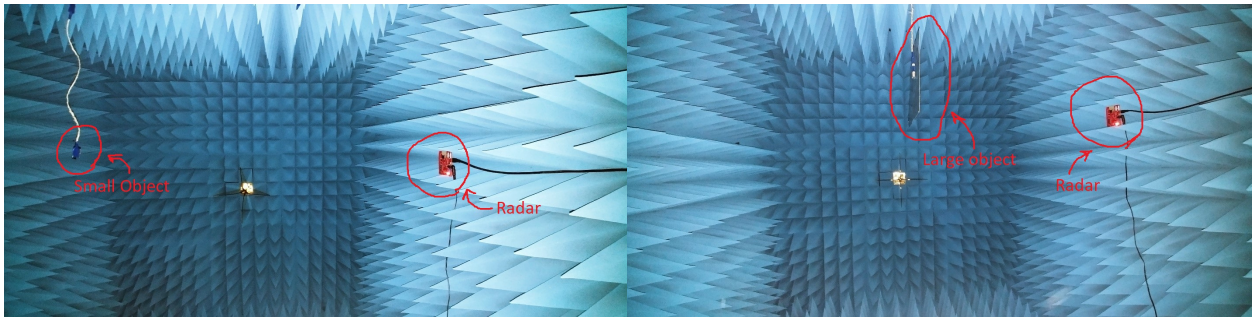

(a) (b)

Figure 4.1: Antenna chamber

Table 4.1: Radar configuration for chamber tests

Parameter	T_c	**Frame rate**	**Chirp slope**	$f_{b,max}$	**N**[a]	**M**[b]
Values	57 μs	20 fps	70 $MHz/\mu s$	2 MHz	128	256

[a] Range FFT size

[b] Second FFT size, which is either for velocity or vibration maps

4.1 Antenna chamber tests

The radar was placed in an antenna chamber which is, an ideal, a clutter-free environment allowing to examine the reflections from the desired targets. The targets we chose are two rectangular aluminium plates. One of them is $2 \times 2\,cm$ and the other is $20 \times 30\,cm$. The Radar configuration parameters are given in Table 4.1. The min/max values of each variable corresponding to the values in Table 4.1 are given in Table 4.2. Since the minimum resolvable distance difference is 3.76 cm, the small plate should only be seen in a single range bin, in contrast, the big plate fills more than three range bins. In Figure 4.1, the radar and the plate locations and their alignment are shown.

An FFT of size N is applied on each received chirp samples. Then the DC compensation is applied. The *range-velocity* map is obtained by taking the second FFT over the DC compensated range bins across M chirps. For *range bin phase spectrogram* map, instead of taking FFF of the complex samples, the short-time Fourier transform (STFT) is taken over unwrapped phase of the target range bin.

In figure 4.2a, the small plate is located at 1.46 m and occupying about 3 range bins. Ideally, the target should be seen in a single range bin, as mentioned before, but due to

Table 4.2: Min/Max value of different parameters

Parameter	Range	Velocity	Vibration
Max	8.57 m	19.5 mm/s	10 Hz
Min (resolution)	3.76 cm	0.1522 mm/s	0.0781 Hz[a]

[a] FFT is used to calculate the vibration thus the minimum is the FFT resolution.

phase noise of the FMCW generator, the beat signal does not have a sharp peak only at f_b (see 3.4). The spectrum widening is one effect of the phase noise reducing the range accuracy. In fact, $\exp(j\phi_n[m])$ in 3.19 is multiplied to the phase noise-free part of $\tilde{y}[m]$ in (3.18), which spreads the beat signal spectrum. Also note that there are reflections at other ranges meaning that the chamber is not perfectly absorbing the wave at this frequency. Figure 4.2b shows that everything, including the target, is perfectly still and this is consistent with Figure 4.2c as well.

In comparison to Figure 4.2a, in Figure 4.3a the large plate range bin is wider as expected and the plate is vibrating around its hanger in Figure 4.3b. This is not a radial velocity as the *range-velocity* map does not have a single peak implying that there is periodic movement. Figure 4.3c also indicates that the plate was moving with an almost constant vibration frequency of 0.7813 Hz during the entire recording.

We intentionally tapped the plate to oscillate. Different maps for this case are illustrated in figure 4.4. First of all, the *range-velocity* map is full of harmonics generated due to the high magnitude of vibrations. Secondly, the *phase spectrogram* shows a smooth reduction of the vibration harmonics over time. The fundamental frequency of the vibration is 0.7813 Hz. This is almost the same vibration fundamental frequency as in figure 4.3, but with different magnitude. In addition, figure 4.5 depicts the time variation of the range bin unwrapped phase together with the wrapped phase. Initially, the phase is not unwrapped correctly because of sparse sampling of the phase. There is no upsampling in the processing but it can be used to uncover the phase even for the beginning moments.

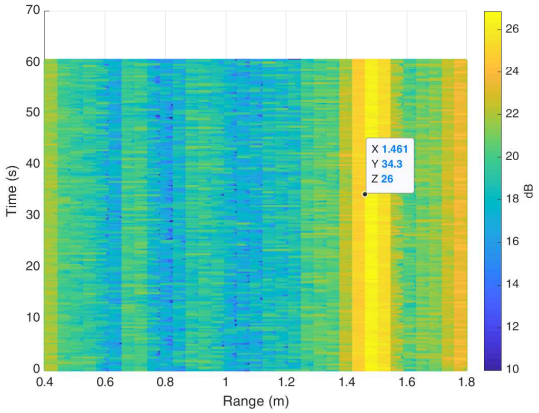

(a) Range-slow time map

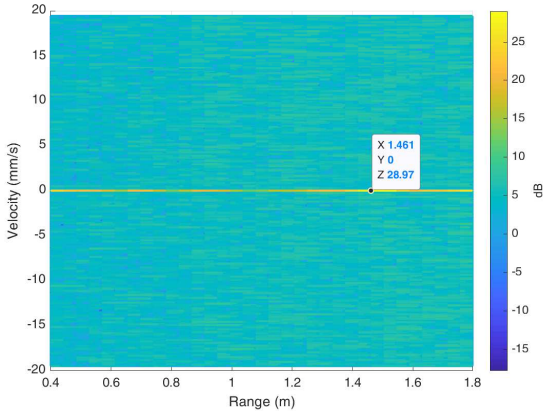

(b) Range-velocity map

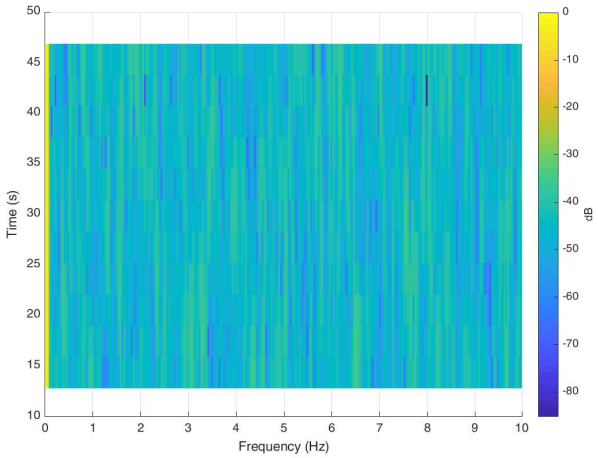

(c) Range bin phase spectrogram

Figure 4.2: Different maps for the small still plate

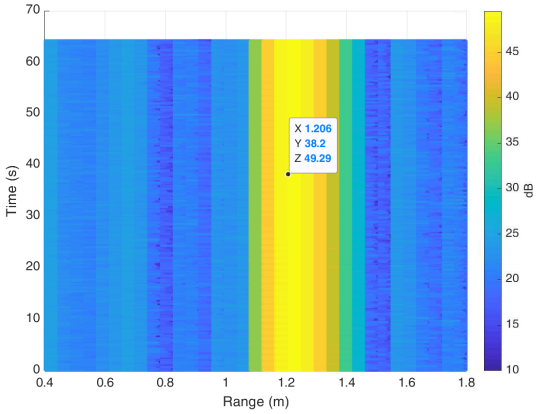

(a) Range-slow time map

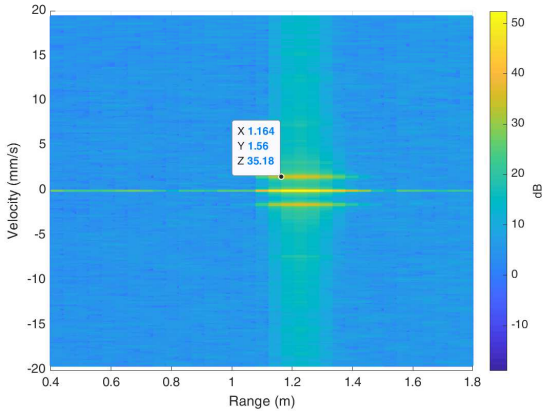

(b) Range-velocity map

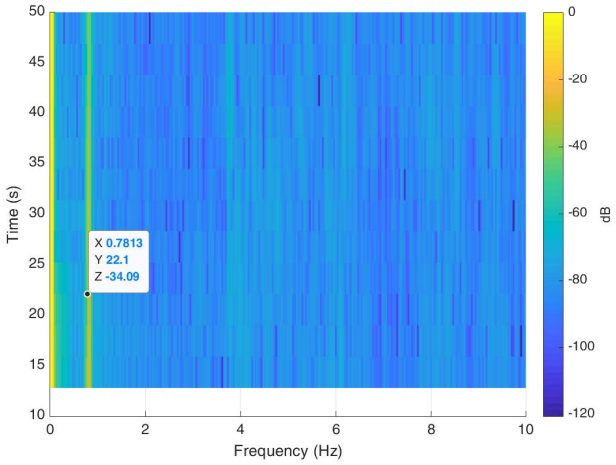

(c) Range bin phase spectrogram

Figure 4.3: Different maps for the large still plate

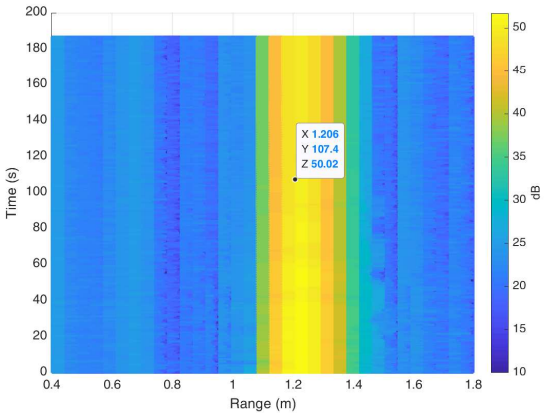

(a) Range-slow time map

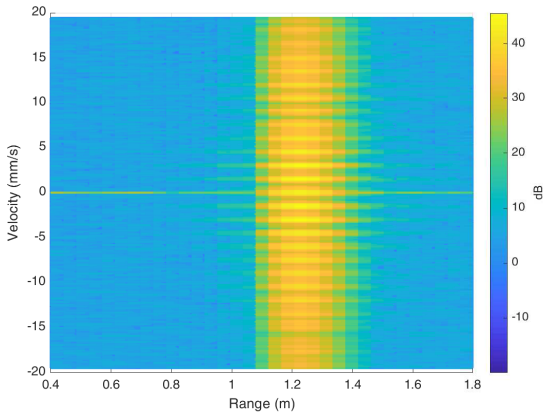

(b) Range-velocity map

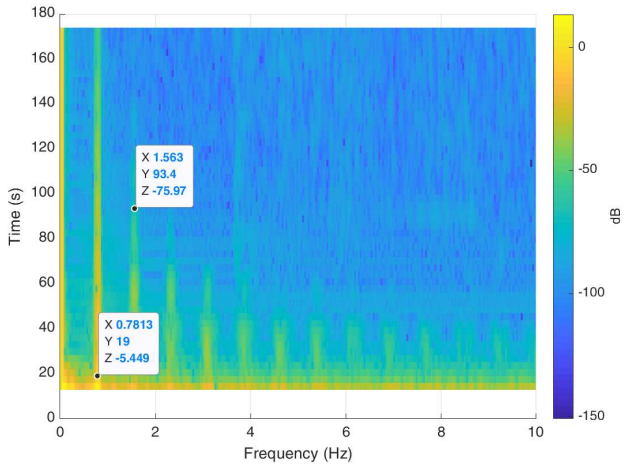

(c) Range bin phase spectrogram

Figure 4.4: Different maps for the large high vibrating plate

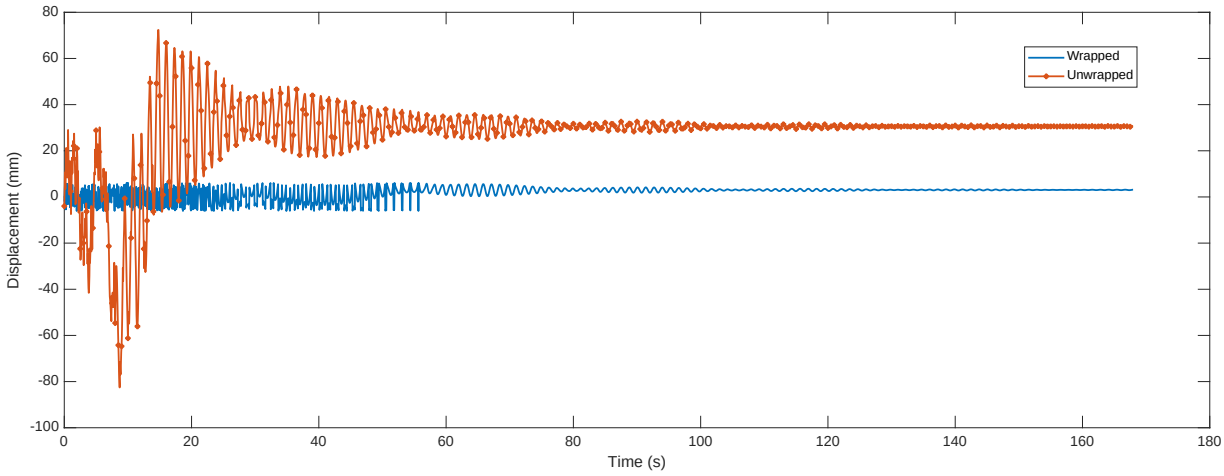

Figure 4.5: Phase variation of the oscillating plate

4.2 Stationary tests

In a long-time run of the radar, the phase exhibits a linear trend, which could result in a high DC in the phase. The trend does not depend on the range of the object and it is indeterministic. The small slope in the phase means that there is a residual frequency in the received complex signal that might be due to residual delay between Tx and Rx. The residual delay might be either because of delays in the circuit path or non-linearities in the FMCW signal generation. There is no nonlinearity in the FMCW output; therefore, the reason for the linear phase trend is due to group delay variation of the PA and LNA over temperature. Also, as the PA heats up, the group delay varies so that the phase slope is varying from one experiment to another.

To show the repeatability of the hypothesis, the tests were run for different objects at different ranges. The plates were free to have micro movements as they were hung up to the chamber ceiling. The radar is configured with parameters in Table 4.1. For example, figure 4.6 shows a target's range phase, which was placed at 1.26 m. There is no need for phase unwrapping as the phase changes in a few radians. The slope in this experiment is about 2 $\mu m/s$. There are other peaks in the phase spectrum at 2.148 Hz and 8.438 Hz. The phase magnitude for these peaks is within micro meter, for instance, a peak at -50 dB is equivalent to 3.2 μm. It is important to notice that there is a noise floor for the phase, which is -70 dB/Hz.

For vital signs detection, since the BR is as slow as 0.1 Hz, the phase DC should be removed for BR estimation.

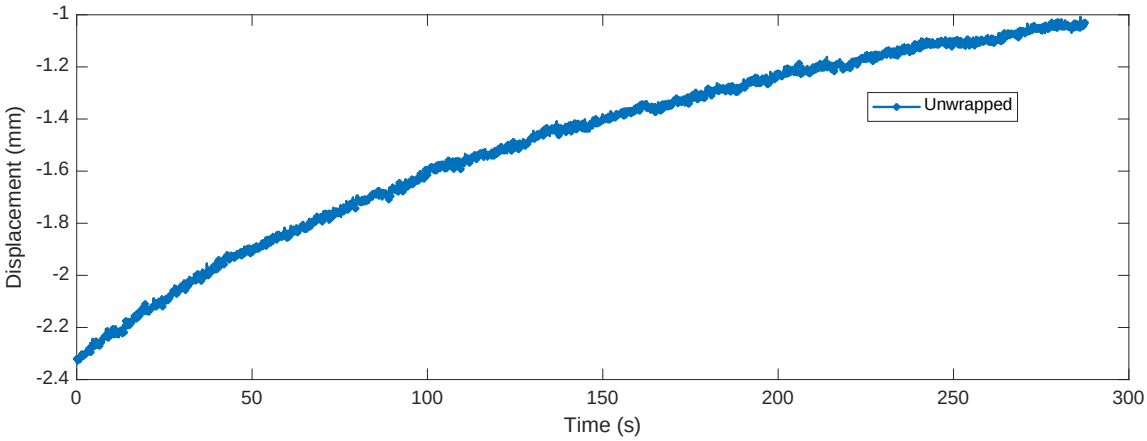

(a) Phase time trace

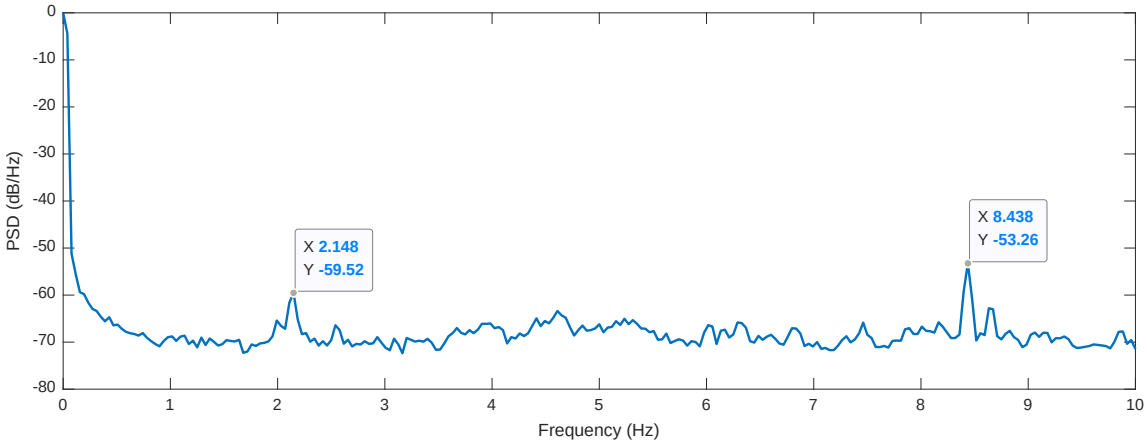

(b) Phase spectrum

Figure 4.6: Linear phase trend

4.3 Pendulum tests

To understand the theoretical analysis done in the previous chapter, we designed a series of experiments with a system containing two pendulums. The system has two pendulums connected to two servo motors with which we can control the swing speed as well as the swing angle. Figure 4.7 shows the base on which the servo motors and the wooden pendulum arms are mounted. Two raspberrypi's are used to generate pulse width modulation (PWM) signal for servo motors to adjust the angle of the arms and their swing speed. The end of each pendulum is covered with a metallic sheet to have higher reflections than the other parts. The radar is placed at different distances to the base centre. In fact, the two pendulums are at the same distance to the radar.

The servo motors could not move the arms smoothly. Particularly, the arms were moved in a step-wise manner by the motors resulting in step-wise phase modulation. The problem were more sever when the swing speed was very low or the swing angle was very wide. Indeed, at the two ends of swing period, when the swing direction changes, the arms were shaking resulted in a high order harmonics. The two issues where controlled by setting appropriate values for the swing angle and the speed. Therefore, we could not expect a fully-controlled smooth swinging, which is enough to model the chest wall movement.

The radar is tested by the pendulum system either when one or both pendulums were moving. The later will be a reference for the vital signs detection in which we have two independent vibrating objects at the same range.

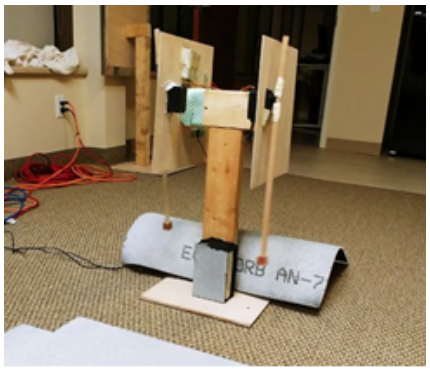

Figure 4.7: Pendulum system

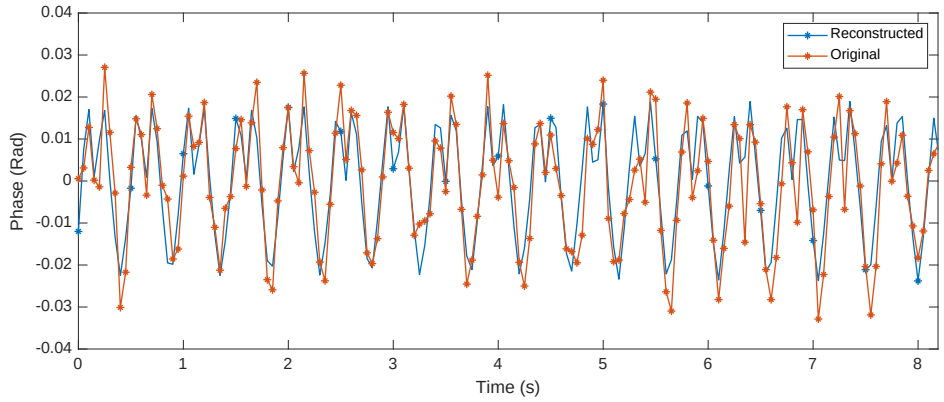

Figure 4.8: Phase time trace for the pendulum at 2.5 m.

4.3.1 One-pendulum tests

In this series of experiments, we will use a single pendulum to modulate the wave echo. We placed the base at the range from 30 cm to 2.5 m when the pendulum was swinging with almost **2.1 Hz**. The radar configuration is the same as Table 4.1 with the valid values in Table 4.2 except that the frame rate is 80 fps. Thus, the vibration rate can be at most 40 Hz. This is much higher than what we need, therefore, the signal is decimated before passing it to the fundamental frequency estimator to have a sampling of 20 Hz.

The original waveform in figure 4.8 is extracted after phase unwrapping process (see algorithm 1) and converting the real phase to the complex phase procedure described in section 3.5.3. The pendulum was at 2.5 m away. The reconstructed waveform is obtained by using the estimated complex coefficients in the model (3.36) with the triple (N,M,L)=(1024,100,4) (in samples). The estimated waveform is very close to the original proving the validity of the estimation even for the far vibrating objects.

As mentioned before, the pendulum was moving step-wisely with a jitter at end of each swing period. As a result, the modulated phase is not purely sinusoidal, which is plotted in Figure 4.8. Also, in Figure 4.9, the phase spectrogram is plotted for the two ranges. The harmonics of the phase are pretty obvious for the pendulum at 30 cm, however, they are less visible at 2.5 m. In fact, the phase noise decorrelation effect at higher ranges makes the received phase noisier. As a result, the higher order harmonics buried under the phase noise power in figure 4.9b.

After running the pendulum for a long time at each range, the accuracy of the fundamental frequency estimator in terms of number of probability of error versus range is

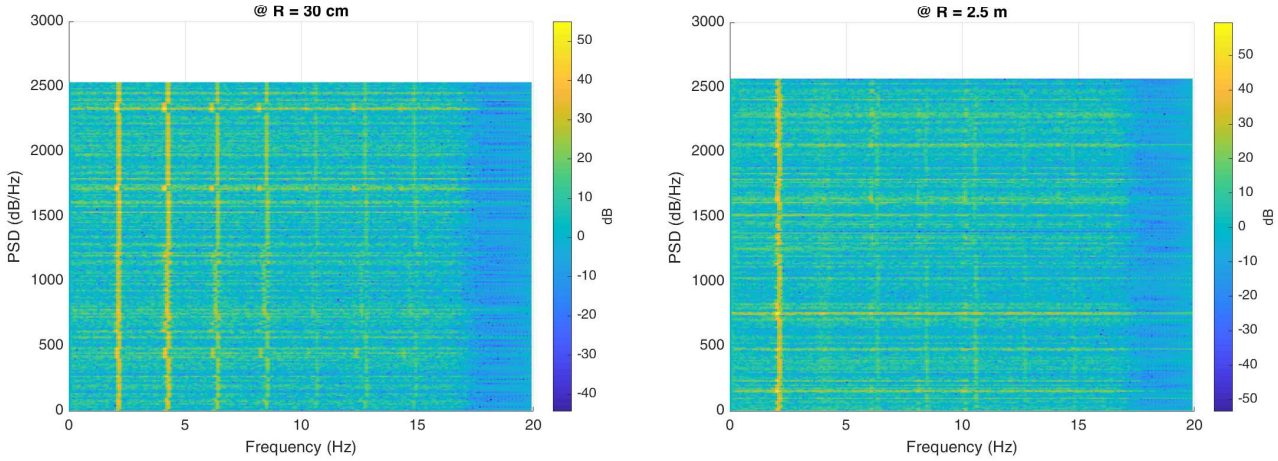

(a) (b)

Figure 4.9: Phase spectrograms of a pendulum with vibration of 2.1 Hz at 30 cm and 2.5 m.

obtained in Figure 4.10 . The prominent fact is that as the range increases the phase quality degrades due to the effect of phase noise uncorrelation (see (3.7)). Furthermore, the thermal noise power is independent of the target range because the received power of the far target is very small due high attenuation, the SNR is lower. Though, the phase noise uncorrelation and SNR reduction deteriorate the phase quality.

DC offset cancellation for one pendulum

The DC in the received complex signal has three origins as mentioned before. In practice, the DC is removed from the received beat signal due to antenna coupling and RF cross-talk. Furthermore, the stationary clutter produces a DC which will appear in the recived range bin. The pendulum system does not have large RCS to shift the complex signal constellation from the origin[1]. However, when a big object like a chair is placed next to the pendulum, the constellation will shift according to the RCS of the chair. For the illustration, the pendulum and the chair were placed at 1.5 m. The radar configuration

[1]In fact, the non-vibrating parts of the pendulums' base can be seen as a stationary clutter. More specifically, the received range bin is a superposition of the two signals, one coming from the vibrating target and the other one from the base body. Hence, if the stationary parts of the base have large RCS, it means that that there will be a high DC in the received range bin.

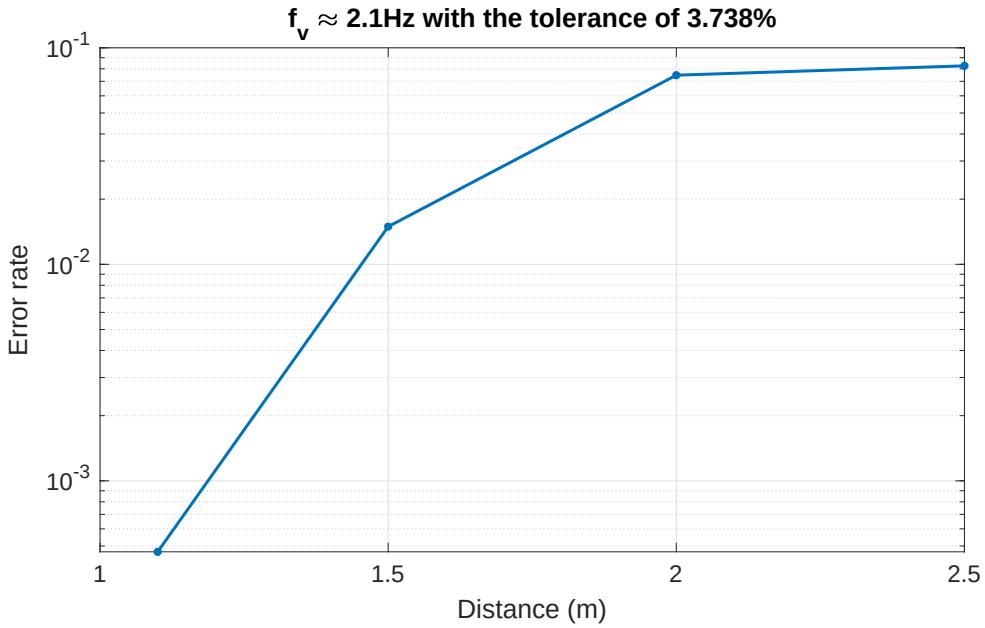

Figure 4.10: f_0 estimation error rate for a single pendulum.

is the same as Table 4.1 except the frame rate is 200 fps. The pendulum frequency was set to 6.5 Hz such that the phase was modulated with less harmonics. In Figure 4.11, the received complex signal trajectory is depicted where the center of the phase modulation is shifted back to the origin by estimating the center (and the radius) using (3.27). The phase variation is shown in Figure 4.12 before and after DC compensation. Visually, the DC removed signal has lower distortion.

The phase spectrograms in Figure 4.13 prove that the phase harmonics reduced. More specifically, the power spectral density (PSD) of both signals are demonstrated in Figure 4.14. As the marker indicates, the second harmonic is reduced by 12 dB using DC compensation.

This should be noted that the DC compensation is required for the phase analysis if we know that there are stationary clutters at the range of interest, otherwise removing it does not improve the phase quality and also it distorts the phase.

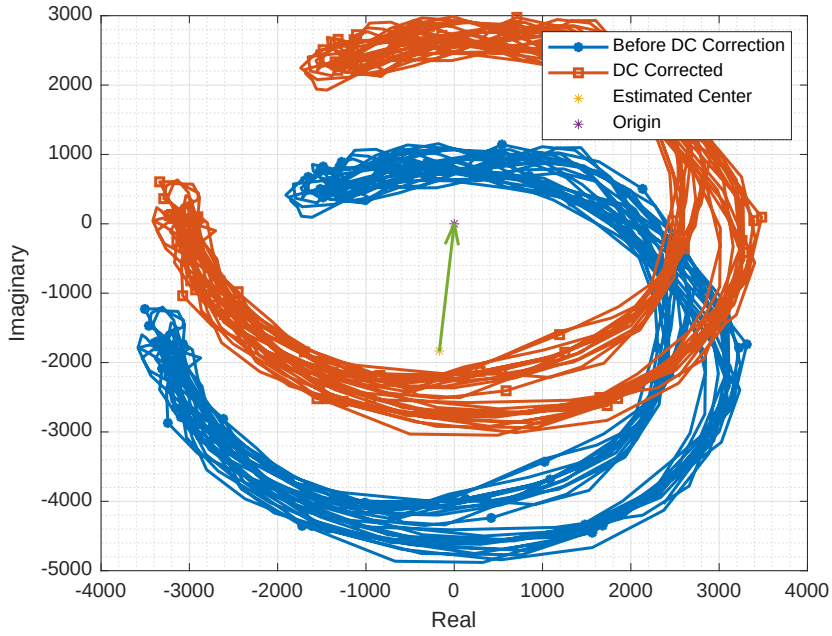

Figure 4.11: Signal constellation with a shifted origin

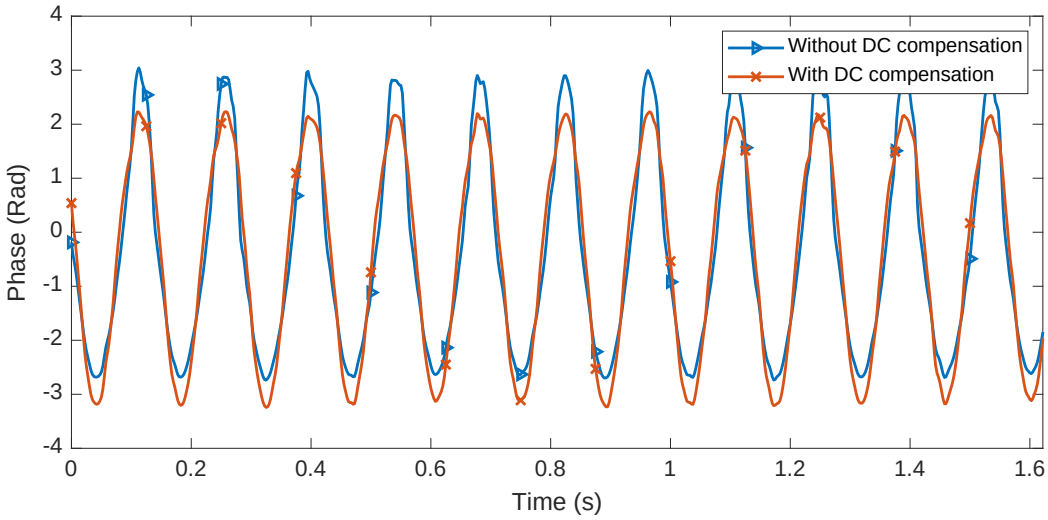

Figure 4.12: Phase modulation with a single pendulum before and after DC cancellation

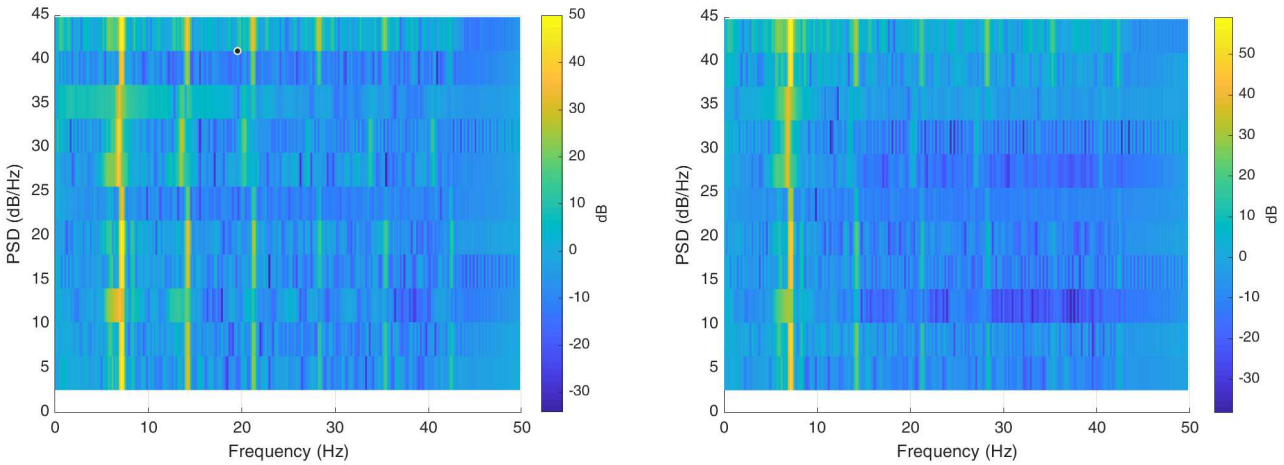

(a) With DC (b) Without DC

Figure 4.13: Phase spectrograms before and after DC offset cancellation

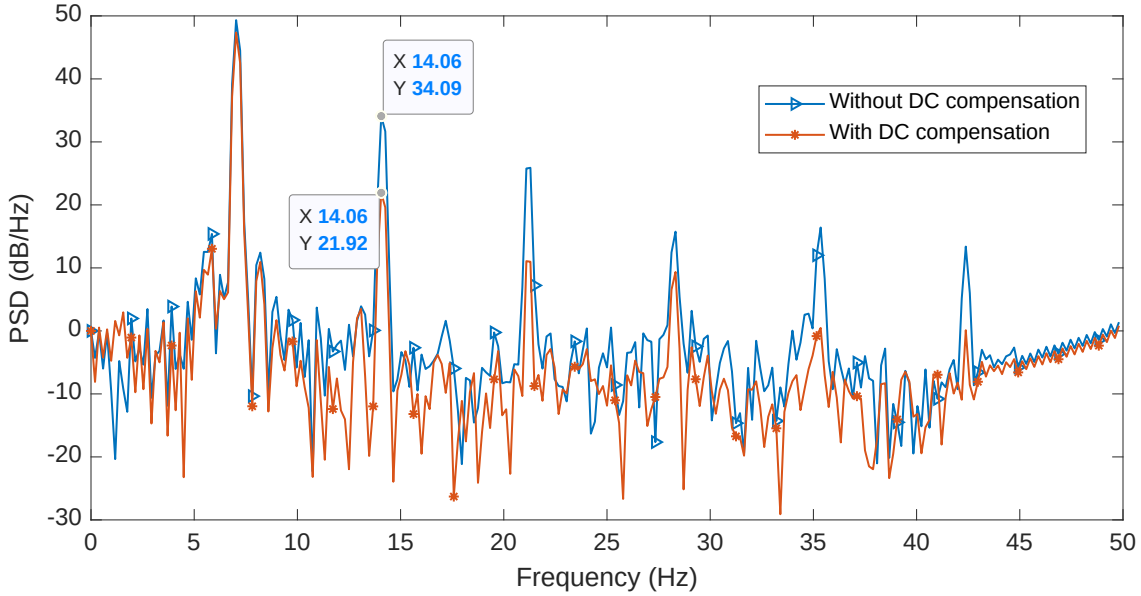

Figure 4.14: PSD of the phase signal before and after DC compensation

4.3.2 Two-pendulum tests

For the vital signs' application, the chest wall moves by the respiration and heart beats. To emulate the behaviour, we used the two-pendulum system as a reference for the radar accuracy in detecting two independent vibrating targets at the same range[2]. The magnitude respiration motion is about ten times greater than the heartbeats (see A_h, A_b in 3.22). In addition, the frequency of BR is about 6 times less than HR. Considering these ratios, the frequency for the two pendulums were set to **2.04 Hz** and **6.5 Hz**, respectively. Let us call the pendulum with lower frequency p1, and the other p2. The amplitude of vibration for p1 to p2 were set to 10.

There is no need for DC compensation. The radar parameters are the same as Table 4.1 except the frame rate is 200 Hz. The higher the frame is, the better the phase is unwrapped. The received signal is down-sampled to the sampling of 50 Hz after phase unwrapping. Furthermore, the fundamental frequency estimation parameters were set to (N,M,L)=(10 seconds, 4 seconds, 4).

The pendulums were placed at the ranges from 85 cm to 2.5 m. The two figures in 4.15 show the single-side band phase spectrograms obtained at two different ranges. The harmonics of p1 up to 4th order, about 8 Hz, can be seen in 4.15a. In contrast, the harmonics of p2 decay faster such that they cannot be found higher than the second order. Also, there are intermodulation components between p1 and p2 up to the third order. For instance, there is a peak around 15 Hz, which is $2f_1 + f_0$ where f_1 and f_0 correspond to the frequency of p1 and p2, respectively. The noise level in the phase domain at 2.5 m for the two pendulums is higher than the single pendulum (see Figures 4.9b and 4.15b). This stems from the appearance of the intermodulation terms in the two-pendulum system.

The frequency estimator performance versus different ranges is depicted in Figure 4.16. For the comparison, the error rate for the single-pendulum system is also included in the figure. To obtain each point in the figure, it was required to run the system for more than 40 minutes in order to measure the error rate above 0.02. The important fact is that the error rate for the p2 is higher, which is justifiable for a phase modulation with 20 dB less power than p1[3]. Also note that the lower bound for the system performance is the single-pendulum system. Specially, with this radar, the error rate of the vibration

[2]From the biological point of view, the respiration and heart rates depend on each other such that an increase in the BR will also increase HR. However, for the purpose of signal processing, we assume that they are independent.

[3]The power of the phase modulation for p2 is 20 dB less than p1 since its magnitude is 10 times less than p1.

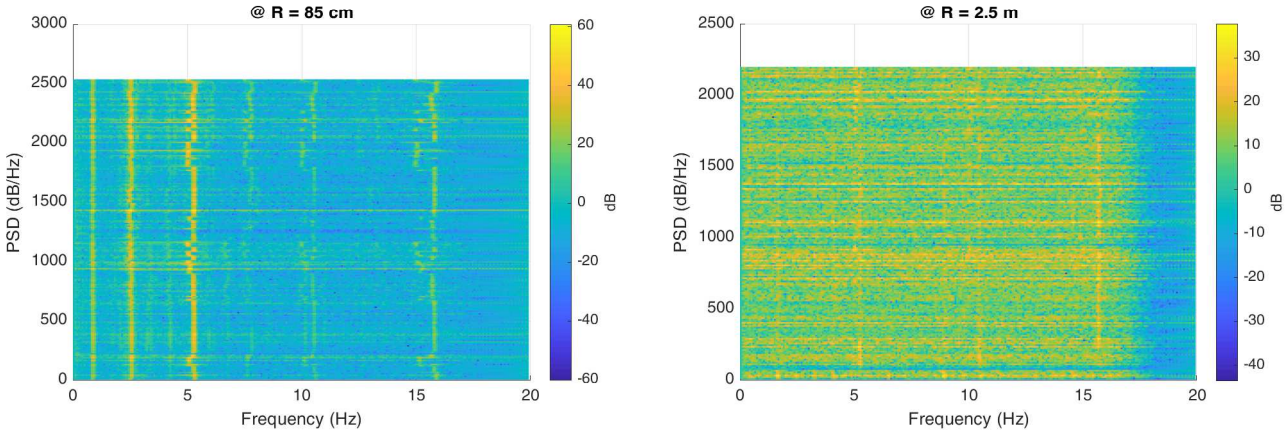

(a) (b)

Figure 4.15: Phase spectrograms of the two pendulums at 85 cm and 2.5 m

frequency estimations in the two-pendulum system (as well as vital signs) is higher than the single pendulum system by using the optimum filter.

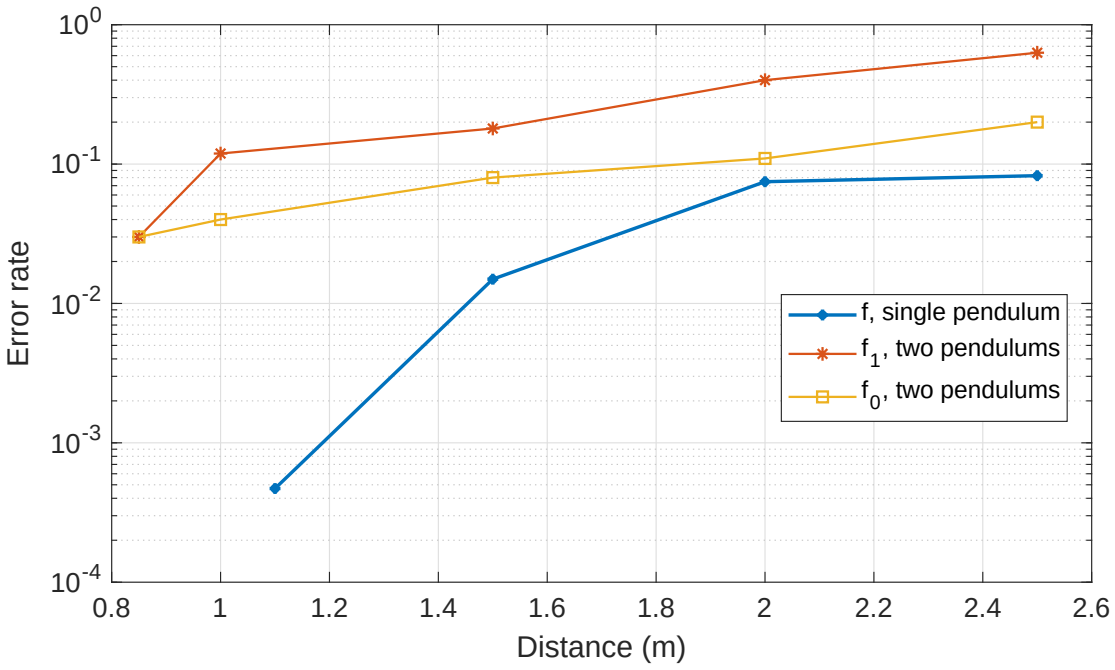

Figure 4.16: Frequency estimator error rate for two-pendulum and single-pendulum experiments at different ranges: f_0, f_1 are for p1 and p2, respectively.

4.4 Matlab simulations

The Simulink environment of Matlab leverages the same toolbox functions and it provides pipeline processing [4]. To be more clear, it does not run the blocks in different threads like a multi-thread program, but it can use GPU or the CPU itself to parallelize the processing whenever it is possible. The parallel processing basically depends on the intelligence of Matlab to choose which parts can be run on different CPU cores separately. In general, Simulink provides a higher simulation speed and has rich and powerful tools for visualizing the signal properties, which help to understand, identify, and debug the program.

As a matter of fact, we used Simulink for analyzing the system under practical circumstances, which is based on the most realistic assumptions that has been used so far. We used *phased array* and *antenna* toolboxes together to model an FMCW radar. The model incorporates all the transceiver chain from the generation of the FMCW signal, transmit hardware, Tx/Rx antennas, the channel, objects, down to the signal processing at the receiver end. The first page of the designed Simulink model is illustrated in Figure 4.17. The FMCW signal is generating by a ready block from the *phased array* toolbox. The signal goes to a phased noise block, which adds a phase noise to the generator. Next, the signal is fed into an antenna array, which propagates the equivalent fields in the space. The field is attenuated by considering the free space channel model and it is reflected by three scatterers. The scatterers are placed at the same distance on purpose. Two of them model the vibrations of the two vibrating objects while the third one models the stationary clutter. After the field bounces off the objects, it is collected by the receiver array, which is at the same location as the transmitter. In the wave propagation, the wave polarization is considered in order to count the effect of the polarization change. Then, the thermal noise will be added and the mixture is correlated with the transmit signal to get the beat signal. The beat signal has a very high sampling rate but it has a low IF frequency. Hence, it is downconverted to 2 MHz sampling rate[5]. We denoted this process as the ADC block in Figure 4.17. After ADC, the signal is delivered to the signal processing block, which performs chirp collection, phase unwrapping, and fundamental frequency estimation.

Figure 4.18 shows the schematic of the radar and targets' platform positions. The propagation model is based on the *ray tracing* model. The model gets the propagation direction from the transmitter to the targets and it applies the antenna gain and phase on the signal. The targets can have a scattering matrix, which can be a time varying property.

[4] different from parallel processing

[5] Note that the same baseband sampling rate as $f_{b,max}$ in table 4.1. Also, the downsampling factor is 50, which has to be carried out by multi-chain downconverter to avoid of having long filters. Actually this is achieved by using 3 stages of downsampling by the factors of 5,5,2, respectively.

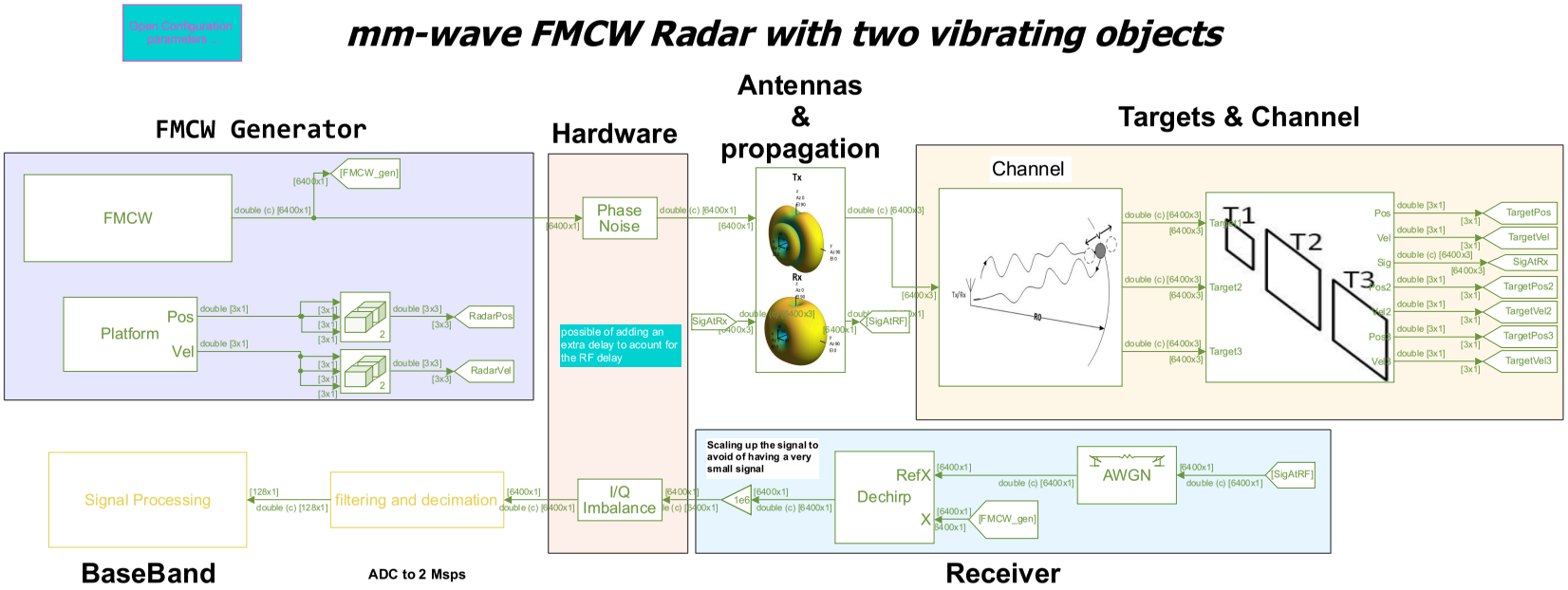

Figure 4.17: Matlab Simulink main page

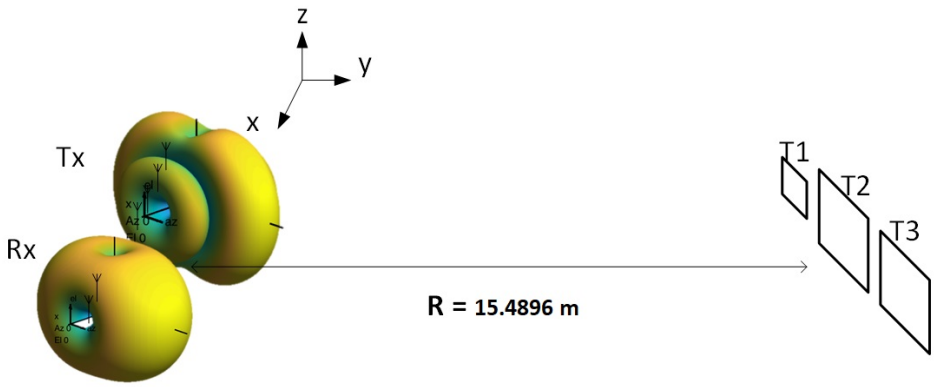

Figure 4.18: The radar and the targets' positions in the simulation

Without loss of generality, we assumed that they are constant. Although they are fixed, the mean RCS value of each target is different. The first target, denoted as T1 in the figure 4.18, is aimed for modelling the lung cavity for the respiration. Particularly, the second target (T2) has separate RCS, vibration magnitude and frequency to demonstrate the heart activity. The last target (T3) will help to give us insight about the effect of a stationary clutter on the phase quality.

We chose a 4 by 2 Tx/Rx arrays in the simulations. They are uniform linear array (ULA)s with dipole antenna elements and with half-wavelength spacing. Their patterns are shown in the schematic of 4.18. They were designed by the ready models in the *antenna* toolbox of Matlab. There is no restriction of using a custom antenna module by passing required parameters to Matlab antenna system object. The object can be replaced with the one that is used here and it will carry out all the necessary processing for converting a signal to a propagating field.

The actual radar system has a sweeping bandwidth of 4 GHz at 77 GHz. The simulation for that sweeping bandwidth requires to generate a signal with a sampling rate of 4 Gsps. In fact, the number of samples per $20\mu s$ chirp will be 80,000 samples. As a result, the size of the vectors and the processing time will be increased to an amount with which the simulation will not be made in a reasonable order of time. Thus, for the purpose of the simulation and without loss of generality, the sweeping bandwidth was set to 100 MHz by the chirp slope of 1.5625 $MHz/\mu s$ and the duration of 64 μs. The order of the valid range, velocity, and the vibration frequencies changed to values in Table 4.4. Also Table 4.3 summarizes the simulation configuration's parameters. The magnitude of the first and the second vibrating object are set with a ratio of 10 in order to mimic the situation between

the breathing and the heart waveform. Also, their frequencies have a ratio of 6 like the ratio between the HR to BR. The first target, v1, has the frequency of 24 Hz while the second one has the frequency of 105 Hz. In the entire simulation, the DC compensation is ignored due to absence of any stationary clutter. The phase noise is modelled by using a ready Matlab block from the communications toolbox. We set the noise level for the frequency shifts of $[500\ KHz,\ 1\ MHz]$ to $[x,\ -91]\ dBc$. The first phase noise level is varying in different simulations and we mentioned that on each simulation (see Figure 4.19). The second phase noise level is equal to the TI radar phase noise reported in Table 2.1. 500 KHz frequency shift from the carrier means that the target is at 47.9667 m away from the radar. Accordingly, 1 MHz shift means that the target is at 95.9336 m. In mm-wave frequencies the wave is attenuated by a factor of 10^{-13}, but for the simulation purpose, we added the thermal noise by a controlled SNR to be able to test for different SNRs. Otherwise, in practice, the receiver could not deliver the signal with a high SNR of 10 dB at these ranges.

The SNR is set such that the desired range experiences that SNR value. Therefore, the noise power level is computed by having the power of the echo signal and considering the target distance, antenna gains, and the free-space loss as well as the number of range FFT bins. The later is required to have the effective SNR in the range bin as they are reported in the results. The number of range FFT bins is 128 (see Table 4.3), so the noise power is multiplied to 128. This factor causes the effective desired SNR in the range bin bandwidth, which is a 128th portion of the baseband bandwidth. In practice, each range bin can have $10log_{10}128 = 21.072\ dB$ higher SNR with respect to the total baseband bandwidth. For instance, if we set SNR = 10 dB, then the actual SNR for the received beat signal can be -11.0720 dB.

The spectrum of the phase without applying DC compensation for two SNRs are shown in Figures 4.20 and 4.21. A comparison of the two figures reveals that the noise floor of the phase spectrum will be increased by reducing the SNR. This fact is analytically expressed in the equation of (3.35). The total harmonic distortion (THD) analysis of up to 6 order harmonics of the first vibrating object shows almost 5 dB THD increment in the phase domain, which is in agreement of the phase error variance in (3.35). The constellation points of the complex signal are shown in Figure 4.22. The uncertainty in the trajectory is increased by reducing the SNR. In addition, there is a DC offset around which the constellation points cloud is formed. This DC value is due to the phase modulation of the vibrating objects [43] and it does not distort the phase. The time domain of the phase for two values of the phase noise level 1 are plotted in figure 4.23. The phase variance is increased as a consequence of the SNR increment.

Indeed, the simulink model was run for a long time to obtain the frequency estimator

Table 4.3: Radar configuration for the Simulink model

Parameters	**Value**	**Description**
T_s	64 μs	
$T_r = 4T_s$	256 μs	Collecting the chirps every 4 chirps
Chirp slope	1.5625 $MHz/\mu s$	
Sweeping BW	100 MHz	
$f_{b,max}$	2 MHz	
λ_{max}	3.9 mm	
N	128	Range FFT size
NDop	128	Vibration FFT size which is equivalent to 32.76 ms.
$R_0,\ R_1,\ R_2$	14.9896 m	Equivalent to the range bin index of 11.
$A_{v1},\ A_{v2}$	0.4, 0.04 mm	Magnitudes of the first and the second vibrating object
$f_{v1},\ f_{v2}$	24, 105 Hz	Keeping the ratio of 6 between the two vibrating objects' frequency
L	4	System model order for f_0 estimation
M	81	The f_0 estimation parameter
N_{f0}	203	The f_0 estimation parameter

Table 4.4: Radar parameter detection valid ranges for the Simulink model

parameters	**Range** (m)	**Velocity**	**Vibration frequency**
Max	95.93	3.8 (m/s)	1.953 KHz
Min	1.499	5.94 (cm/s)	30.51 Hz

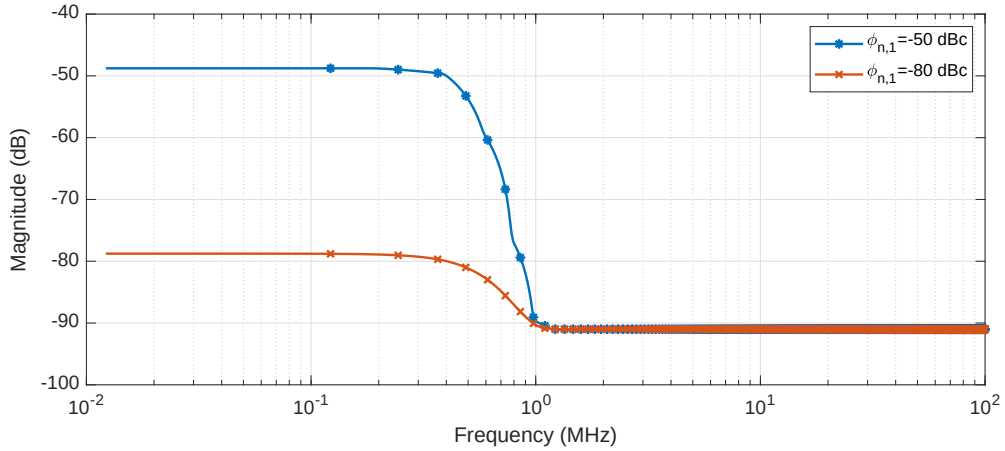

Figure 4.19: Phase noise block frequency response for the minimum and maximum phase noise level 1. It is important to note that the x-axis is plotted in logarithmic scale in order to be able to depict the magnitude response transition. Otherwise, in the linear scale, the magnitude drops very rapidly like a Dirac function.

performance for different SNRs and different phase noise levels (figure 4.24).

Firstly, in Figure 4.24a, the gap between the estimation error of f_1 and f_0 is obvious. Secondly, if the desired P_{err} is 10^{-2}[6], then the SNR should be greater than or equal to **16 dB** such that the condition is satisfied for both f_0, f_1. This means that if the antenna gains are 10 dB at both Tx and Rx, and the receiver NF is 16 dB[7], the maximum detectable distance will be **1.667 m** by using equation (3.9). Thirdly, there is an error floor for high enough SNR. The floor is due to the phase noise. Therefore, in order to have the error rate less than 10^{-2}, the phase noise level should be less than or equal to **-80 dBc**. Note that the curves in Figure 4.24a are not stretched beyond of 10^{-2} due to having small number of estimation samples[8]. Thus, the error floor for f_0 is not shown since it is less than 10^{-2}.

The estimation accuracies versus the phase noise levels are plotted in the figure 4.24b. The phase noise level has a greater influence on the performance of f_0 than f_1 (compare the no-noise cases). For all SNRs, the error rate at the phase noise of -50 dBc is almost 1. In addition, the figure confirms that for having an error rate of less than 10^{-2}, the phase noise level at 500 KHz offset should be less than -80 dBc.

[6]meaning that out of 100 trials, one of the estimations are wrong
[7]this is the NF of the AWR1642/AWR1443.
[8]Each pair of graph in Figure 4.24 for f_0, f_1 requires 8 hours of simulation run.

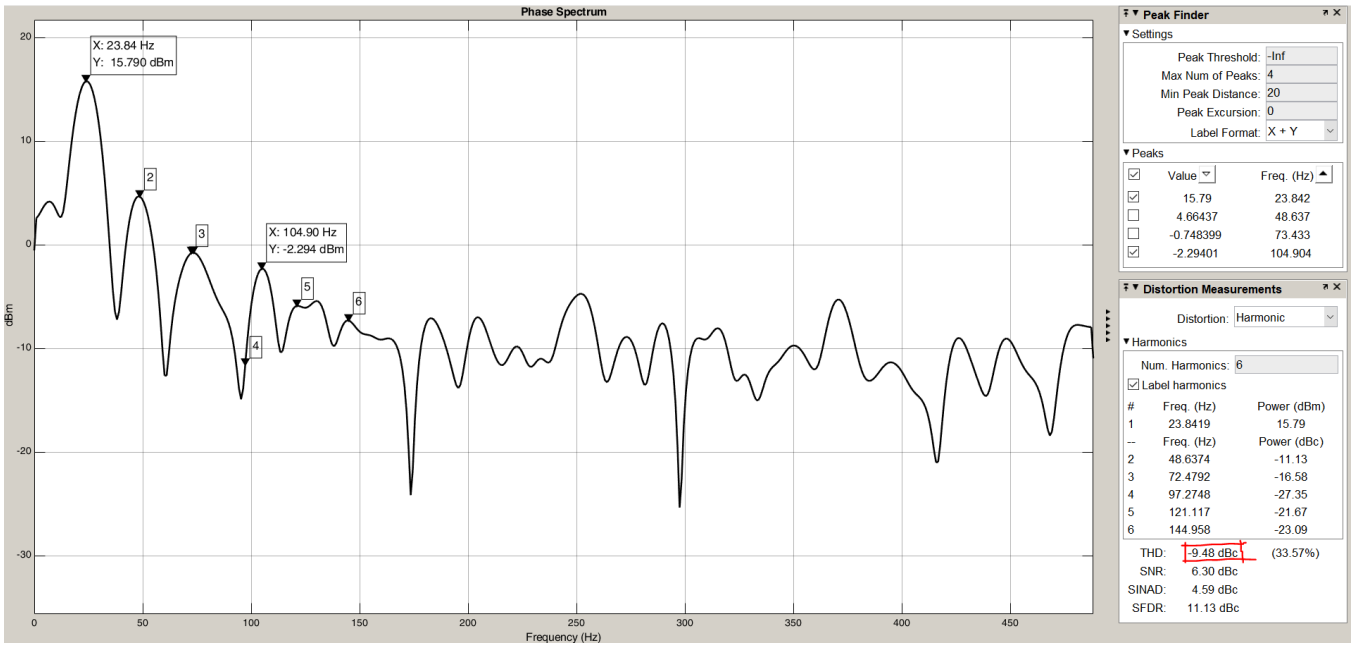

Figure 4.20: Phase spectrum for SNR = 10 dB and the phase noise level 1 = -80 dBc

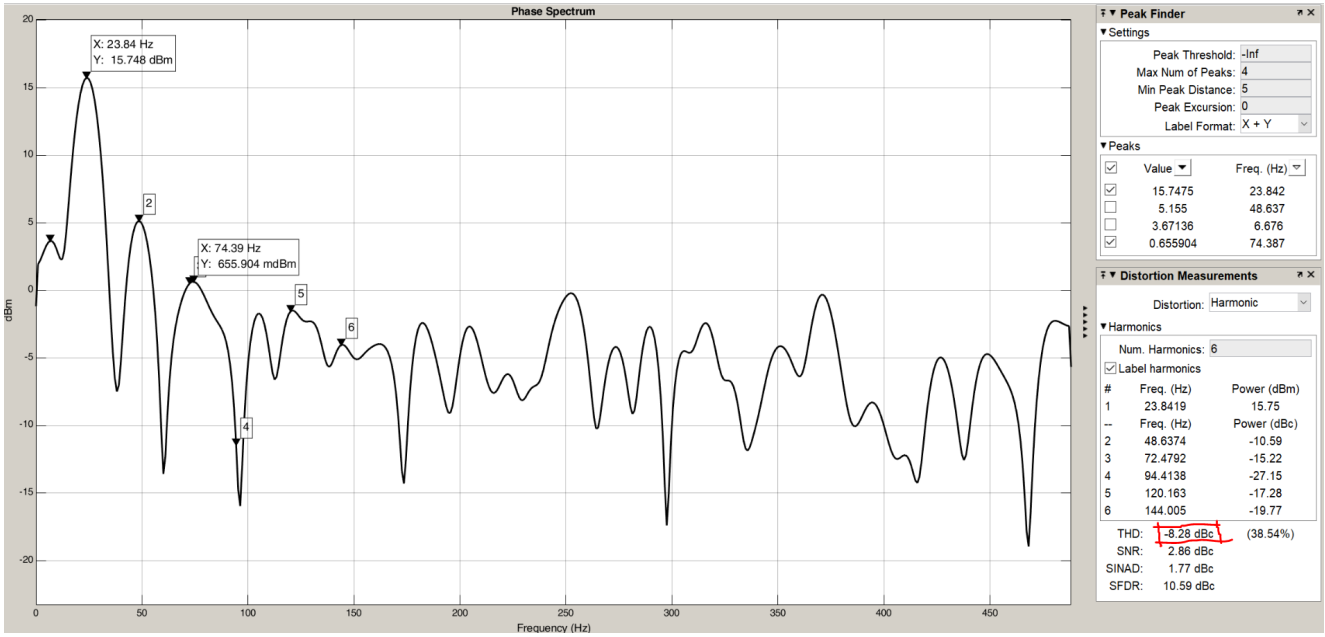

Figure 4.21: Phase spectrum for SNR = 5 dB and the phase noise level 1 = -80 dBc

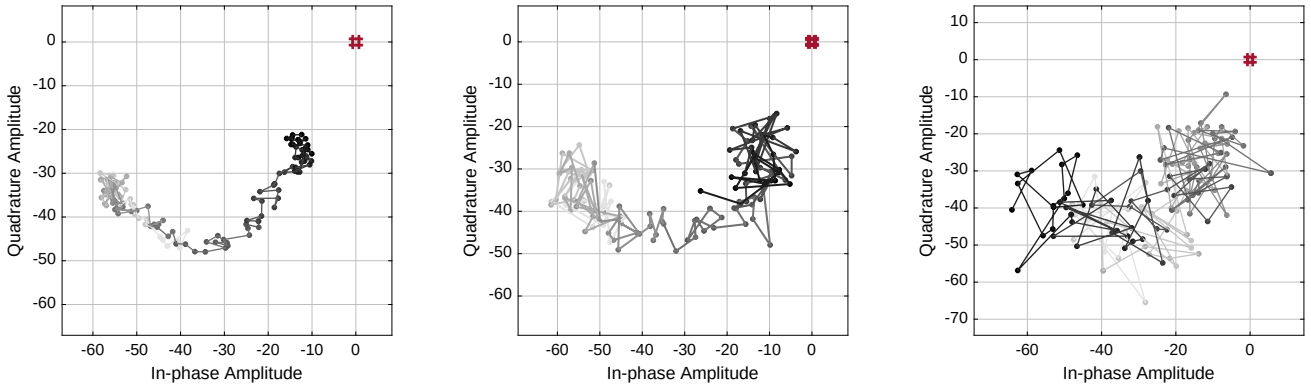

(a) SNR = 18 dB (b) SNR = 10 dB (c) SNR = 5 dB

Figure 4.22: The constellation of the complex signal at different SNRs and the phase noise level 1 of -80 dBc: the color shading is getting stronger for the most recent samples and the origin of the plane is denoted by the square.

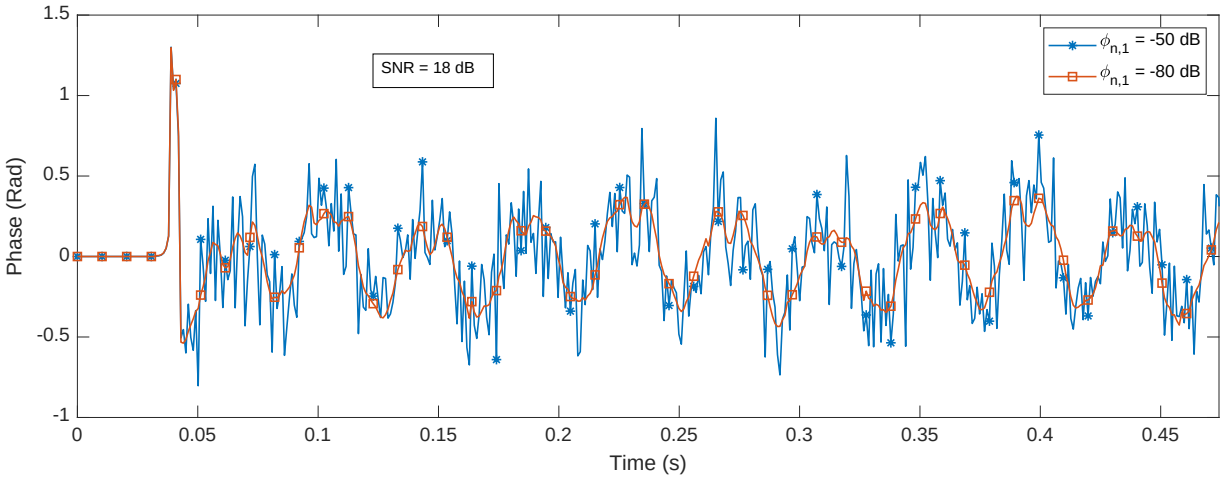

Figure 4.23: Phase time trace for two different phase noise levels

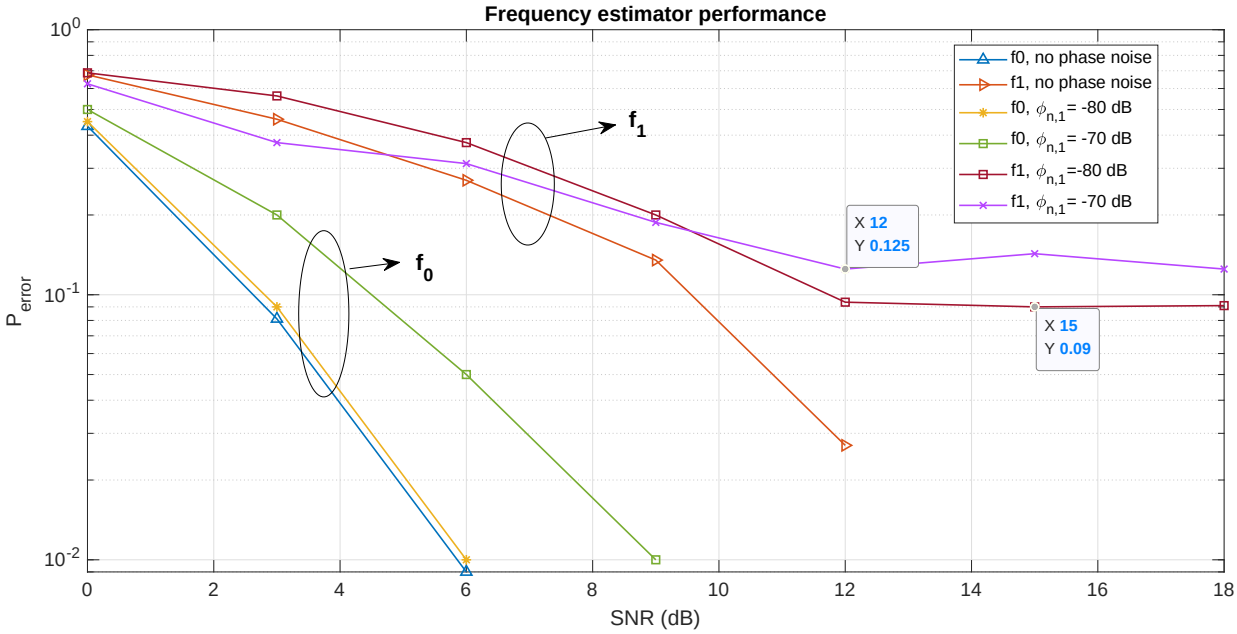

(a)

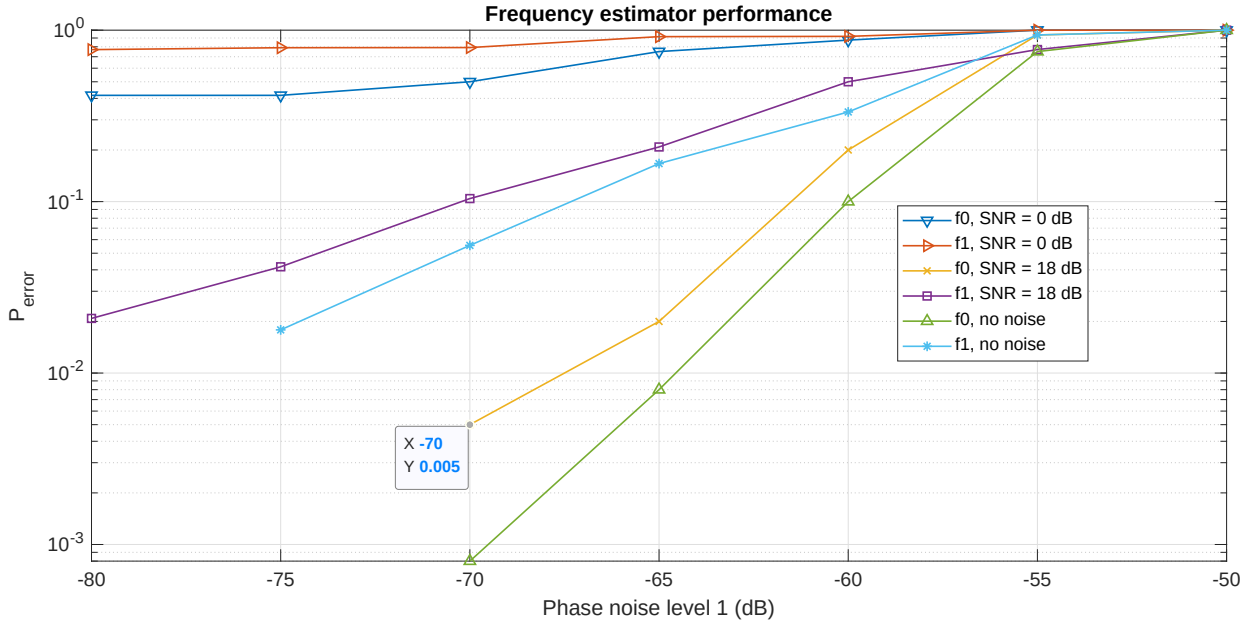

(b)

Figure 4.24: Fundamental frequency estimation error rates vs SNR and phase noise levels: $\phi_{n,1}$ is the phase noise level of 1.

Chapter 5

Application on vital signs detection

Although in general one can use the theories developed in Chapter 2 to detect and find one or two vibrating objects and their features, specifically it can be used for vital signs detection. In this chapter, we will investigate the mm-wave FMCW radar application for vital signs detection. For this purpose, we will use the findings in Chapter 4.

5.1 Signal processing flow

In Figure 5.1, the block diagram of the proposed signal processing chain for vital signs detection is shown. After sampling the beat signal with $f_{b,max}$, the range FFT is applied over the samples of each chirp and the result is a vector, which is called *complex range profile*. By collecting consecutive complex range profiles from multiple chirps and putting them into a matrix in a row-wise manner, the *range-slow time matrix* is constructed with M rows (i.e. M chirps).

Prior to taking the angle of the received complex signal, we must make sure that any non-linearities, distortions, and artifacts have been removed since the phase computation is highly non-linear and it increases the complexity of removing those imperfections. For instance, the DC value of both in-phase and quadrature components of the complex signal must be removed otherwise, it will affect the phase quality. There is no high DC component in the received complex beat signal since none of the DC generators are present at a "good" range except the one that is generated by the cardio-respiratory phase modulation itself. A "good" range is the first range at which we have an intersection to the body. For example, if the subject side is faced to the radar, then his/her shoulder has an intersection to a sphere

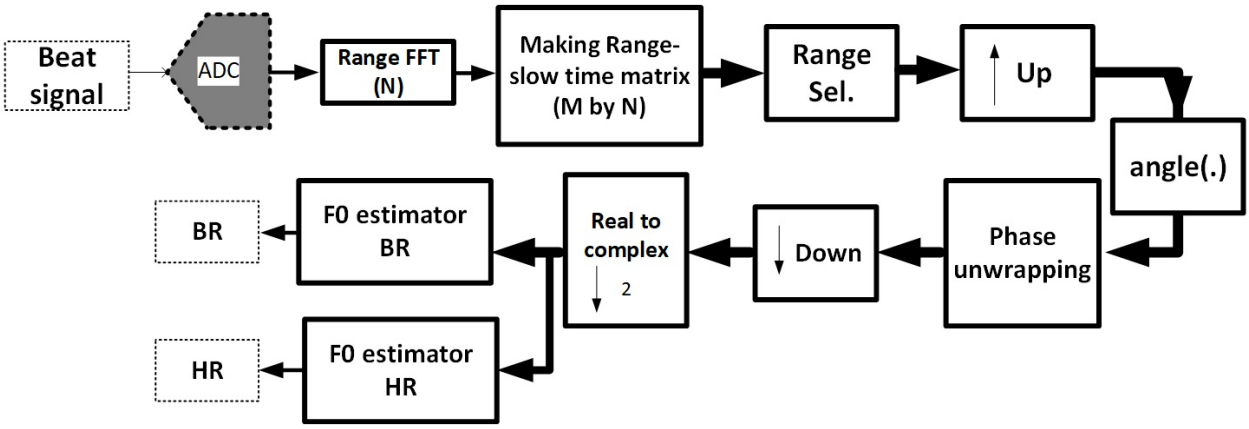

Figure 5.1: Proposed signal processing chain

surface, which has the smallest radius (radius here means the range). In this way, we minimize the effect of the stationary parts of the body, which are recognized as stationary clutters with high RCS. In other words, we do not need to use DC compensation in the following scenarios for the vital signs tests.

After selecting the desired range bin as described before, we upsample the complex signal in order to add redundant samples to have a higher chance of correct phase unwrapping. The upsampling factor for each test will be given. The upsampled complex signal is ready to go to the phase domain.

The phase of each column in the *range-slow time matrix* is calculated by using $\tan^{-1}(.)$ so that the output phases are wrapped in $[-\pi, \pi]$. In contrast, the phase can change beyond of $\pm\pi$ because $x(t)$, the physical displacement, can be greater than $\lambda_{max}/4$. Therefore, there should be a mechanism to unwrap the phase beyond of $\pm\pi$ as it was mentioned in section 3.4. Phase unwrapping is performed on the columns of the *range-slow time matrix* separately (Figure 5.1). For a detailed analysis on the phase unwrapping process see algorithm 1.

The unwrapped phase is downsampled to 40 Hz. Then the signal goes through real to complex transformation in which its sampling rate is reduced by a factor of two making the final sampling rate of 20 Hz. The final sampling rate is enough for the vital signs detection since it contains up to the fourth order harmonics of the HR (it is assumed that the maximum HR is 2 Hz at rest condition). The DC value of each column is removed during real to complex transformation. Then, to find vibration frequencies, the fundamental frequency estimator is employed separately for each vital sign (see algorithm 2).

Radar configuration is the same as in Table 4.1 except that the frame rate may vary from one experiment to another. Thus, for the valid values of the range, Table 4.2 is a true reference. The valid range of vibration frequencies depend on the frame rate and it can be computed using Table 3.1.

In the following sections we will discuss the results and the comparison of this work to similar works using FMCW radar.

5.2 Experiments' setup

In Figures 5.2 and 5.3 the positions of the subject and the radar for sitting and sleeping tests are shown. In the sleep experiments, the radar platform was mounted on the ceiling above the bed as shown in Figure 5.3. We will demonstrate the results for both set ups. The radar was connected to a PC via a USB cable to control the reception and transmission. The raw data is taken and analyzed in Matlab with the processing chain shown in Figure 5.1.

In all tests, a male subject sat or slept approximately 1.5 to 2 m in front of the radar on a chair or on a bed. The 28-years-old subject has the height of 1.7 m and the weight of 62 kilograms. In the sleeping tests, the subject was free to sleep in different positions such as back, stomach, right, and left sides. The Hexoskin vest is worn by the subject to track his BR, HR, and their corresponding waveforms.

Figure 5.2: Sitting tests setup

Figure 5.3: Sleep tests setup

5.3 Waveforms

The vital signs waveform conveys information about the subjects health condition. In fact, the respiration and ECG signals help to diagnose potential diseases in the subject. For instance, there are enormous studies on the heart waveform, ECG, to understand the emotional state of an individual. This analysis is not possible except by having the required cardio-respiration waveforms. Here, we demonstrate the potential use of FMCW radars for deep clinical health diagnostics. The frame rate of the radar was set on 80 fps and we did not use upsampling. For example, Figure 5.4 shows the waveform in which the subject was sitting on a chair faced to the radar[1]. Initially, he was told to hold his breath to capture the phase modulation only due to the heartbeats. After some time, he released his breath to have the combination of the breathing and heart waveforms. The wrapped phase is also drawn to show the effective phase unwrapping. The magnitude of the phase waveform for the breathing is almost 10 times less than the breathing, which is equivalent to 20 dB less power. For a typical adult, the chest moves about 1-12 mm and 0.01-0.5 mm due to breathing and heartbeat, respectively [29]. In fact, in practice, the heart rate extraction is a great challenge due to having imperfect DC cancellation and the strong respiration. Each peak in the heartbeat-only period corresponds to the R peak in the ECG waveform, which is a sharp peak. The detection of the peak further helps to identify the HRV parameter. From the respiration waveform[2], one can retrieve the minute ventilation as well as the tidal volume. Although, they can be computed by the waveform, our focus in this work is on the vital signs rates. Also consider that, there is a linear very low slope in the phase generated by the time delay variations of the RF components, which were warming up at the beginning of the radar operation. In fact, this behaviour will be diminished after 5 minutes or so when the RF part goes in the stable temperature period.

In the sleep study, the radar frame rate was set to 200 fps and the upsampling factor was 2. The higher frame rate is used to be able to track possible body motions. In Figures 5.5 and 5.6, the vital signs waveforms are plotted against that of the Hexoskin vest for different sleep positions. The waveforms all have almost peak-to-peak value of 3 mm except the back-side waveform. This means that the body motion due to the expiration, inspiration and the heartbeats is less from the back side. In these figures, the breathing waveform reconstructed from the optimum filter design is plotted (see section 3.5). The reconstructed noise-free waveform is the summation of the harmonics after estimation of $\boldsymbol{a}$ coefficients in equation (3.36). The optimum filter design parameters for the breathing waveform were set to (N,M,L)=(25 seconds, 10 seconds, 1). Actually, only the first order approximation of the

[1]The sitting-on-the-chair tests were done in which the target is faced directly to the radar front side.
[2]After releasing the breath, the dominant waveform is the breathing.

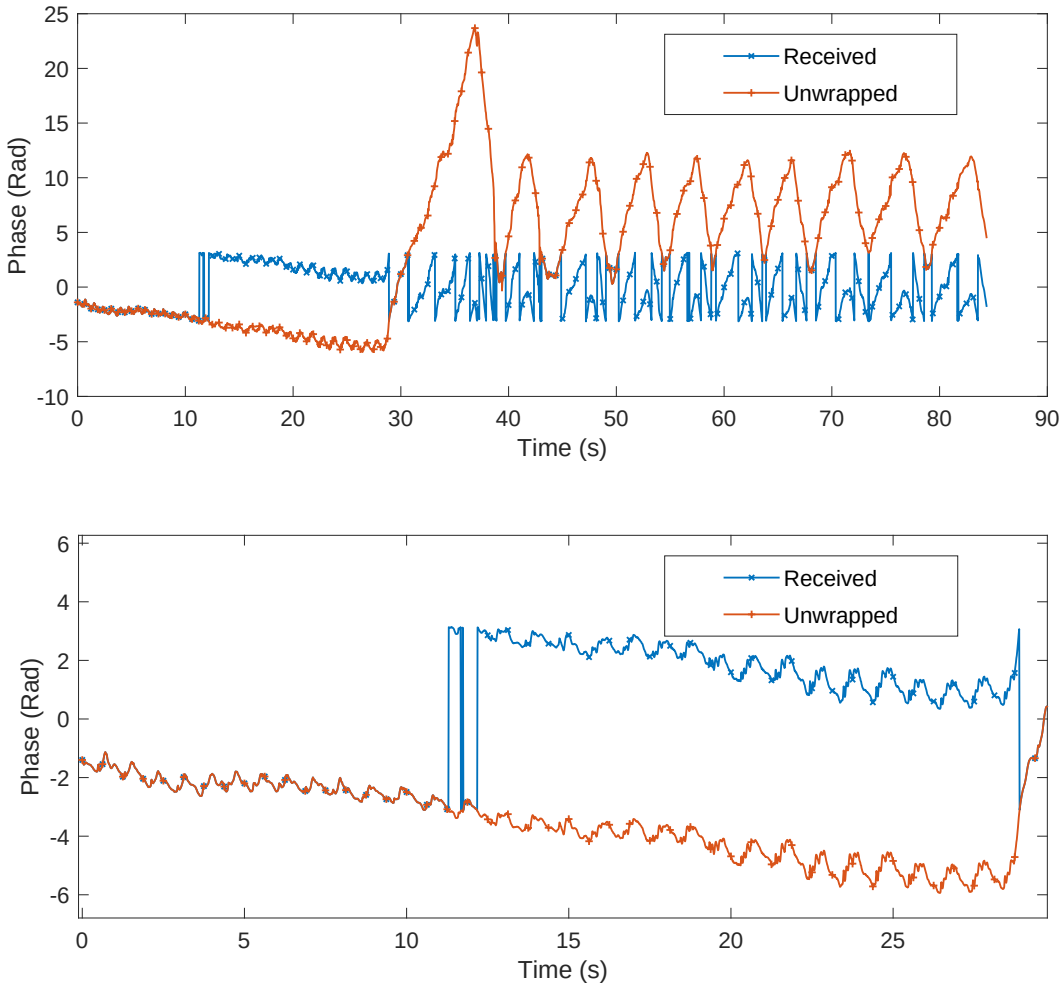

Figure 5.4: Vital signs waveform for hold-and-release-breath tests

breathing waveform is used since the waveform shape is very close to the pure monotone signal. In contrast, for the heart waveform, the filter parameters were set to (N,M,L)=(25 seconds, 10 seconds, 8) because, ECG signal has high order harmonics, hence, we need a high order system model. The results for the heartbeat waveforms obtained by the radar and Hexoskin are shown in figures 5.7 and 5.8. Depending on the quality of the received signal, at particular moments, the heart signal has closer shape to ECG.

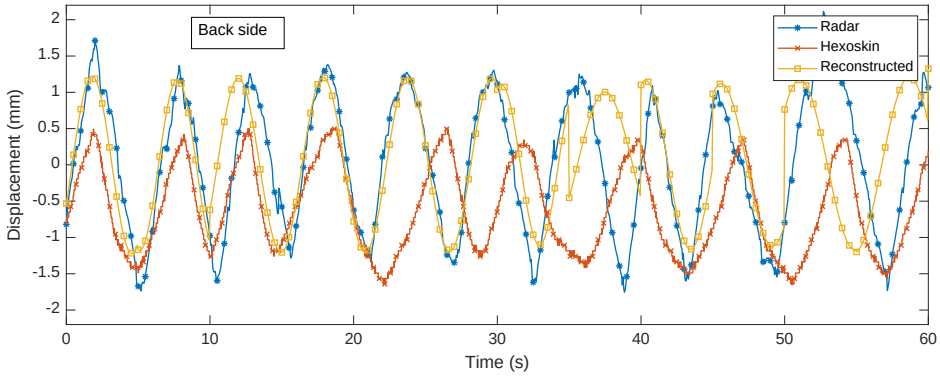

(a) Back

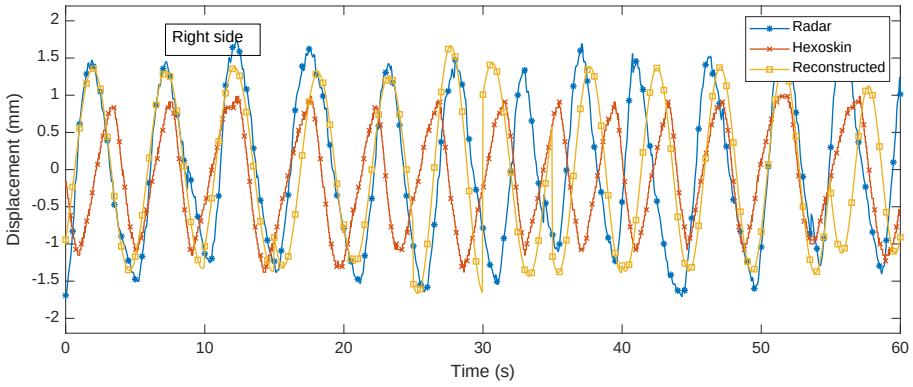

(b) Right

Figure 5.5: Vital signs waveforms for the sleep tests on the back and right side: in each figure, the original phase waveform together with the Hexoskin breathing waveforms and the breathing waveform reconstructed from the optimum filter are plotted.

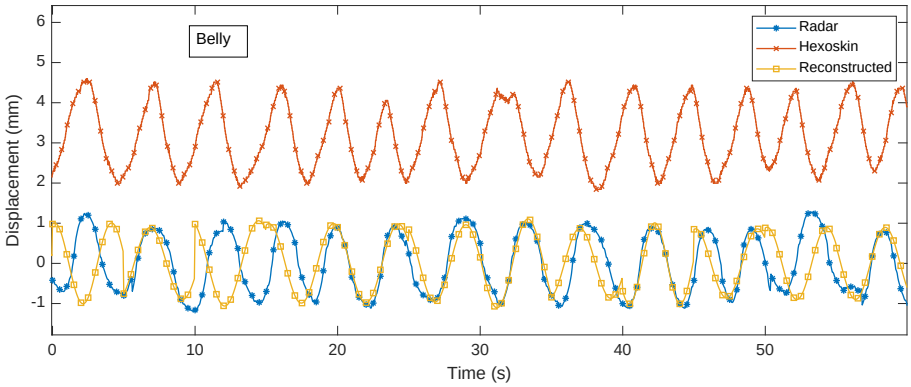

(a)

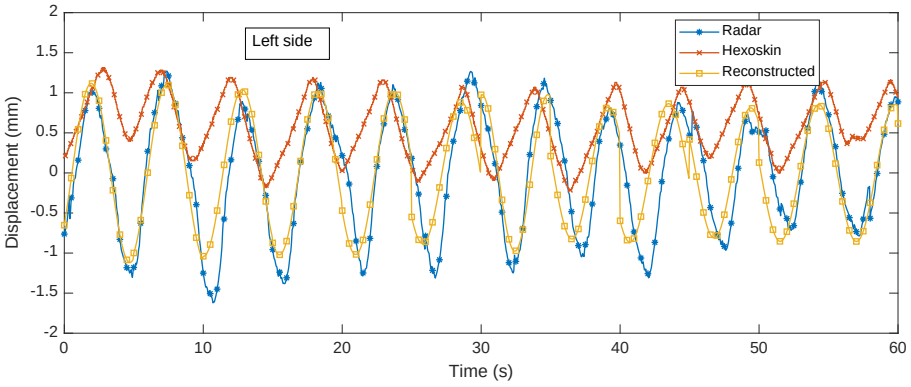

(b)

Figure 5.6: Vital signs waveforms for the sleep tests on the belly and left side: in each figure, the original phase waveform together with the Hexoskin breathing waveforms and the breathing waveform reconstructed from the optimum filter are plotted.

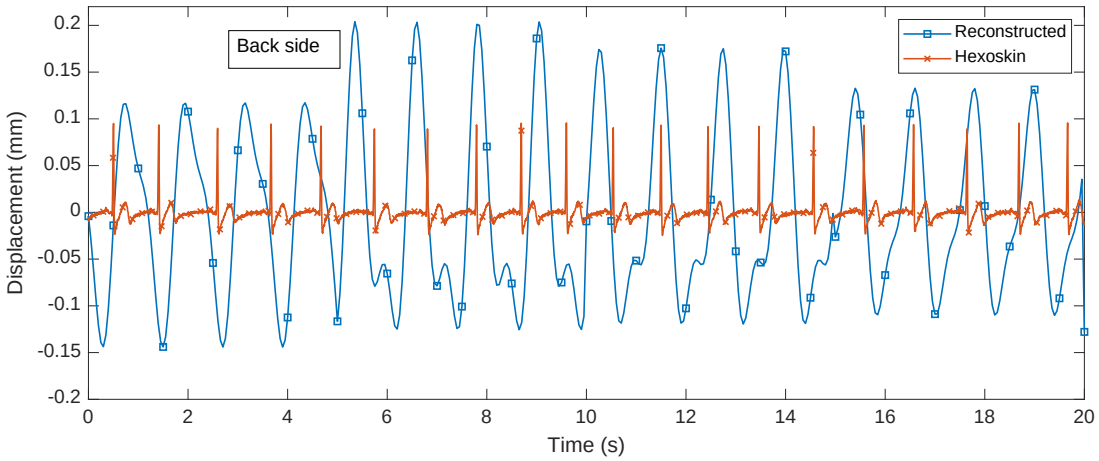

(a) Back

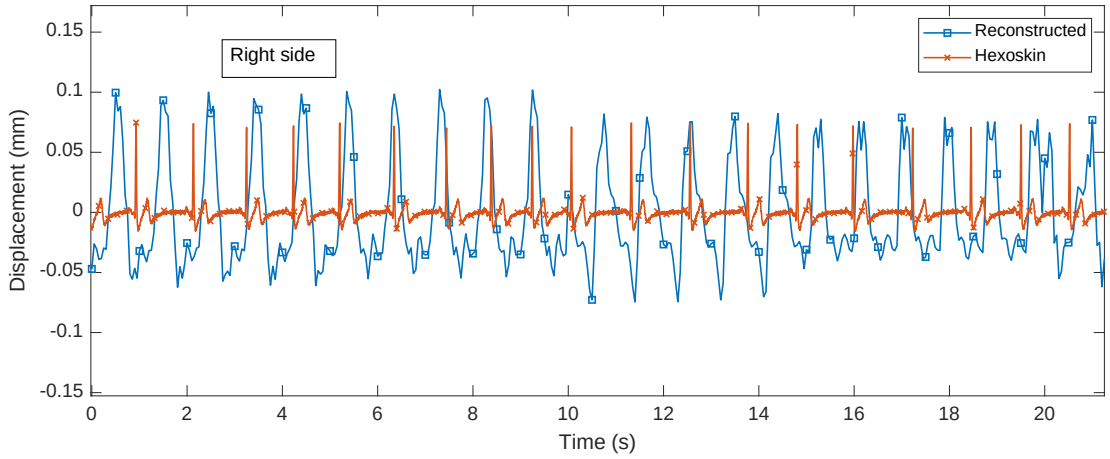

(b) Right

Figure 5.7: Heart waveforms for the sleep tests on the back and right side: in each figure, the ECG signal from Hexoskin vest and the heart waveform reconstructed from the optimum filter are plotted.

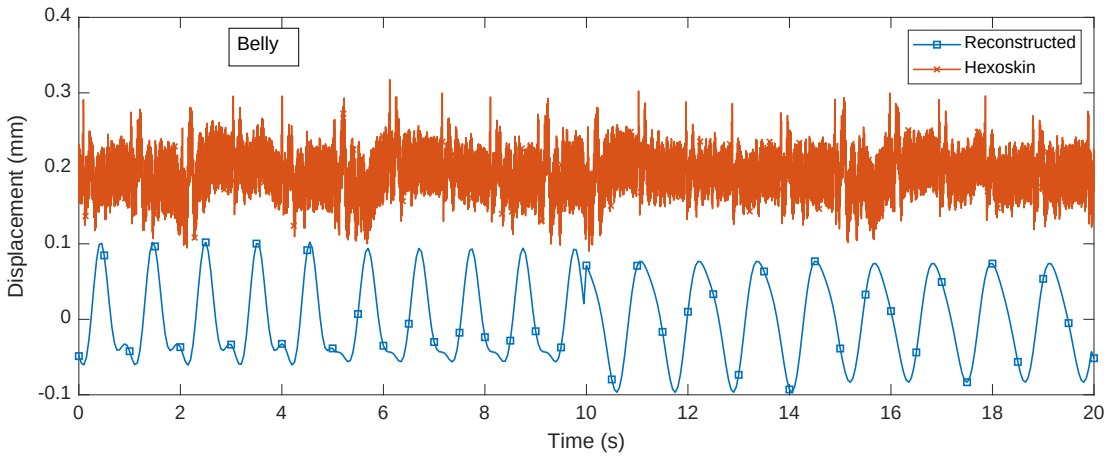

(a) Belly

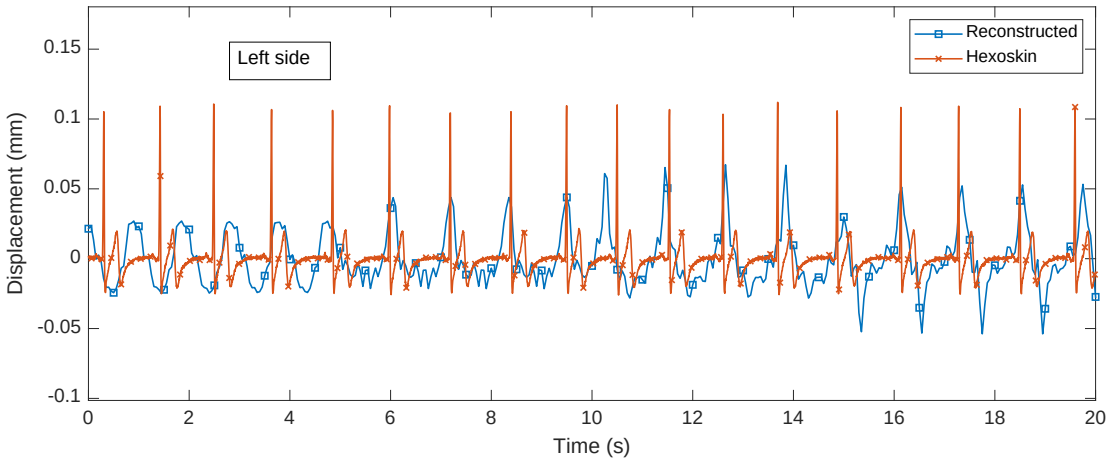

(b) Left

Figure 5.8: Heart waveforms for the sleep tests on the belly and left side: in each figure, the ECG signal from Hexoskin vest and the heart waveform reconstructed from the optimum filter are plotted. Note that the ECG signal when the subject was sleeping on his belly is very noisy, which is due to improper electrodes contact of the Hexoskin vest to the skin surface. The R peaks are obvious to compare with the radar.

5.4 Respiration and heart rates

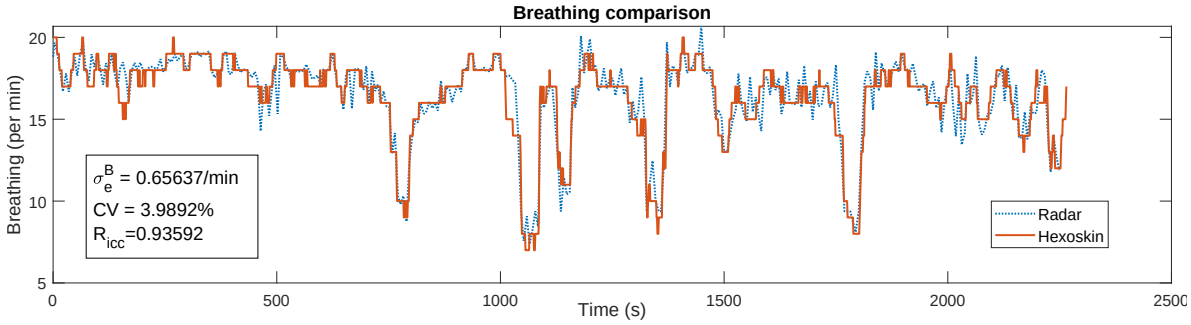

(a) BR time trace

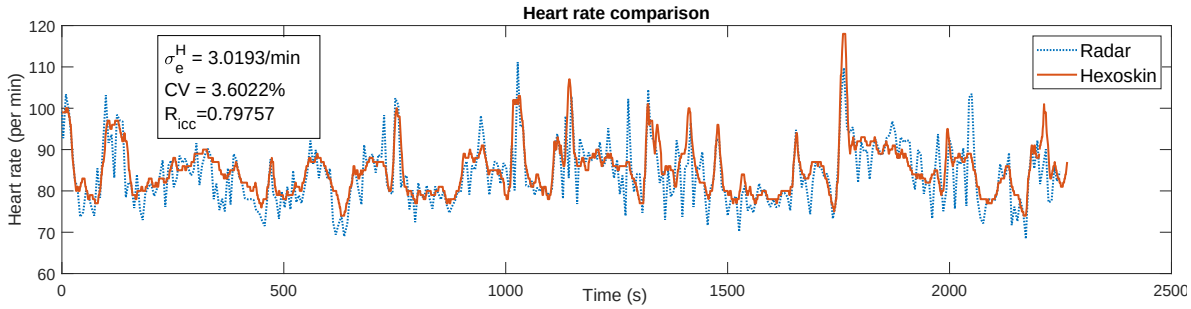

(b) HR time trace

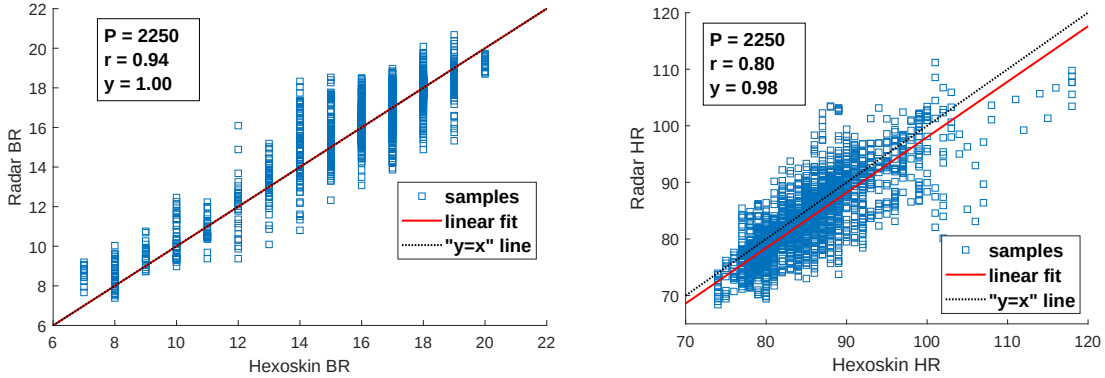

(c) Radar BR vs Hexoskin BR (left), radar HR vs Hexoskin HR (right)

Figure 5.9: Radar BR comparison with Hexoskin (a), and radar HR comparison with Hexoskin (b)

In a 40-minute trial the BR and HR are estimated based on algorithm 2. During the entire test, the subject was sleeping on his back meaning that his face was toward the radar. After removing out-of-norm estimates, which can be due to spark noises and any other external causes, the time trace along with the statistics of BR and HR are shown in Figure 5.9a and Figure 5.9b. In these figures, the instantaneous values of the radar and Hexoskin estimates are compared.

To have intuitions, some statistical parameters are defined to evaluate the similarity, robustness and confidentiality of the radar estimations with respect to Hexoskin estimates. If $\mathbf{e}$ is an error vector with the elements of e_i, then the standard deviation of the error can be stated as:

$$\sigma_e = \sqrt{\frac{1}{P}\sum_{i=1}^{P}(e_i - \bar{e})^2} = \| \boldsymbol{e} \|, \tag{5.1}$$

which is the standard deviation where $\bar{(.)}$ and $\| \, . \, \|$ are the notations for statistical mean and second norm of a vector respectively and P is the number of data points. The correlation of variation (CV) is another factor represents the ratio between the standard deviation and the mean value of the data, d:

$$CV = \frac{\sigma_e}{\bar{d}} \times 100 \tag{5.2}$$

One useful parameter is Pearson correlation coefficient denoted as R_{icc}:

$$R_{icc} = \frac{\sum_{i=1}^{P}\left(d_{r_i} - \bar{d}_{r_i}\right)\left(d_{h_i} - \bar{d}_{h_i}\right)}{\sqrt{\sum_{i=1}^{P}\left(d_{r_i} - \bar{d}_{r_i}^2\right)\sum_{i=1}^{P}\left(d_{h_i} - \bar{d}_{h_i}^2\right)}}, \tag{5.3}$$

in which d_{r_i} and d_{h_i} are the i'th radar and Hexoskin estimations respectively. The value of R_{icc} is in the interval of $[-1, 1]$. The value of 1 means the two data sets are fully correlated and 0, in contrast, means they are uncorrelated. In fact, this correlation describes how two data sets are similar. All the metrics are annotated in the time trace Figures of figure 5.9a and Figure 5.9b.

The sample points cloud in radar-Hexoskin planes is plotted in Figure 5.9c (left) and Figure 5.9c (right) in which r is R_{icc}. The ideal case is when all the samples are sitting on $y = x$ line indicating that the radar data are the same as Hexoskin. In practice, the BR data follows a similar linear behavior around $y = x$ line with a slop of 1 and a 0 bias. Similarly, for HR, the linear fitted curve has a slop of 0.98 and a bias of 0. In the acceptable ranges of HR values, the linear fitted curve is very close to $y = x$ line while they can diverge for very lower or very higher invalid values. It is also good to mention

Table 5.1: HR and BR error rates for different sleep positions: the underlined values are the worst performances

Side	HR (%)	BR (%)
Left	5	**4.26**
Right	**5.86**	4.14
Back	3.95	3.39
Belly	2.5	1.54

Table 5.2: Estimation accuracy comparison to similar works

Ref.	Distance (m)	f_{min} (GHz)	HR (%)	BR (%)	p_{out} (mW)
[15]	2.48	9.6	55.2	—	25
[66]	1	80	87.2	91.08	0.5
Ours	1.7	77	94	95	15.8

that the BR and HR values are well distributed in the whole range of vital signs to show the agreement between the radar observation and the reference sensor.

In table 5.1, the error rates for the vital rates are listed for different sleep positions. Each BR value of the radar, which was in the $\pm$ 1 bpm, was considered as a correct estimation. For HR, the acceptable tolerance was set on $\pm$ 3 bpm. The table shows that with the radar the accuracy of **95%** and **94%** for BR and HR is achieved, respectively.

The performance of our system is compared to similar works in Table 5.2. The values for the front side tests in [66] are in the table to make a fair comparison to our experiments. The performance reported in [66] has a high variance for a particular radar-target orientation. However, we consider the average performance while there might be a case the values are less than 4%. The system performance in [15] is not better than [66] and the best correct estimation rate they obtained is considered here. BR accuracy for [15] was not reported but our system shows an improvement in comparison to [66]. Our HR estimation is much more accurate than [15] and it is so close to [66]. Besides, the output power of our radar is higher than the others (last column of Table 5.2) but the target is somehow in a close range. Although we could not change the distance due to the space limitation in the bedroom, it is possible to use the radar for further distances.

Chapter 6

Summary, outlook, and future extensions

In Chapter 3, the fundamental FMCW radar principles were discussed. In that, the DC compensation method is investigated. But later, in Chapter 4, we have shown that there no DC compensation is required if there is no big stationary target in the range. Also we used the mathematical derivations in Chapter 3 throughout the experiments and simulations in Chapters 4, 5. The experiments showed a good match between theory and the practice. Indeed, the phase unwrapping process is proposed followed by the harmonic analysis based on MUSIC. In fact, MUSIC was used to extract and enhance the periodic signals. The enhancement of the heart signal was shown in the Chapter 5.

Chapter 4 verified the proposed system with the design of different experiments. They are stationary tests, pendulum tests, and the Matlab simulation as well. We discussed the results obtained by the simulations, which are very close to the practical observations.

In Chapter 5, the experiments results were provided for the vital signs detection. Generally, two sets of experiments were conducted. In one setting, a subject was sitting in front of the radar facing to the radar at a right angle. In the second set of experiments, a subject was sleeping on a bed and the radar was mounted on the ceiling above the bed. The final results of BR and HR accuracies are compared to the preceding works. Our measurements showed that HR and BR accuracies in the worst case for all sleeping positions were **94%** and **95%**, respectively.

6.1 Future extensions

One benefit of the FMCW radars is their ability in range discriminations or localization. Thus, it is straightforward to use them for multiple subjects monitoring. Suppose that a single radar is attached on the corner of a bedroom and it monitors the heart and breathing rates of the residents. This is feasible because it has been shown that the radar could detect the vital signs from different positions to the targets.

TI radars can be used to make a network of the sensors. The radars can be cascaded in the master-slave configuration suggesting that multiple radars can be used to continuously monitor the health condition of people in an environment such as in an air plane.

We measured the BR and HR, but it is possible to measure the minute ventilation, HRV etc.

For body motion cancellation, the use of a secondary radar has been suggested by [43, 70]. This idea can be extended to FMCW radars as well. By placing another radar under the bed, it is possible to eliminate the subject movements by giving the second radar signal as a reference to an ANC unit.

In addition, a phased array antenna can be designed to narrow the antennas pattern. This will help to have a focused beam on the body where the chest is moving rather than having a wave impinged on the whole body. The other parts of the body, which are not contributing to the vital phase modulation will be observed as stationary clutters. Thus, exploiting narrowband arrays at both Tx and Rx help to resolve the DC issue in the phase analysis. More advancely, TI has another type of mm-wave chips with the name of AWR1242 [1] with which we can connect a couple of them to have a large of number of antennas. In fact, the chipsets are only RF front-ends and we can make a phased array. Using these chips can be a quick solution for developing a large array of antennas for a mm-wave FMCW radar.

In general, based on the analysis carried out in Chapter 3, and simulations and experiments in Chapter 4, we can design the FMCW radar hardware based on the requirements obtained for the vital signs application. For instance, the phase noise should be smaller than -80 dBc at the particular distance of the subject. The detectable range can be increased by reducing the NF of the receiver and increasing the output power.

References

[1] AWR1243 76-to-81ghz high-performance automotive MMIC | TI.com.

[2] AWR1443 Single-Chip 76-to-81ghz Automotive Radar Sensor Integrating MCU and Hardware Accelerator | TI.com.

[3] AWR1443boost AWR1443 Single-Chip 76-to-81ghz Automotive Radar Sensor Evaluation Module | TI.com.

[4] AWR1642 Single-chip 76-to-81ghz automotive radar sensor integrating DSP and MCU | TI.com.

[5] AWR1642boost AWR1642 single-chip 76-to-81ghz automotive radar sensor integrating DSP and MCU evaluation module | TI.com.

[6] The BioRadio Wireless Physiology Monitor |.

[7] Computing the discrete-time "analytic" signal via FFT - IEEE Journals & Magazine.

[8] The dielectric properties of biological tissues: III. Parametric models for the dielectric spectrum of tissues - IOPscience.

[9] An electromagnetic model of human vital signs detection and its experimental validation - IEEE journals & magazine.

[10] Joint High-Resolution Fundamental Frequency and Order Estimation - IEEE Journals & Magazine.

[11] Optimal carrier frequency of non-contact vital sign detectors - IEEE conference publication.

[12] A robust and computationally efficient subspace-based fundamental frequency estimator - IEEE journals & magazine.

[13] Robust doppler radar demodulation via compressed sensing - IET journals & magazine.

[14] Alfred V. Aho and Jeffrey D. Ullman. *Foundations of Computer Science*. W H Freeman & Co, new edition edition edition.

[15] L. Anitori, A. de Jong, and F. Nennie. Fmcw radar for life-sign detection. In *2009 IEEE Radar Conference*, pages 1–6, May 2009.

[16] S. Ayhan, S. Scherr, A. Bhutani, B. Fischbach, M. Pauli, and T. Zwick. Impact of Frequency Ramp Nonlinearity, Phase Noise, and SNR on FMCW Radar Accuracy. *IEEE Transactions on Microwave Theory and Techniques*, 64(10):3290–3301, October 2016.

[17] Constantine A. Balanis. *Modern Antenna Handbook*. John Wiley & Sons, Incorporated. Google-Books-ID: Q9OgkQEACAAJ.

[18] S. Benchikh, H. Arab, and S. O. Tatu. A novel millimeter wave radar sensor for medical signal detection. In *2018 IEEE International Microwave Biomedical Conference (IMBioC)*, pages 142–144.

[19] M. C. Budge and M. P. Burt. Range correlation effects in radars. In *The Record of the 1993 IEEE National Radar Conference*, pages 212–216, 1993.

[20] A. T. Cemgil. *Bayesian Music Transcription*. [S.l. : s.n.].

[21] K. W. Chan and H. C. So. Accurate frequency estimation for real harmonic sinusoids. 11(7):609–612.

[22] N. Chernov and C. Lesort. Least squares fitting of circles. 23(3):239–252.

[23] M. G. Christensen and A. Jakobsson. Optimal filter designs for separating and enhancing periodic signals. 58(12):5969–5983.

[24] M. G. Christensen and A. Jakobsson. Optimal Filter Designs for Separating and Enhancing Periodic Signals. *IEEE Transactions on Signal Processing*, 58(12):5969–5983, December 2010.

[25] M. G. Christensen, A. Jakobsson, and S. H. Jensen. Fundamental Frequency Estimation using the Shift-Invariance Property. In *2007 Conference Record of the Forty-First Asilomar Conference on Signals, Systems and Computers*, pages 631–635, November 2007.

[26] Mads Christensen and Andreas Jakobsson. *Multi-Pitch Estimation*. Morgan and Claypool Publishers.

[27] Mads Christensen and Andreas Jakobsson. *Multi-Pitch Estimation*. Morgan & Claypool Publishers, March 2009. Google-Books-ID: DtJcAQAAQBAJ.

[28] L. Ding, M. Ali, S. Patole, and A. Dabak. Vibration parameter estimation using FMCW radar. In *2016 IEEE International Conference on Acoustics, Speech and Signal Processing (ICASSP)*, pages 2224–2228, March 2016.

[29] Amy Diane Droitcour. *Non-Contact Measurement of Heart and Respiration Rates with a Single-Chip Microwave Doppler Radar*. 2006.

[30] N. Du, K. Liu, L. Ge, and J. Zhang. ApneaRadar: A 24ghz Radar-Based Contactless Sleep Apnea Detection System. In *2017 2nd International Conference on Frontiers of Sensors Technologies (ICFST)*, pages 372–376, April 2017.

[31] C. Gabriel, S. Gabriel, and E. Corthout. The dielectric properties of biological tissues: I. literature survey. 41(11):2231.

[32] C. Gabriel, S. Gabriel, and E. Corthout. The dielectric properties of biological tissues: I. Literature survey. *Physics in Medicine & Biology*, 41(11):2231, 1996.

[33] S. Gabriel, R. W. Lau, and C. Gabriel. The dielectric properties of biological tissues: II. measurements in the frequency range 10 hz to 20 GHz. 41(11):2251.

[34] S. Gabriel, R. W. Lau, and C. Gabriel. The dielectric properties of biological tissues: III. parametric models for the dielectric spectrum of tissues. 41(11):2271.

[35] S. Gabriel, R. W. Lau, and C. Gabriel. The dielectric properties of biological tissues: II. Measurements in the frequency range 10 Hz to 20 GHz. *Physics in Medicine & Biology*, 41(11):2251, 1996.

[36] S. Godsill and M. Davy. Bayesian harmonic models for musical pitch estimation and analysis. In *2002 IEEE International Conference on Acoustics, Speech, and Signal Processing*, volume 2, pages II–1769–II–1772.

[37] Andrea Goldsmith. *Wireless Communications*. Cambridge University Press, Cambridge ; New York, 1 edition edition, August 2005.

[38] S. Guan, J. A. Rice, C. Li, and C. Gu. Automated DC offset calibration strategy for structural health monitoring based on portable CW radar sensor. 63(12):3111–3118.

[39] S. Guan, J. A. Rice, C. Li, and C. Gu. Automated DC offset calibration strategy for structural health monitoring based on portable CW radar sensor. 63(12):3111–3118.

[40] S. M. A. T. Hosseini and H. Amindavar. UWB radar signal processing in measurement of heartbeat features. In *2017 IEEE International Conference on Acoustics, Speech and Signal Processing (ICASSP)*, pages 1004–1007, March 2017.

[41] Carre Technologies inc (Hexoskin). Hexoskin Smart Shirts - Cardiac, Respiratory, Sleep & Activity Metrics.

[42] Carre Technologies inc (Hexoskin). Hexoskin Smart Shirts - Cardiac, Respiratory, Sleep & Activity Metrics.

[43] C. Li and J. Lin. Random body movement cancellation in doppler radar vital sign detection. *IEEE Transactions on Microwave Theory and Techniques*, 56(12):3143–3152, Dec 2008.

[44] C. Li, V. M. Lubecke, O. Boric-Lubecke, and J. Lin. A review on recent advances in doppler radar sensors for noncontact healthcare monitoring. *IEEE Transactions on Microwave Theory and Techniques*, 61(5):2046–2060, May 2013.

[45] C. Li, Y. Xiao, and J. Lin. Experiment and spectral analysis of a low-powerka-band heartbeat detector measuring from four sides of a human body. 54(12):4464–4471.

[46] C. Li, Y. Xiao, and J. Lin. Experiment and spectral analysis of a low-power*ka*-band heartbeat detector measuring from four sides of a human body. *IEEE Transactions on Microwave Theory and Techniques*, 54(12):4464–4471, Dec 2006.

[47] Hongbin Li, Petre Stoica, and Jian Li. Computationally efficient parameter estimation for harmonic sinusoidal signals. 80(9):1937–1944.

[48] A. Mase, Y. Kogi, and T. Maruyama. Real-time evaluation of heart rate and heart rate variability using microwave reflectometry. In *2018 IEEE International Microwave Biomedical Conference (IMBioC)*, pages 160–162.

[49] S. Nahar, T. Phan, F. Quaiyum, L. Ren, A. E. Fathy, and O. Kilic. An electromagnetic model of human vital signs detection and its experimental validation. *IEEE Journal on Emerging and Selected Topics in Circuits and Systems*, 8(2):338–349, June 2018.

[50] A. Nezirovic, A. G. Yarovoy, and L. P. Ligthart. Signal processing for improved detection of trapped victims using UWB radar. 48(4):2005–2014.

[51] A. Michael Noll. Cepstrum pitch determination. 41(2):293–309.

[52] M. Nosrati, S. Shahsavari, and N. Tavassolian. Multi-target vital-signs monitoring using a dual-beam hybrid doppler radar. In *2018 IEEE International Microwave Biomedical Conference (IMBioC)*, pages 58–60.

[53] M. Nosrati and N. Tavassolian. Effects of antenna characteristics on the performance of heart rate monitoring radar systems. *IEEE Transactions on Antennas and Propagation*, 65(6):3296–3301, June 2017.

[54] M. Nosrati and N. Tavassolian. Accuracy enhancement of doppler radar-based heartbeat rate detection using chest-wall acceleration. In *2018 IEEE International Microwave Biomedical Conference (IMBioC)*, pages 139–141, June 2018.

[55] P. Pahl, T. Kayser, M. Pauli, and T. Zwick. Evaluation of a high accuracy range detection algorithm for FMCW/phase radar systems. In *The 7th European Radar Conference*, pages 160–163, September 2010.

[56] B. Park, O. Boric-Lubecke, and V. M. Lubecke. Arctangent demodulation with DC offset compensation in quadrature doppler radar receiver systems. 55(5):1073–1079.

[57] H. Rohling. Radar CFAR Thresholding in Clutter and Multiple Target Situations. *IEEE Transactions on Aerospace and Electronic Systems*, AES-19(4):608–621, July 1983.

[58] F. Schadt, F. Mohr, and M. Holzer. Application of kalman filters as a tool for phase and frequency demodulation of iq signals. In *2008 IEEE Region 8 International Conference on Computational Technologies in Electrical and Electronics Engineering*, pages 421–424, July 2008.

[59] K. Thurn, R. Ebelt, and M. Vossiek. Noise in homodyne FMCW radar systems and its effects on ranging precision. In *2013 IEEE MTT-S International Microwave Symposium Digest (MTT)*, pages 1–3.

[60] A. Vallan, M. L. Casalicchio, and G. Perrone. Displacement and acceleration measurements in vibration tests using a fiber optic sensor. 59(5):1389–1396.

[61] ∅. Aardal, Y. Paichard, S. Brovoll, T. Berger, T. S. Lande, and S. E. Hamran. Physical working principles of medical radar. *IEEE Transactions on Biomedical Engineering*, 60(4):1142–1149, April 2013.

[62] M. Vespe, G. Jones, and C. J. Baker. Lessons for Radar. *IEEE Signal Processing Magazine*, 26(1):65–75, January 2009.

[63] Rodrigo Villar, Thomas Beltrame, and Richard L. Hughson. Validation of the Hexoskin wearable vest during lying, sitting, standing, and walking activities. *Applied Physiology, Nutrition, and Metabolism = Physiologie Appliquee, Nutrition Et Metabolisme*, 40(10):1019–1024, October 2015.

[64] J. Wang, X. Wang, L. Chen, J. Huangfu, C. Li, and L. Ran. Noncontact distance and amplitude-independent vibration measurement based on an extended dacm algorithm. *IEEE Transactions on Instrumentation and Measurement*, 63(1):145–153, Jan 2014.

[65] J. Wang, X. Wang, Z. Zhu, J. Huangfu, C. Li, and L. Ran. 1-d microwave imaging of human cardiac motion: An ab-initio investigation. 61(5):2101–2107.

[66] S. Wang, A. Pohl, T. Jaeschke, M. Czaplik, M. Kny, S. Leonhardt, and N. Pohl. A novel ultra-wideband 80 ghz fmcw radar system for contactless monitoring of vital signs. In *2015 37th Annual International Conference of the IEEE Engineering in Medicine and Biology Society (EMBC)*, pages 4978–4981, Aug 2015.

[67] B. Widrow, J. R. Glover, J. M. McCool, J. Kaunitz, C. S. Williams, R. H. Hearn, J. R. Zeidler, J. Eugene Dong, and R. C. Goodlin. Adaptive noise cancelling: Principles and applications. 63(12):1692–1716.

[68] P. C. Yuen and G. C. Feng. A novel method for parameter estimation of digital arc. 17(9):929–938.

[69] P. C. Yuen and G. C. Feng. A novel method for parameter estimation of digital arc. 17(9):929–938.

[70] F. Zhu, K. Wang, and K. Wu. A fundamental-and-harmonic dual-frequency doppler radar system for vital signs detection enabling radar movement self-cancellation. *IEEE Transactions on Microwave Theory and Techniques*, pages 1–13, 2018.

APPENDICES

Appendix A

TI mm-wave FMCW radars

In order to configure the radar, after connecting the radar to a PC, a series of commands should be sent to the radar for the configuration. The bellow commands are transferred via UART port to the radar as a command line interface (CLI). Each line is a command. Some of them mandatory and some of them are optional. But here, we will have a quick review of the parameters set by these commands and for more details refer to the newest *mm-wave SDK* document [4, 2].

```
sensorStop
flushCfg
dfeDataOutputMode 1
channelCfg 15 3 0
adcCfg 2 1
adcbufCfg -1 0 0 1 0
profileCfg 0 77 7 6 57 0 0 70 1 100 2000 0 0 30
chirpCfg 0 0 0 0 0 0 0 1
frameCfg 0 0 2 0 12.5 1 0
lowPower 0 0
guiMonitor 0 0 0 0 1
vitalSignsCfg 1.5 2.2 256 512 1 0.1 0.05 100000 300000
motionDetection 1 20 2.0 0
sensorStart
```

The description of the commands are given in the following table:

Table A.1: CLI command description

CLI name	**Parameters**	**Descriptions**
sensorStop		Should be the 1st command

flushCfg		Should be 2nd command
dfeDataOutputMode	1	Frame-based chirp. The advanced frame configuration is not used here.
channelCfg	15 3 0	4 Rx and 1 Tx are used because this is a 2D profile.
adcCfg	2 1	16-bit ADC is used. The ADC output is complex. It can also be configured as real. This 1x complex output which means the image band is filtered out. Each 16-bit output contains both real and imaginary parts.
adcbufCfg	-1 0 0 1 0	The memory is configured as complex. The position of IQ in the 16-bit data is determined as I is in LSB and Q is in MSB. The channel output is not interleaved, which is the only option supported by AWR16xx and AWR14xx. The last input is for setting the threshold for triggering ping/pong ADC buffer usage. In fact, the ADC must know when to switch between ping/pong memories. This is depending on the number of samples are received in a chirp period. The number of samples depends on the number of Rx as well. Only option 1 is available for AWR14xx.

profileCfg	0 77 7 6 57 0 0 70 1 100 2000 0 0 30	This configuration can be changed between stop and start commands. It is possible to define different chirp profiles, though it is possible to define different chirps to put them in a frame. In AWR14xx only one profile is allowed to be used in the chirp frame. The start frequency is set on 77GHz. "idle time is set $7\mu s$. (float) "ADC valid start time is set to $6\mu s$. (float) "Ramp end time = $57\mu s$. This plus the idle time is equivalent to chirp duration. The "output power back-off is set on 0. (float) The "tx phase shifter is set to 0. "frequency slope = $70MHz/\mu s$. This together with "ramp end time" mean that the bandwidth is 3.99GHz. (float) "Tx start time = $1\mu s$. (float) "number of ADC samples = 100. So, per chirp 100 samples are collected. Probably, this is managed by the decimating/interpolating filters inside the ADCs. "digital ADC output sampling rate = 2000 Ksps. The "number of ADC samples = "ADC sampling rate * "sampling time. So, "sampling time = $50\mu s$. "High pass filter1 = has cutoff frequency of 175KHz. "High pass filter2 = has cutoff frequency of 350KHz. "Rx gain = 30 dB.

chirpCfg	0 0 0 0 0 0 0 1	This is a mandatory command. “chirp start index = 0 “chirp end index = 0 “Profile identifier = 0 “start freq variation = 0 (Hz) “freq. slope variation = 0(Hz) “idle time variation = 0 (us) “ADC time variation = 0 (us) “Tx antenna enabled mask = 1 which means the first Tx is used. So there is one bit per Tx antenna showing whether it is enabled or not. For example, for activating the 3rd antenna the mask should be 4.
frameCfg	0 0 2 0 12.5 1 0	“start chirp index = 0 (can be 0-511) “chirp end index = 0 Because we have only one chirp profile, the start and the end indexes are the same. “Number of loops = 2 (can be 1-255) “Number of frames = 0 “frame periodicity = 21.5 ms “trigger select = 1 which is the software triggered. This is used to determine how to trigger the FFT units for starting the process. “frame trigger delay = 0 ms
guiMonitor	0 0 0 1	detected objects = the export of detected objects is not enabled. “log mag range is not enabled. “noise profile is no activated. “range-azimuth heat map is enabled.
sensorStart		Runs the sensor.

Appendix B

Matlab codes and the Simulink model

The phase unwrapping process is written in the listing B.1. The Matlab code for the optimum filter is written in the listing B.2.

Listing B.1: Phase Unwrapping Matlab code

```
% The input must contain phases of the ranges where each column is for a
% specific range. In other words, treating each column as an independent
% channel.
%
% UPDATEs:
% September 25, 2018: after adding or subtracting 2pi, all the phases to
% the end of the phase vector will be shifted by that amount. Because
   each
% shift corresponds to the unit circle shift up or down to a new circle.
% Thus, all later phases should be assumed to be in a new circle.
% Otherwise, the previous procedure did not allow to have a phase beyond
   of
% [-3pi,3pi].

function UnwrappedPh = unwraphase(PhaseRange)

    % unwrapping the phase
    for i = 1:length(PhaseRange)-1
        cols = PhaseRange(i+1,:)-PhaseRange(i,:) > pi;
        if (sum(cols)>0)
```

```
            colsIdx = find(cols ~=0);
            for jj = 1:length(colsIdx)
                PhaseRange(i+1:end,colsIdx(jj)) =  PhaseRange(i+1:end,
                    colsIdx(jj))-2*pi;
            end
        end
        cols1 = PhaseRange(i+1,:)-PhaseRange(i,:) < -pi;
        if (sum(cols1)>0)
            colsIdx = find(cols1 ~=0);
            for jj = 1:length(colsIdx)
                PhaseRange(i+1:end,colsIdx(jj)) =  PhaseRange(i+1:end,
                    colsIdx(jj))+2*pi;
            end
        end
        if cols1==cols & sum(cols1) > 0
           display('At the same time PhaseRange(i+1)-PhaseRange(i)<> \pi'
              )
        end

    end

    UnwrappedPh = PhaseRange;
end
```

Listing B.2: Fundamental frequency estimation Matlab code

```
%% Function of both fundamental frequency estimation and periodic signal
   characterization
% [1] M. G. Christensen and A. Jakobsson,  Optimal Filter Designs for
%     Separating and Enhancing Periodic Signals,    IEEE Trans. Signal
%     Process., vol. 58, no. 12, pp. 5969  5983 , Dec. 2010.
%
% *Inputs* :
%           - "y_complex"       : the complex input phase
%           - "R_hat"           : estimated autocorrelation of the input
   phase
%           - "freqSet"         : set of candidate frequencies
%           - "M"               : averaging length
%           - "L"               : # of harmonics
%           - "pw"              : output power vs frequencies in "freqSet
   "
%           - "p_hat"           : the output power of the optimum filter
%           - "a_mat"           : a matrix with the columns of a
   coefficients for each "freqSet" member.
```

```
%           - "h_k_mat"         : a matrix with the columns of h
    coefficients for each "freqSet" member
%
function [pw p_hat a_mat h_k_mat] = f0_a_est(y_cmplx,R_hat,freqSet,M,L)

G = length(y_cmplx)-M+1;
for ii=1:length(freqSet)

    G_k = zeros(L,M);
    W_k = zeros(L);
    for i2=1:G
        w_k_n = exp(1j*2*pi*freqSet(ii)*(1:L)*(M+i2-2)).';
        G_k = G_k + 1/G * w_k_n*(y_cmplx(M+i2-1:-1:i2))';
        W_k = W_k + 1/G * w_k_n*(w_k_n)';
    end
    Q_k = R_hat - G_k' * W_k^-1 * G_k;
    Z_k = MakeA(2*pi*freqSet(ii),M,L);
    h_k_hat = Q_k^-1 * Z_k * (Z_k'*Q_k^-1*Z_k)^-1 * ones(L,1);

    pw(ii) = (h_k_hat)'*R_hat*h_k_hat;
    p_hat(ii) = ones(1,L) * (Z_k'*Q_k^-1*Z_k)^-1 * ones(L,1);
    a_mat(:,ii) = W_k^-1*G_k*h_k_hat;
    h_k_mat(:,ii) = h_k_hat;
end

end

%% functions added to make matrix A
function A = MakeA(omega,M,L)
    a_ = @(omega) exp(-1j*omega*(0:M-1)).';
    A = zeros(M,L);
    for jj=1:L
    A(:,jj) = a_(omega*jj);
    end
end
```

For the Simulink model, we have shown the main page in Figure 4.17. There are subsystems, subsubsystems, etc. In Listings B.1 to B.4, the subsystems of the model are illustrated with their order of placements in the transceiver chain. For instance, Listing B.1 shows the blocks doing the propagation and collection of the transmitted and received waves, respectively. In the propagation block, which is the *Matlab embedded function*, the transmit array antenna model is formed and it takes the (azimuth,elevation) pair, which is the angle between the targets and the radar. Similarly, the collector, takes the angle and computes the received vector by considering the receiver array antenna and its polarization.

The polarization is considered, so the output will be two vectors corresponding to the co/cross-polarizations. We use the co-polarized received signal.

The channel subsystem in Listing B.2, computes the propagation delay and the free-space pathloss for the travelling wave from the radar platform to the targets location. We have three targets as explained in Section 4.4, there are three separate channels.

The subsystem of the targets is depicted in Listing B.3 in which a block is associated to each target. The platform blocks generate vectors of the position and the velocity of the target at each sample time. The input to each platform block determines the velocity of the target at a particular time stamp. We assumed that the first two targets have a velocity proportion to a function of $2\pi A_v f_v cos(2\pi f_v t)$ such that the instantaneous location of a target is proportion to $A_v sin(2\pi f_v t)$. The input velocities realize the vibration of the targets as intended. Also, in Listing B.3, the *MyTarget* block reflects the wave at the targets by the reflection factor related to the RCS of each target.

At the receiver, after downsampling of the beat signal, it goes in the *signal processing* subsystem where the frame rate of the received chirps is determined, and then he slow-fast time matrix is formed. Then, by applying the *range FFT*, the range-slow time matrix (map) is obtained. The map goes into the constant false alarm rate (CFAR) block to detect the range bin containing the reflections of the targets. Then after upsampling, the phase is calculated and converted to a complex signal in order to find the optimum filters. We used two independent optimum filter calculations for the two vibrating targets. There are blocks for demonstrating and saving the necessary signals in the Matlab workspace.

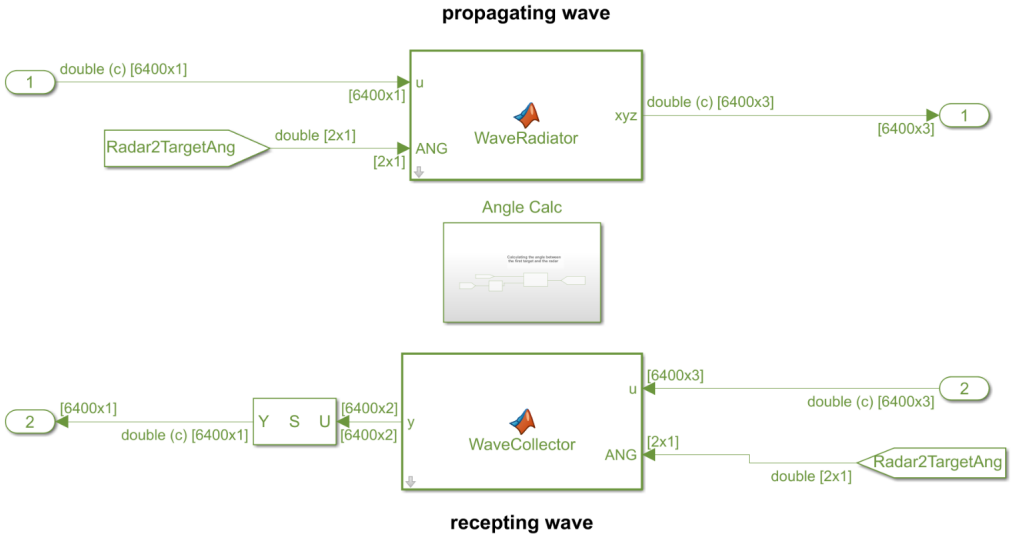

Figure B.1: Propagation and collection subsystem

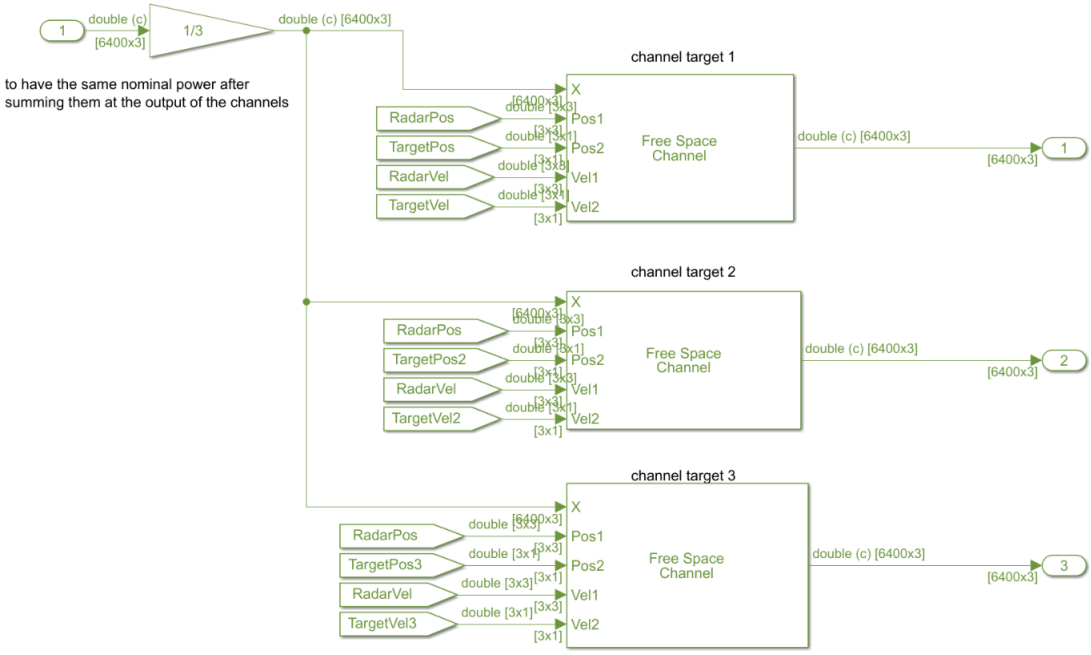

Figure B.2: Channel subsystem

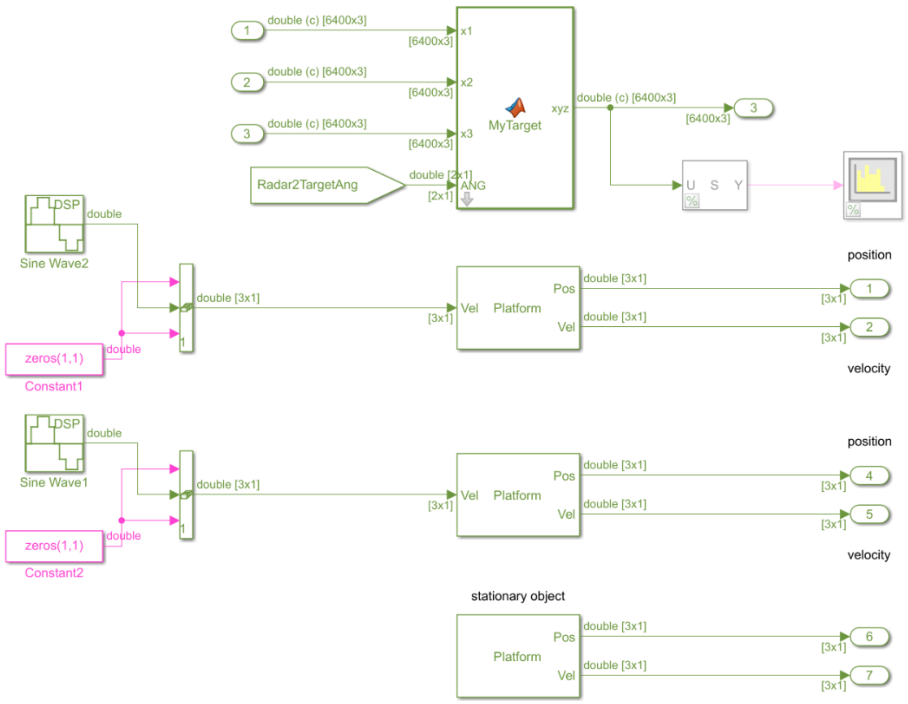

Figure B.3: Targets subsystem

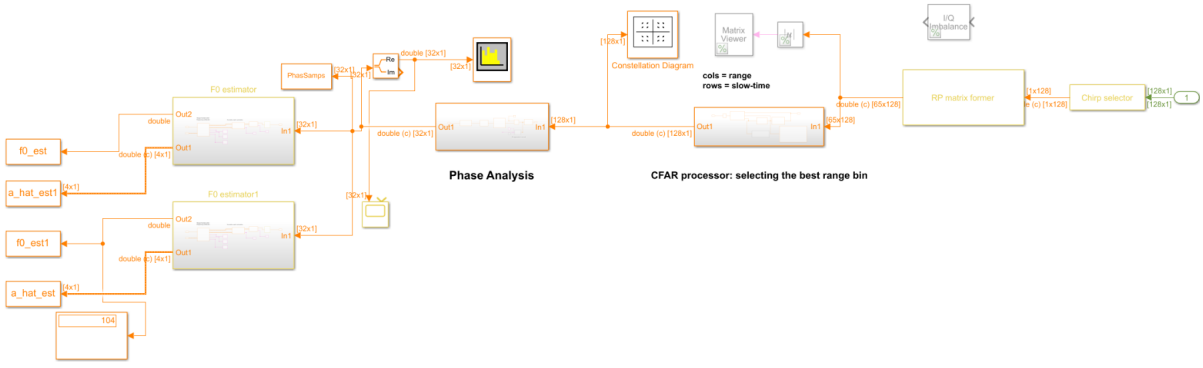

Figure B.4: Signal processing subsystem